AUDRIUS GRAŽEVIČIUS

NUMERICAL INVESTIGATION OF TWO-COMPONENT TWO-PHASE NATURAL CONVECTION AND THERMAL STRATIFICATION PHENOMENA

DOCTORAL DISSERTATION

Kaunas
2020

LITHUANIAN ENERGY INSTITUTE

AUDRIUS GRAŽEVIČIUS

NUMERICAL INVESTIGATION OF TWO-COMPONENT TWO-PHASE NATURAL CONVECTION AND THERMAL STRATIFICATION PHENOMENA

Doctoral dissertation
Technological Sciences, Energetics and Power Engineering (T 006)

2020, Kaunas

This doctoral dissertation was prepared at Lithuanian Energy Institute, Laboratory of Nuclear Installation Safety, during the period of 2015–2019.

Scientific Supervisor:

Assoc. Prof. Dr. Habil. Algirdas KALIATKA (Lithuanian Energy Institute, Technological Sciences, Energetics and Power Engineering, T 006).

Doctoral dissertation has been published in:
http://ktu.edu

Editor:

Agnė Lukševičiūtė ("Bella Verba, UAB" translation agency)

© A. Graževičius, 2020

LIETUVOS ENERGETIKOS INSTITUTAS

AUDRIUS GRAŽEVIČIUS

DVIFAZIO-DVIKOMPONENČIO FLUIDO NATŪRALIOS KONVEKCIJOS IR TERMINĖS STRATIFIKACIJOS PROCESŲ SKAITINIS TYRIMAS

Daktaro disertacija
Technologijos mokslai, energetika ir termoinžinerija (T 006)

2020, Kaunas

Disertacija rengta 2015–2019 metais Lietuvos energetikos institute, Branduolinių įrenginių saugos laboratorijoje.

Mokslinis vadovas:

Doc. habil. dr. Algirdas KALIATKA (Lietuvos energetikos institutas, technologijos mokslai, energetika ir termoinžinerija, T 006).

Interneto svetainės, kurioje skelbiama disertacija, adresas:
http://ktu.edu

Redagavo:

Agnė Lukševičiūtė (UAB „Bella Verba” vertimų biuras)

© A. Graževičius, 2020

CONTENT

NOMENCLATURE 7
INTRODUCTION 10
1. LITERATURE REVIEW 14
1.1. Natural convection phenomenon 14
1.2. Thermal stratification phenomenon 15
1.3. Overview of the most popular CFD software 16
1.3.1. ANSYS Fluent 16
1.3.2. ANSYS CFX 16
1.3.3. OpenFOAM 17
1.3.4. STAR-CD and STAR-CCM+ 17
1.3.5. FLOW-3D 17
1.3.6. PHOENICS 17
1.3.7. COMSOL Multiphysics 18
1.3.8. Code Saturne 18
1.3.9. Performance of different CFD software 18
1.4. Numerical investigations of natural convection and thermal stratification phenomena in the rectangular enclosures by other authors 18
1.5. Summary of literature review and the formulation of scientific problems 23
2. METHODOLOGY OF CFD SIMULATIONS OF NATURAL CONVECTION AND THERMAL STRATIFICATION PHENOMENA 25
2.1. Selection of CFD software and computing resources 25
2.2. The mathematics of ANSYS Fluent software 26
2.3. Geometry and mesh generation 26
2.4. Near-wall modeling 27
2.5. Turbulence modelling 28
2.6. Multiphase modelling 29
2.6.1. The VOF model 30
2.6.2. Evaporation and condensation modelling 31
2.6.3. Governing equations 31
2.7. Convergence 33
2.8. Transient calculation 34
2.9. UDF for heating 35
3. DESCRIPTION OF EXPERIMENTAL FACILITIES AND CFD MODELS 36
3.1. Introduction to KAERI experimental facility 36
3.1.1. Description of the KAERI experimental facility 37
3.1.2. Initial and boundary conditions of the KAERI experiment 38
3.1.3. Lack of information 39
3.2. Introduction to the Osaka University experimental facility 39
3.2.1. Description of the Osaka University experimental facility 39
3.2.2. Osaka University experiment initial and boundary conditions 41
3.2.3. Lack of information 41
3.3. A numerical model for KAERI experiment modelling 41

3.3.1. Mesh generation 42
3.3.2. Boundary and initial conditions of the CFD model for the KAERI experiment 43
3.4. A numerical model for the Osaka University experiment modelling 43
3.4.1. Mesh generation 44
3.4.2. Boundary and initial conditions of the CFD model for Osaka University experiment 47
3.5. Numerical set-up 47
3.6. UDF for heating 48
3.7. Thermal-physical properties of the fluids 49
4. RESULTS AND DISCUSSION 51
4.1. Numerical investigation of the KAERI experiment 51
4.1.1. Influence of the turbulence models 51
4.1.2. Mesh independence study 54
4.1.3. Influence of the heating rate 54
4.1.4. Final calculation 55
4.2. Numerical investigation of the Osaka University experiment 64
4.2.1. Influence of the number of iterations 65
4.2.2. Influence of time step size 67
4.2.3. Influence of the heat transfer coefficient 69
4.2.4. Influence of the heating rate 71
4.2.5. Influence of the heating power 73
4.2.6. Influence of the turbulence models 75
4.2.7. Mesh independence study 77
4.2.8. Final calculation 79
CONCLUSIONS 85
REFERENCES 86
LIST OF SCIENTIFIC ARTICLES RELATED TO DISSERTATION 91
APPENDIXES 93
APPENDIX A: Calculation journal of the KAERI experiment 93
APPENDIX B: Calculation journal of the Osaka University experiment 95

NOMENCLATURE

a	thermal diffusivity of the fluid (m^2/s)
C_1	constant (dimensionless)
$C_{1\varepsilon}$	constant (dimensionless)
C_2	constant (dimensionless)
$C_{3\varepsilon}$	constant (dimensionless)
$coef\ f$	is a coefficient that must be fine-tuned and can be interpreted as a relaxation time (dimensionless)
c_p	specific heat (J/kg·K)
D	cross-diffusion term (m)
E	total energy (or activation energy) (J)
F	force (N)
G	generation ($kg/m{\cdot}s^3$)
Gr	the Grashof number (dimensionless)
g	gravitational acceleration (m/s^2); standard value = 9.80665 m/s^2
h	enthalpy (J/kg)
k	turbulence kinetic energy per unit mass (J/kg)
k_{eff}	effective thermal conductivity (W/m·K)
L	length (m)
M	mass fraction (dimensionless)
$\dot{m}_{lv}$	mass transfer from the liquid to the vapor due to evaporation ($kg/s/m^3$)
$\dot{m}_{pq}$	mass transfer from phase *p* to phase *q* (kg/s)
$\dot{m}_{qp}$	mass transfer from phase *q* to phase *p* (kg/s)
$\dot{m}_{vl}$	mass transfer from the vapor to the liquid due to condensation ($kg/s/m^3$)
n	number of phases
Pr	the Prandtl number (dimensionless)
p	pressure (Pa)
q^{th}	volume fraction (dimensionless)
Ra	the Rayleigh number (dimensionless)
Re	the Reynolds number (dimensionless)
Ri	the Richardson number (dimensionless)
S	user-defined source term (total entropy) (J/K)
S_a	total entropy of volume fraction (J/K)
S_h	source term (total entropy) contains contributions from radiation, as well as any other volumetric heat sources (J/K)
S_{rst}	mean rate-of-strain tensor (s^{-1})
Str	the Stratification number (dimensionless)
T	temperature (K)
t	time (s)
U	mean velocity (m/s)

U_f	volume flux through the face, based on normal velocity (m/s)
u	velocity components (u; v; w) in Cartesian directions: x; y; z (m/s)
V	volume of the cell (m^3)
$\overrightarrow{V_v}$	vapor phase velocity (m/s)
v	velocity (m/s)
x	Cartesian coordinate (m)
Y	dissipation (m^2/s^3)
z	coordinate for the vertical direction (m)

Greek symbols

α	volume fraction (dimensionless)
$\alpha_{q,f}$	face value of the qth volume fraction (dimensionless)
β'	coefficient of thermal expansion of the fluid (1/K)
Γ	effective diffusivity (m^2/s)
Δ	change in variable
ε	turbulent dissipation rate (m^2/s^3)
μ	dynamic viscosity (cP)
ν	kinematic viscosity m^2/s
ρ	density (kg/m^3)
σ	the turbulent Prandtl number (dimensionless)
ω	specific dissipation rate (s^{-1})
∇	the operator referred to as grad, nabla, or del, represents the partial derivative of a quantity with respect to all directions in the chosen coordinate system

Superscripts

n	index for previous time step
$n+1$	index for new (current) time step

Subscripts

b	buoyancy
i	unit vector in the direction of the x-axis
j	unit vector in the direction of the y-axis
k	turbulence kinetic energy
l	liquid
M	Mach number
q	q phase
ref	reference
s	species s
sat	saturation
t	time
w	water

ε	turbulent dissipation rate
ν	vapor phase
ω	specific dissipation rate

Abbreviations

2D	Two-dimensional
3D	Three-dimensional
CA	Chromel-Alumel
CFD	Computational Fluid Dynamics
CFL	Courant-Friedrichs-Lewy
CPU	The Central Processing Unit
GRS	Global Research for Safety
HPC	High Performance Computing
KAERI	Korea Atomic Energy Research Institute
LEI	Lithuanian Energy Institute
NRG	Nuclear Research and consultancy Group
PAFS	Passive Auxiliary Feedwater System
PCCT	Passive Condensate Cooling Tank
PCHX	Passive Condensate Heat eXchanger
PISO	Pressure-Implicit with Splitting of Operators
PIV	Particle Image Velocimetry
RANS	Reynolds-Averaged Navier-Stokes
UDF	User-Defined Function
VOF	Volume Of Fluids

INTRODUCTION

The importance of passive cooling systems for nuclear reactors heat removal function was highlighted after the Fukushima accident on 11 March 2011. Therefore, advanced nuclear power plants are designed with passive cooling systems, which due to the simple operation principle, without the need for external power supply, contribute to nuclear safety. It is necessary to evaluate the ability of passive cooling systems to effectively cool down the nuclear reactor or atmosphere in the containment in order to implement passive cooling systems in a new generation nuclear power plant under construction or design process, and it is directly related to accident management. In the historical context, accident management or mitigation of its consequences using passive cooling systems is particularly important for the operation of nuclear installations as in the worst-case scenario radioactive releases can occur and potentially damage workers, residents, and/or the environment. However, the use of such passive cooling systems in non-nuclear facilities and installations is also important. Firstly, non-nuclear facilities and installations are more widely operated. Secondly, in the industrial sector, there is a growing number of parks of different companies, which use a single powerful thermal energy generation unit as a heat source for a variety of technological processes (e.g. glass or fertilizer manufacturing). It is understandable, that natural convention and thermal stratification phenomena have the same nature and causal laws/relationships in the secondary site of the above mentioned industrial facilities (non-nuclear and nuclear facilities). Therefore, the interpretation of these phenomena, based on operational experience of nuclear installations or results of related experimental investigations, is correct and applicable to similar or analogous thermal energy facilities.

A large volume cooling pool is one component of a passive cooling system, which is designed to accumulate large amounts of heat incoming from the reactor core or the containment in a case of station blackout. Typically, the heat exchangers are located at the bottom of the cooling pool and are designed to transfer heat from the heat source to the cooling pool water. Air circulates freely above the cooling pool. Due to the heat transfer through the walls of the heat exchangers, the density of the water adjacent to the heat exchangers reduces, therefore, lower density water begins to rise upward via the buoyancy force. The heated water after reaching the free surface, cools and mixes with the colder water below and flows around the heat exchangers again. Natural convection flow is formed above the heat exchangers, meanwhile, there is no flow below the heat exchangers and after a while, thermal stratification is formed. As the amount of heat incoming from the heat source increases, water temperature approaches to saturation temperature and water starts to mix under the heat exchangers – thermal stratification disappears. These phenomena occur not only in the above-mentioned cooling pool but also in the spent nuclear fuel pool or the nuclear reactor. Natural convection and thermal stratification phenomena are closely interrelated and particularly important to nuclear safety, and they always have been of interest and remain relevant to engineers, inspectors, and researchers. Currently, there is a growing interest in modelling of these phenomena using CFD software. Although CFD programmes are rapidly developed, these phenomena are

modelled using a lot of simplifications such as fluid properties are constant, analysing single-phase flow, simulations performed using steady-state conditions, the effects of solid walls are neglected, etc. Investigations with these simplifications lose the ability to perform a comprehensive nuclear safety assessment. Therefore, in the development of today's and creation of future nuclear energy, it is necessary to develop the methodology that would allow performing complex modelling of natural convection and thermal stratification phenomena in cooling pools. The developed methodology would allow evaluating the variable thermodynamic-physical properties of the fluid involved in the heat transfer process, changing two-component two-phase flow regime, dynamics of heat release and heat transfer through the heat exchanger walls, inevitable phase change, and other variable parameters and phenomena.

This dissertation introduces the methodology for modelling of two-component two-phase natural convection and thermal stratification phenomena in a cooling pool using CFD software. The modelling methodology was developed based on the results of the two international experiments. The first experiment is a case where the heat exchangers are placed in a horizontal position in the cooling pool (horizontal heating surface) and this case corresponds to the component of the passive cooling system being installed in advanced new generation nuclear power plants. The second experiment is a case of cooling of a pressurised water reactor that has been shut down, opened, and ready for overload (vertical heating surface).

Relevance of the work

It is important to understand processes, to predict steady or changing situations, and to manage potential or unexpected accidents when a powerful industrial unit is operated. Passive cooling systems that do not require an external power source during critical situations and accidents are being installed or designed in advanced industrial facilities in order to prevent or minimise the potential consequences of such accidents. This issue is particularly relevant in nuclear power plants because the potential consequences of accidents at these facilities can be severe. Natural convection and thermal stratification phenomena, which occur in cooling pools of passive systems are closely interrelated and their behavior affects the safety of the installations, and they always have been of interest and remain relevant to engineers, inspectors, and researchers. Currently, there is a growing interest in modelling of these phenomena using CFD software, however, these phenomena are modelled using a lot of simplifications. There is no detailed and complex modelling methodology for these phenomena available today or it has not been published.

Object of the research

The two-component two-phase natural convection and thermal stratification phenomena in thermal installations.

Aim of the work

To develop the methodology for modelling of two-component two-phase natural convection and thermal stratification phenomena in thermal installations using CFD software.

Tasks of the work

1. To create numerical models of the experimental facilities with horizontal and vertical heating surfaces.
2. To determine the influence of initial and boundary conditions and numerical model parameters on modelling results during the modelling of natural convection and thermal stratification phenomena in the experimental facilities.
3. To create and describe in the programming language the UDF designed to define the dynamics of heat release on heating surfaces.
4. To prove the appropriateness of the developed methodology by modelling the experiments that represent two-component two-phase natural convection and thermal stratification phenomena in a cooling pool and to analyse the obtained results.

Novelty of the work

- The methodology for modelling of two-component two-phase natural convection and thermal stratification phenomena in thermal installations using CFD software was developed based on modelling of the two experiments. Until now, these phenomena assuming a lot of simplifications are modeled using CFD software.
- The developed methodology allows evaluating not single-phase fluid, but two-phase (two-component) fluid in one analysed system with variable thermodynamic-physical properties of this fluid. As well as allows evaluating the interaction between different fluids, transient and phase transition processes, and heat transfer through solid structures.

Practical significance of the research

The developed methodology allows performing complex numerical investigations of two-component two-phase natural convection and thermal stratification phenomena using CFD software. The methodology can be applied for modelling of these phenomena, which occurs in power or industrial installations (in the cooling pool of the passive system, in the spent nuclear fuel pool, in the nuclear or chemical reactor, etc.), facility or installation safety assessment, development of accident management methodology, etc. The second application of this methodology is its use in the process of creating and developing CFD programmes.

Statement presented for defense

1. The $k - \varepsilon$ realizable turbulence model with enhanced wall treatment more accurately simulates the thermal stratification phenomenon than the $k - \omega$ SST turbulence model.
2. The implementation of solid structures in the numerical model has a significant influence on modelling results of two-component two-phase natural convection and thermal stratification phenomena.

3. A special UDF described in programming language and implemented in the numerical model is a suitable numerical tool in order to define the dynamics of heat release on heating surfaces.
4. The developed methodology allows performing complex modelling of two-component two-phase natural convection and thermal stratification phenomena in complex configuration geometries.

Approbation of dissertation

Two scientific articles on the theme of the dissertation have been published in journals with a citation index at the “Clarivate Analytics” database “Web of Science Code Collection” and five scientific articles have been published in proceedings of international conferences. The results of the research were presented at five international conferences.

Structure and content of the dissertation

The dissertation work consists of the following chapters: introduction, literature review, the methodology of CFD simulations, description of experimental facilities and CFD models, results and discussion of numerical investigations, conclusions, references, list of scientific articles published on the theme of the dissertation, and two appendixes. General information on the content of the dissertation is as follows: 98 pages, 86 figures, 8 tables, and 77 references.

1. LITERATURE REVIEW

The natural convection and thermal stratification phenomena, a detailed overview of the most popular CFD software to solve these and other phenomena related to nuclear safety, and an overview of the public scientific articles related to numerical investigations of the natural convection and thermal stratification phenomena using CFD software are presented and discussed in this chapter.

1.1. Natural convection phenomenon

Natural (or free) convection is a type of mass and heat transport in which the fluid motion is generated only by the density difference of a fluid due to temperature change or gradient. Natural convection occurs due to temperature change or gradient, not by any external force source (like a pump, fan, suction device, etc.). In natural convection, a fluid surrounding a heat source receives heat and due to thermal expansion becomes less dense and rises. In other words, heavier (more dense) components will fall, while lighter (less dense) components rise, leading to bulk fluid movement. Natural convection can only occur in a gravitational field or in the presence of another proper acceleration, such as acceleration, centrifugal force, or the Coriolis force (1).

In natural convection, the flow is characterised by the Gr and Ra numbers. Usually, the density decreases due to an increase in temperature and causes the fluid to rise. The buoyancy force causes this motion. The major force that resists this motion is the viscous force. The Gr number characterises the ratio of the buoyancy to a viscous force acting on a fluid and has the following form (2, 3):

$$Gr = \frac{g\beta'\Delta TL^3}{\nu^2} \tag{1}$$

The boundary layer is laminar in the range $10^3 < \mathrm{Gr} < 10^6$, transition in the range $10^8 < \mathrm{Gr} < 10^9$, and turbulent $\mathrm{Gr} > 10^9$.

The Gr number is closely related to the Ra number, which is defined as the product of the Gr and the Pr numbers. The Pr number characterises the relationship between momentum diffusivity and thermal diffusivity. The Ra number is used to express heat transfer in natural convection and is a good indication where the natural convection boundary layer is laminar or turbulent. According to References (4, 5) the flow is laminar if $\mathrm{Ra} < 10^6$, the transition region is large and varies between $10^6 \div 10^{10}$, and turbulent if $\mathrm{Ra} > 10^9$. The Ra number has the following form (6):

$$Ra = \frac{g\beta'\Delta TL^3}{\nu a} = Gr \cdot Pr \tag{2}$$

Provided that forced or natural convection can be neglected for a system, the ratio of the Gr number to the square of the Re number can be used for the characterisation. This characteristic ratio is called the Ri number and has the following form (7):

$$Ri = \frac{g\beta'\Delta TL}{v^2} = \frac{Gr}{Re^2} \tag{3}$$

If the Ri < 1, then natural convection can be neglected. If the Ri > 1, then forced convection can be neglected. If the Ri ≈ 1, then the regime is combined forced and natural convection.

1.2. Thermal stratification phenomenon

Thermal stratification is formed in horizontal fluid layers with different fluid temperatures, where the warmer fluid layers are located above the cooler fluid layers. Thermal stratification occurs due to the change in fluid density with temperature. However, thermal stratification can be greatly disturbed by the undesirable and uncontrolled water flows, which stirs the otherwise thermally separated layers together and mixes them into a uniform temperature (8). Different parameters are used to measure the level of thermal stratification phenomenon. The most used are Charging energy efficiency, the Re number, the Mix number, Lost capacity, and others (9–17). The main disadvantage of these parameters is that they are used for solar water heating systems where inlet and outlet and steady-state condition exists. These parameters are not used for a "free surface" storage tanks where only one surface corresponds to the inlet and outlet at the same time and transient boundary condition exists.

The temperature distribution along the height of the storage tank at different time intervals can be used to evaluate the level of thermal stratification for a "free surface" storage tank. It is simply plotted and the temperature profiles represent a thermal gradient from the to the bottom of the storage tank. A larger temperature difference implies a larger temperature gradient and hence a larger level of thermal stratification (9, 18).

The Str number is another parameter in order to evaluate the level of thermal stratification. The Str number was defined as the ratio of the mean of the temperature gradients at any time to the maximum mean temperature gradient (9, 10, 16):

$$Str = \frac{(\partial T/\partial y)_t}{(\partial T/\partial y)_{t=0}} \tag{4}$$

The Ri number, mentioned in Section 1.1. can be used to evaluate the level of thermal stratification modifying Equation 3 to the following form (9, 15, 17, 19):

$$Ri = \frac{g\beta'(T_{top} - T_{bottom})L}{v^2}; \tag{5}$$

where ΔT is modified to: T_{top} – is the temperature at the top of the storage tank (K) and T_{bottom} – is the temperature at the bottom of the storage tank (K).

A small Ri number means a mixed storage tank, while a larger Ri number means a stratified storage tank. Similarly, the Ra number also can be modified and used to evaluate the level of thermal stratification. Nevertheless, the temperature distribution along the height of the storage tank is the best and the simplest way to compare the level of thermal stratification for a "free surface" storage tank with transient boundary condition. This parameter is useful when numerical results are compared with experimental data.

1.3. Overview of the most popular CFD software

Computers have been used to solve fluid flow problems for many years. From the mid-1970s, the complex mathematics required to generalise the algorithms began to be understood and general CFD solvers were developed. These CFD solvers began to appear in the early 1980s and required very powerful computers, in-depth knowledge of fluid dynamics, and large amounts of time to prepare set-up for simulations. Therefore, CFD solvers were used almost only in research.

Year by year, the advance of computing power, solvers, models, and graphics have made the progress of CFD modelling and analysis of results less complex, as well as reduced time and cost. Advanced solvers together with HPC enable robust solutions in a reasonable time. Today, CFD software is widely used as an industrial and research tool (20).

There are a lot of CFD codes, which can be used to analyse the flow fields numerically; nevertheless, these CFD codes have their advantages and disadvantages. Almost all CFD software solves the same problems and descriptions of this software are similar in their websites. ANSYS Fluent / CFX, OpenFOAM, STAR-CCM+ and STAR-CD, FLOW-3D, PHOENICS, COMSOL Multiphysics, and Code Saturne are the most popular CFD software related to nuclear industry and research (21).

1.3.1. ANSYS Fluent

ANSYS Fluent has powerful modelling capabilities: to model fluid flow, heat transfer, turbulence, reactions, airflow over an aircraft wing, combustion, bubble columns, oil platforms, blood flow, etc. This software is written in the C computer language, therefore, it can be automated using journal and scripting files and widely used in commercial and academic organisations. A large advantage of ANSYS Fluent is 2D modelling, Shell Conduction model, Porous Media, Simplified Heat Exchanger Model, dynamic mesh, etc. (22). The software also enables mesh refinement based on the flow solution.

ANSYS Fluent offers highly scalable, HPC helps to solve complex and large CFD problems quickly and cost-effectively. This software set a world supercomputing record by scaling to 172000 cores (23).

1.3.2. ANSYS CFX

ANSYS CFX software is a high-performance general-purpose CFD programme that is applied to solve a wide range of fluid flow problems for over 20 years. Due to advanced solver technology, software achieves reliable and accurate solutions quickly and robustly. This software can capture virtually any type of phenomena related to fluid flow. Furthermore, the software has a modern, intuitive, and flexible GUI and user environment with extensive capabilities for customisation and automation using session files, scripting, and expression language (20, 24). Compared to the same developer product called ANSYS Fluent, ANSYS CFX has some disadvantages, namely the lack of opportunities to solve 2D problems, to use ROM, Density-Based Coupled Solver, and Solution-Adaptive Mesh Refinement, to overset mesh, to model Shell Conduction, Simplified Heat Exchanger Model, Porous Media, Macroscopic

Particle Model, etc. ANSYS CFX has fewer capabilities comparing to the ANSYS Fluent according to Reference (25). ANSYS CFX software in the nuclear safety field is used quite often.

1.3.3. OpenFOAM

OpenFOAM is a free and open-source CFD software. This software is quite new – debut was in 2004 and now it has a lot of users from commercial and academic organizations. OpenFOAM can model a wide range of fluid flows involving chemical reactions, turbulence, heat transfer, acoustics, solid mechanics, etc. (26). One of the advantages of OpenFOAM is that software and parallel licenses are free of charge, while other CFD software is quite expensive. Another advantage of OpenFOAM is C++ programming language, which allows for a CFD user to create his own models provided that a CFD user understands not only the thermal-hydraulics phenomena but also the C++ programming language. It may be the reason why there are not many scientific articles related to nuclear safety topics and especially to numerical investigations of passive cooling systems in NPPs.

1.3.4. STAR-CD and STAR-CCM+

STAR-CD software was created for the development of internal combustion engines. This software has been actively involved with in-cylinder analysis from its inception and there are many engines in production now that have benefitted from using STAR-CD. In-cylinder processes such as turbulence, heat transfer, two-phase flow, evaporation, spray, combustion, chemistry, and turbulence-chemistry interactions, real-gas effects, etc., are key STAR-CD software phenomena (27).

STAR-CCM+ software is used for simulations of electromagnetics, heat transfer, multiphase and particle flows, aerodynamic, reacting flows, solid mechanics, and rheology. Also, the software focuses on the aerodynamics of cars, wind turbines, motorbikes, buildings, etc. (28). In other words, it is the same software as STAR-CD and is a powerful tool for aerodynamics simulations.

1.3.5. FLOW-3D

FLOW-3D is a highly-efficient and comprehensive CFD software, which specialises in solving transient and free-surface problems. This software is the most used by engineers, who investigating the dynamic behaviour of liquids and gas in industrial installations or nature (for example river and dam-break flows) (29).

1.3.6. PHOENICS

PHOENICS is typical CFD software, which has been used for different kinds of simulations that involve multiphase flows, heat transfer, chemical reactions, particle tracking, ventilation and acclimatisation, smoke dispersion, etc. (30). The developers of PHOENICS software published the list of the scientific articles (31) in order to show how widely the software is used.

1.3.7. COMSOL Multiphysics

COMSOL Multiphysics is a wide-range simulation software for modelling designs, devices, and processes in all fields of engineering, manufacturing, and scientific research. This software has different modules such as electromagnetics, structural mechanics and acoustics, fluid flow and heat transfer, chemical engineering, etc. These modules allow performing complex simulations of solving problems (32).

1.3.8. Code Saturne

Code Saturne is the free and open-source software developed to solve CFD problems. Code Saturne can solve 2D and 3D flows, steady and transient, laminar and turbulent, incompressible and weakly dilatable, isothermal, and not isothermal problems. RANS and Large-Eddy Simulation models are available. Specific physical models are available: combustion, radiative heat transfer, particle-tracking, electrics arcs, atmospheric flows, etc. (33).

1.3.9. Performance of different CFD software

It is difficult to assess the performance of these different CFD software for solving the CFD problem. Keshmiri, A. et al. (34) performed the benchmark of CONVERT, STAR-CD, and Code Saturne in simulating natural, forced, and mixed convection flows. The first case was a mixed convection flow in a vertical pipe. The second case was natural convection in an enclosed tall cavity. Despite differences in the numerical procedures used by each software, good agreements were obtained for velocity and temperature gradients between the CFD software. Meanwhile, some discrepancies were found in both cases for the Reynolds shear stress and turbulent kinetic energy gradients.

Due to the complex nature of the CFD software, it is difficult to identify all the sources that would contribute to the discrepancies in the results. Therefore, it is difficult to choose the proper CFD software for the CFD problem.

1.4. Numerical investigations of natural convection and thermal stratification phenomena in the rectangular enclosures by other authors

Many investigations have been performed to analyse the natural convection phenomenon in enclosures for different geometries, boundary conditions and fluids using CFD codes. The doctoral thesis focused on the CFD investigations of the two-component two-phase natural convection and thermal stratification phenomena in rectangular enclosures within horizontal cylindrical heating elements and heat transfer through solid structures (the conjugate heat transfer). Different researchers have been analysing these phenomena using different approaches, assumptions, and simplifications. Two-dimensional and three-dimensional modelling approaches could be distinguished.

Numerical simulations of natural convection phenomenon using two-dimensional approach (Fig. 1.1) for different thermal boundary conditions, Richardson and Rayleigh numbers, diameters and positions of a cylindrical heating element in rectangular enclosures, were performed by many researchers.

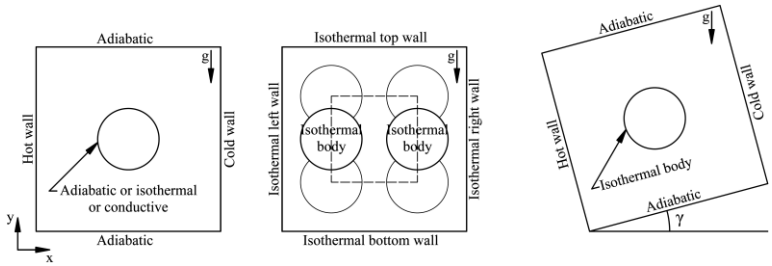

Fig. 1.1. The examples of 2D models for numerical investigations of natural convection phenomenon (35–42)

Oztop, H.F. et al. (35) studied mixed convection characteristics for a lid-driven air flow within a square enclosure, which has a circular body. The left wall of the square enclosure moves up or down in y-direction while the other walls remain stationary. Different boundary conditions were applied for the walls and the circular body. It was found that the most effective parameter on flow and temperature fields is the orientation of the moving wall. The circular body can be as a control parameter for heat and flow fields. Park, Y.G. et al. (36) carried out a numerical investigation of natural convection induced by a temperature difference between a cold outer square enclosure and two hot inner cylinders. This study investigated the effects of the locations of the two cylinders in the enclosure on the heat transfer and laminar fluid flow when they move in a vertical direction along the centreline. It was found that the bifurcation of natural convection from steady to the unsteady state depends on the Ra number and the dimensionless vertical distance from the square cylinder center to the circular cylinder center of the two cylinders. When $10^3 \leq Ra \leq 10^5$, the flow and thermal fields reached steady state and flow and thermal fields became unsteady at $Ra = 10^6$. The same authors (37, 38) studied the same phenomena, but the difference from the previous investigation is that the two cylinders were placed in a vertical position in a square enclosure, and another case is that the four cylinders were placed in a square enclosure. Kang, D.H. et al. (39) investigated the effect of the location of an inner heated cylinder along a horizontal or diagonal line in a cooled enclosure on the fluid flow and heat transfer for a $Ra = 10^7$. The flow and thermal fields change from the steady or unsteady to the unsteady or steady state at critical positions on both the horizontal and the diagonal lines. The major origin of the unsteady state depends on the position of the cylinder. The unsteadiness near the upper corners, the centre of the enclosure, and the lower corners is governed by a series of cells, and the inner vortices periodically merging and separating within the enlarged lower primary eddy. The variation in the local Nusselt number of the cylinder and enclosure is dominated by the gaps between the inner heated cylinder and the cooled enclosure, the upwelling and downwelling thermal plumes, and the upward returning flow. Mun, G.S. et al. (40) carried out numerical simulations of natural convection heat transfer induced by the temperature difference between cold walls of the tilted square enclosure and a hot inner cylinder for $10^{-2} \leq Pr \leq 10^2$ and $10^3 \leq Ra \leq 10^6$. The outer square enclosure is tilted $\gamma = 0° \div 45°$. It was found that the unsteady characteristics of the flow and thermal fields occurs at $10^5 \leq Ra \leq 10^6$ and $0.01 \leq Pr \leq 0.1$ regardless

of the tilted angle of the enclosure due to the increase in the flow instability except the cases for $Ra = 10^5$ and $Pr = 0.1$ at $15° \leq \gamma \leq 30°$. The Pr number is directly depended only on the fluid and fluid state. The entropy generation rates due to heat transfer and fluid friction increases very slightly for $10^3 \leq Ra \leq 10^4$. The degree of the irreversibility produced in the system is similar regardless of the variation in the tilted angle of the enclosure at the same Ra and Pr numbers. At relatively low Ra numbers $10^3 \leq Ra \leq 10^4$, the irreversibility in the system is dominantly produced by the heat transfer. Similar phenomena were studied by the same authors (41) as in the previous study, nonetheless, the study focused on not tilted square enclosure. Choi, C. et al. (42) studied the effect of a cylinder location on natural convection in a rhombus enclosure for $10^3 \leq Ra \leq 10^7$. The inner hot cylinder location is vertically changed along the rhombus enclosure centerline. They identified three thermal and flow regimes: steady-symmetric, steady-asymmetric, and unsteady-asymmetric. The distribution of the thermal and flow regimes was presented as a function of the dimensionless off-centre distance and the Ra number. The characteristics of the heat transfer between the cylinder and the enclosure also depend on the location of the cylinder and the value of the Ra number. As convection magnitude becomes larger than its magnitude for lower Ra numbers, the difference in the thermal and flow fields occurs.

The most numerical simulations of natural convection and thermal stratification phenomena using three-dimensional approach usually are performed on similar conditions compared to the ones for two-dimensional numerical simulations (Fig. 1.2, Fig. 1.3).

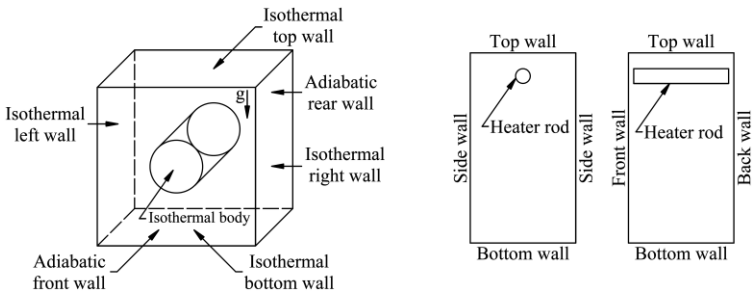

Fig. 1.2. The examples of 3D models for numerical investigations of natural convection phenomenon (43–46)

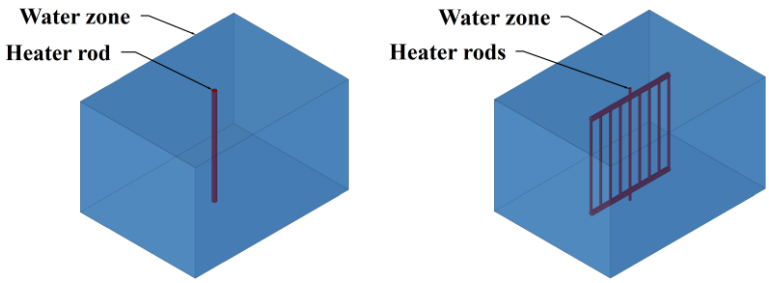

Fig. 1.3. The examples of 3D models for numerical investigations of thermal stratification phenomenon (47)

Seo, Y.M. et al. (43) carried out three-dimensional numerical investigations of the natural convection around the heated cylinder located in the cold cubic enclosure for $10^3 \leq Ra \leq 10^6$ at $Pr = 0.7$. The radius of the inner cylinder varied in $0.1L \leq R \leq 0.4L$. According to their research, the numerical solution shows the time-independent characteristics, and the flow and thermal structures have almost a two-dimensional structure regardless of the variation of the cylinder radius. When the cylinder radius increases to $R = 0.3L$ at $Ra = 10^6$, the flow experiences a transition from the steady state to the unsteady state. When the cylinder radius increases from $R = 0.2L$ to $R = 0.3L$ at $Ra = 10^6$, the space that the spanwise vortex occupies is confined and hence the flow instability is intensified. When the cylinder radius increases to $R = 0.4L$ from $R = 0.3L$ at $Ra = 10^6$, the space in which the fluid is filled is extremely confined. Lee, S.H. et al. (44) also studied three-dimensional numerical investigations of the natural convection around the heated cylinder located in the cold cubic enclosure with sinusoidal thermal boundary conditions for $Ra = 10^5$ and $Ra = 10^6$ at $Pr = 0.7$. It was found that if the hot inner cylinder is located at the center of the enclosure at $Ra = 10^5$, the flow and thermal fields reach the steady state with the mirror-symmetric pattern. Then the distribution of local Nusselt numbers at the walls of the enclosure does not depend much on the sinusoidal temperature variation at the bottom wall. If the inner cold cylinder is located at the center of the enclosure, the mirror-symmetric pattern of isotherms is broken, and the isotherms and streamlines rotate in the counter-clockwise direction. The distribution of local Nusselt numbers depends on the position and size of the counter-clockwise rotating ascending plumes, which is a function of the sinusoidal temperature variation on the bottom wall. When $Ra = 10^6$, the distribution of flow and thermal fields becomes time-dependent for both cases of the presence of the hot and cold inner cylinder. Souayeh, B. et al. (45) numerically investigated three-dimensional natural convection of air induced by a temperature difference between a cold outer cubic enclosure and a hot inner cylinder. Numerical investigations were carried out for $10^3 \leq Ra \leq 10^7$ and a titled angle of the enclosure varying from 0° to 90°. It was found that the distribution of isocontours of temperature, components of velocity and streamtraces eventually reaches a steady state for $10^3 \leq Ra \leq 10^7$ for titled inclination of 90°. However, for the remaining inclinations, Ra numbers must be in the range $10^3 \div 10^6$ to avoid unsteady state, which is manifested by the subdivision of the area, containing the maximum local heat transfer rate, into three parts for $Ra = 10^7$ and inclination of 90°. The optimal average heat transfer rate is obtained for $Ra = 10^6$ and an inclination of 90° for both cases of the inner cylinder and lateral walls of the cubic enclosure. Kumar, A. et al. (46) investigated the transient two-dimensional and three-dimensional simulations of natural convection of air around a cylinder enclosed in a box of 1000 mm x 600 mm x 1200 mm for $Ra = 1.3 \cdot 10^6$. It was found that the distance between the cylinder and the top wall is an important parameter, which affects the nature of the flow. 3D vortices were observed when the H*/D ratio was 0.2 and these vortices helped in enhancing the heat transfer in the region between the cylinder and the ceiling as it was shown in the comparison between the two-dimensional and three-dimensional simulations. For H*/D=0.4, 1, and 2.3, the difference between the results of two-

dimensional and three-dimensional simulations was very small. The authors also analysed the other researcher's studies by two-dimensional and three-dimensional simulations. Gandhi, M.S. et al. (5, 47) carried out the numerical and experimental investigation of two-phase natural convection and thermal stratification with boiling phenomena in a rectangular tank fitted with a single tube and a 10 tubes assembly. The phenomena were analysed for $4.34 \cdot 10^{11} \leq Ra \leq 2.59 \cdot 10^{14}$. It was found that the fractional vapor hold-up increases from zero to 0.097 % for single tube and 0.35 % for the 10 tubes assembly. At $Ra = 4.34 \cdot 10^{11}$ and $Ra = 5.9 \cdot 10^{11}$, was no difference between the CFD predictions of single-phase and two-phase models. An increase of Ra number has substantial influence on the liquid flow rate, therefore, high values of mixing time indicate that mixing is poor and thermal stratification occurs. Good agreement was found between the values of heat transfer coefficient obtained from experimental measurements and the developed mathematical model. Other numerical and experimental investigations performed by Gandhi et al. (48) were dedicated to two-phase natural convection and thermal stratification with boiling phenomena in a cylindrical vessel with different heating tube designs. The phenomena were analysed for $9.37 \cdot 10^{10} \leq Ra \leq 5.57 \cdot 10^{13}$. The results show that the natural convection is feeble, the rates of mixing and heat transfer are low, and the thermal stratification level is high. Reduction in the aspect ratio causes reduction in the heat transfer rate and some reduction in the thermal stratification. The presence of the appropriate size of the draft tube enhances the overall liquid circulation velocity and reduces the mixing time and the stratification number. Attachment of baffles to the plain tube provides radial flow, which in turn causes the mixing of hot and cold fluids.

Solid structures, representing walls of a rectangular enclosure are rarely considered in CFD simulations of the natural convection and thermal stratification phenomena. However, solid structures have a significant influence on the results of CFD simulations. Kelm et al. (49) performed ANSYS CFX validation and comparative assessment of two different experiments (the TH22 test of the German THAI and the NATHCO test of the French MISTRA experimental facilities) on the buoyancy-driven mixing processes. In the case of buoyant flows, the results of CFD simulations reveal that the heat transfer process between the fluid and solid structures have significantly influenced the CFD simulation results. In order to predict a reliable heat transfer process, the near-wall gradients need to be resolved sufficiently. Furthermore, the definition of solid structures used in CFD simulations is very important and significantly influences the local circulation flow rate of fluids mixing as well as the heat transfer process. Papukchiev, A. and Buchholz, S. (50) performed validation of ANSYS CFX for gas and the liquid metal flows with the conjugate heat transfer. They analysed thermal-hydraulic processes in two experimental facilities (L-STAR and TALL-3D). Numerical simulations of the TALL-3D facility show that solid structures in the CFD model are necessary in order to obtain high-quality modelling results. Solid structures introduce thermal inertia and should be involved in transient simulations. In addition, the results of simulation showed that significantly lower mesh resolution is needed for solid structures, comparing with the fluid region.

Also, with the additional solid domain, CFD simulations can converge faster than the ones without it.

1.5. Summary of literature review and the formulation of scientific problems

The importance of passive cooling systems has significantly increased after the Fukushima accident on March 11, 2011. Researchers pay more attention to numerical investigations of thermal-hydraulic processes in passive cooling systems using CFD software. The methodology used for numerical investigations is not fully developed and still has limitations.

The above literature survey clearly shows that two-dimensional and three-dimensional numerical investigations of natural convection and thermal stratification phenomena are often performed taking into account simplifications such as:

1. Single-phase flow;
2. The fluid flow is incompressible;
3. The Boussinesq approximation is used for the definition of fluid density;
4. Performing simulations at steady-state (not evaluating transients) conditions;
5. The effects of solid wall(s) location and thickness (conjugate heat transfer) are neglected;
6. Fluid properties are constant except in the formulation of buoyancy term;
7. Two-dimensional simulations or three-dimensional simulations with only a half or a quarter of geometry were performed.

The most numerical investigations of the natural convection and thermal stratification phenomena in the passive cooling systems, in the passive cooling pool or the spent nuclear fuel pool were performed according to these simplifications and are not accurate enough. Therefore, in order to perform more accurate and reliable predictions of thermal-hydraulic accidents in nuclear power plants using CFD software, a more developed methodology is needed.

In this thesis, the experimental data obtained from the scientific articles (8, 51, 52) was used as a base to create the methodology for numerical investigations of two-component two-phase natural convection and thermal stratification phenomena in rectangular enclosures using the CFD software. Unlike numerical investigations by many other authors, these phenomena were simulated in detail. The full-scale computational domains of the experimental facilities were created. Full transient calculations were performed. Many sensitivity investigations were performed for CFD models of Osaka University and KAERI experimental facilities. Furthermore, the special UDF's for heating rates of the heated surfaces were created. Two-component two-phase flow, generation of water vapor bubbles around the heated surfaces, evaporation, and condensation phenomena were included in these numerical investigations.

The thesis is written based on the experience gained in the CFD groups for nuclear safety during the six-weeks internship in the GRS research center (2016) and six-months internship in the NRG research center (2018), and based on the knowledge obtained during the European Nuclear Safety Training and Tutoring Institute courses related to nuclear safety.

Author's contribution

The author of the dissertation analysed the scientific data on the two-component two-phase fluid natural convection and thermal stratification phenomena in rectangular enclosures with a cylindrical heating element, and numerical investigations of these phenomena using the CFD software. Based on two experiments and using ICEM CFD and ANSYS Fluent software, detailed numerical models of the experimental facilities were created and two-component two-phase fluid natural convection and thermal stratification phenomena were numerically investigated. The author developed the methodology for complex numerical investigations of the above-mentioned phenomena using the CFD software. In order to define the dynamics of heat release on heating surfaces, a special UDF described in programming language and implemented in numerical models was created. To determine the influence of initial and boundary conditions and numerical model parameters on modeling results, the author performed the sensitivity analysis.

2. METHODOLOGY OF CFD SIMULATIONS OF NATURAL CONVECTION AND THERMAL STRATIFICATION PHENOMENA

This chapter introduces the methodology created for numerical investigations of the two-component two-phase natural convection and thermal stratification phenomena in rectangular enclosures using the CFD software. An overview is given on the selection of the CFD software, ANSYS Fluent mathematics, geometry and mesh generation, near-wall and turbulence modelling, and multiphase modelling including the evaporation and condensation model. The governing equations needed to be solved numerically are described. The requirements for stable and converged transient calculation are introduced. In order to enhance modelling capabilities, a brief introduction to UDF is presented in the last section.

2.1. Selection of CFD software and computing resources

To perform numerical investigations of the natural convection and thermal stratification phenomena in rectangular enclosures, the most appropriate CFD software must be selected.

The geometries and meshes of the experimental facilities will be generated using the ICEM CFD software. The first reason why ICEM CFD software was chosen is that generated mesh consists of hexahedral cells only. In most cases, the best numerical results are obtained when the mesh of the CFD model consists of hexahedral cells. The second reason was that ICEM CFD software has very powerful meshing capabilities comparing with the other meshing software. For example, the ANSYS Mesh software has many limitations and fewer options in hexahedral mesh generation. The third reason was that a lot of knowledge was gained on using the ICEM CFD software during the internships in the GRS research center.

The first reason why the ANSYS Fluent software was chosen is that the ANSYS Fluent software has powerful and wide modelling capabilities (described in Section 1.3.1), which can be enhanced by incorporating UDFs, comparing with other CFD software. Calculations can be automated using journal and scripting files. The second reason was that the most numerical investigations related to nuclear safety were performed using the ANSYS Fluent software according to the public scientific articles. The third reason was that the ANSYS Fluent software with HPC helps to solve complex and large CFD problems quickly and cost-effectively. The fourth reason was that LEI manages the newest ANSYS Fluent user licenses together with 256 parallel licenses for HPC. Also, LEI manages the HPC cluster, which together with the ANSYS Fluent software provides huge computing power. The fifth reason was that a lot of knowledge was gained on using the ANSYS Fluent software during the internships in GRS and NRG research centers. Thus, the ANSYS Fluent 17.2 version (53, 54) and HPC cluster SGI Altix ICE 8400 were used for numerical investigations. The HPC cluster SGI Altix ICE 8400 consists of the 20 nodes, where each node has 48 GB of random access memory and 12 cores (3.33 GHz).

2.2. The mathematics of ANSYS Fluent software

For all flows, the ANSYS Fluent solves the conservation equations for mass and momentum. If flows involve heat transfer or compressibility, then additional energy equation is solved. The domain is discretised into a finite set of control volumes, where conservation equations are solved on this set of control volumes. Partial differential equations are discretised into algebraic equations when algebraic equations are solved numerically to render the solution fields. The ANSYS Fluent has two solver technologies: pressure-based and density-based. Pressure-based solver is used for the most problems, where Mach number varies between 0 and 2÷3. Pressure-based solver has two algorithms: a segregated algorithm and a coupled algorithm. In the segregated algorithm, the governing equations are solved one after another. Each iteration consists of the steps illustrated in Fig. 2.1. Also, when solving heat transfer, turbulence, or multiphase problem, the double-precision solver is recommended (54).

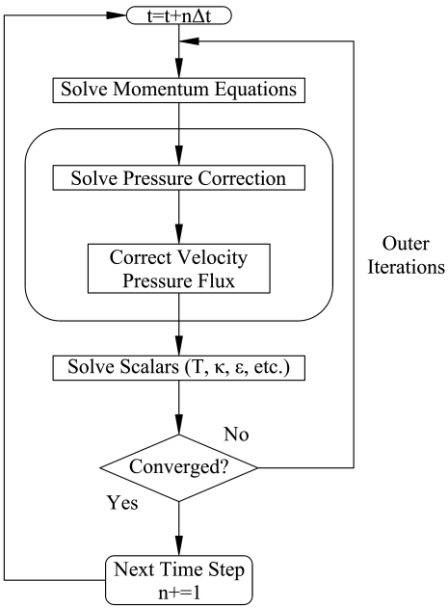

Fig. 2.1. Segregated algorithm scheme in the transient calculation manner (54)

2.3. Geometry and mesh generation

The geometries and hexahedral meshes of the experimental facilities will be created using ICEM CFD software, taking into account OECD/NEA Best Practice Guidelines (55, 56), ECORA (57), ERCOFTAC (58) and ANSYS (59) recommendations.

Mesh quality has a strong influence on the overall calculation (e.g. velocity, temperature and density gradients, computational speed, and resources, converge, etc.). The aim of the mesh generation procedure is to find the best compromise between accuracy, efficiency, and easiness way to generate the mesh. The mesh must be able to capture heat transfer, flow gradients, boundary layers, etc. The acceptable

mesh quality parameters are presented in Table 1. It is important to avoid large changes in mesh density and recommended using hexahedral cells. More accurate results can be obtained using hexahedral cells than tetrahedral cells, or another type of cells, with the same size of cells. The study of mesh independence must be performed in each numerical investigation, before starting the final calculation.

Table 1. Mesh parameters of the computational model (59)

Parameter	The acceptable value
The smallest cell size	–
The biggest cell size	–
Mesh quality	> 0.3
Minimum angle of a cell	> 20.0
Aspect ratio	< 100.0
Skewness	< 0.8
Orthogonal quality	> 0.2
Expansion rate	< 20.0%
Cells type	–

2.4. Near-wall modeling

Mesh generation near the wall has a strong impact on the gradients in the boundary layer. Velocity, temperature, turbulence, etc., variables change rapidly in the boundary layer. In order to correctly capture gradients in the boundary layer, the non-dimensional distance from the wall (Y^+) can be used to calculate the size of the first mesh cell near the wall. The equations for the Y^+ calculation are presented in Reference (60). Boundary layer regions are presented in Fig. 2.2. In the viscous sublayer, the flow is laminar and the viscosity plays an important role in heat and mass transfer, momentum, etc. In the buffer layer, the effects of molecular viscosity and turbulence are equally important. In the fully turbulent region, the turbulence plays a major role.

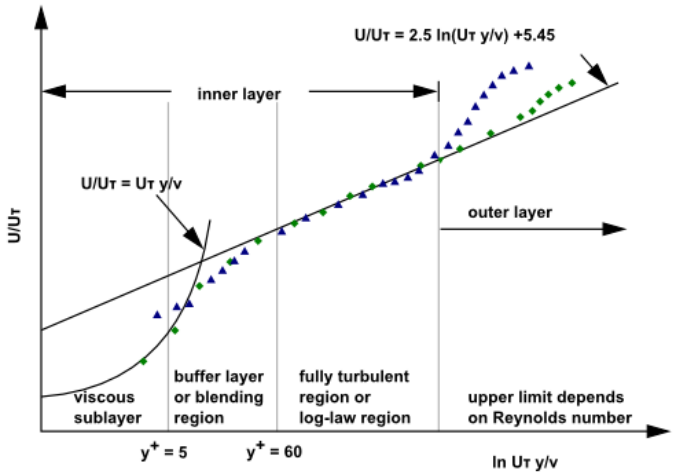

Fig. 2.2. Near wall region (60)

There are two approaches to modelling the near-wall region. In the first approach, the viscous sublayer and buffer layer are not resolved. Semi-empirical equations so-called “wall-functions” are used to connect the wall and the fully turbulent region eliminating the viscous sublayer and buffer layer. In the second approach, the viscous sublayer is resolved by the fine mesh near the wall and this approach is called “near-wall”. These approaches are presented schematically in Fig. 2.3.

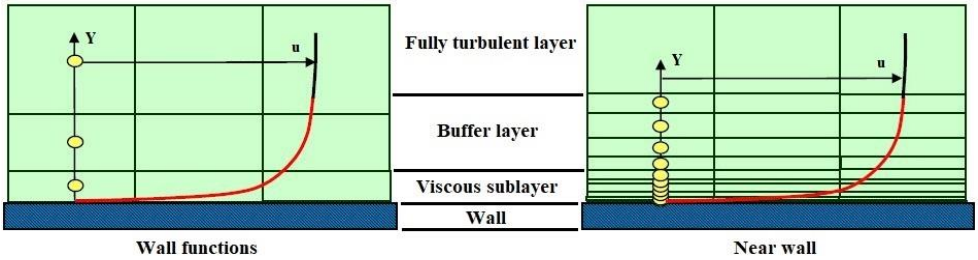

Fig. 2.3. Mesh resolution near walls (60)

In cases, where near-wall modelling is not needed wall functions can be used. Usually, wall functions are used where all attention is focused on mixing in the middle of the domain. Using wall functions, the first cell must be located in the log-layer region ($30<Y^+<300$) and wall functions should be never used below $Y^+<30$. Almost in all CFD problems, the most important region is the viscous sublayer. In the viscous sublayer (near-wall modelling), the size of the first mesh cell needs to be about $Y^+\approx1$ and the other mesh parameters according to Table 1. In order to model a viscous sublayer, the correct turbulence model should be chosen. The $k-\omega$ models and $k-\varepsilon$ models with enhanced wall treatment are used to solve the viscous sublayer according to the ANSYS manuals (53, 54) and recommendations (60).

As mentioned above, the equations for the Y^+ calculation are presented in Reference (60). These equations are the preliminary assessment of the size of the first mesh cell near the wall. However, the real value of the Y^+ can be found only during the calculation by plotting the contour fields of the Y^+ value. If the Y^+ value is too high, it is necessary to refine the mesh.

2.5. Turbulence modelling

Turbulence is a flow regime in which the three-dimensional motion becomes unstable above a certain Re number. The motion becomes intrinsically unsteady even with constant boundary conditions. The velocity and all other flow properties vary in a random and chaotic way. A decomposition of the flow velocity in mean velocity is presented in Fig. 2.4.

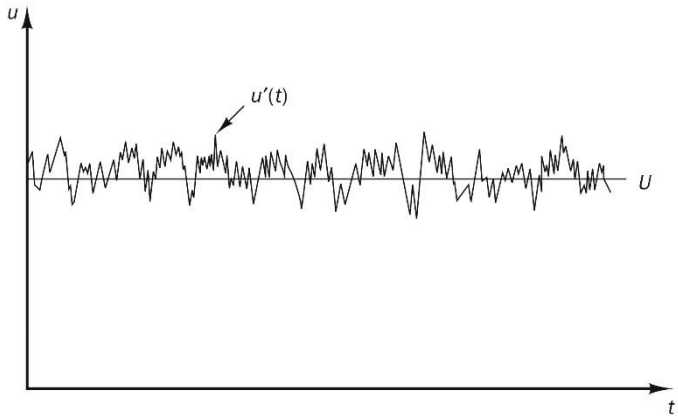

Fig. 2.4. Typical velocity in turbulent flow (61)

Turbulence is described by the Navier-Stokes equations, impossible in most problems to resolve the wide range of scales in time and space by direct numerical simulation due to huge computing resources needed. For this reason, averaging procedures have to be applied for Navier-Stokes equations in order to filter out all parts of the turbulent spectrum. Reynolds-averaging is the most applied averaging procedure of the equations, resulting in the RANS equations. All turbulent structures are removed from the flow and a smooth variation of the averaged velocity and pressure can be obtained. The reliability of the calculation depends on the selected turbulence model; therefore, it is important to choose the proper model as well as to create the proper mesh for the selected model (53).

The most popular RANS based models are two-equation models: $k-\varepsilon$ group (Standard, RNG, Realizable) and $k-\omega$ group (Standard, BSL, SST). The most advanced turbulence models are $k-\varepsilon$ realizable and $k-\omega$ SST. The $k-\varepsilon$ realizable turbulence model is suitable for complex shear flows, moderate swirl, vortices, and locally transitional flows. The $k-\omega$ SST turbulence model is suitable for boundary layer flows under adverse pressure gradient and separation, free shear, low Re number flows (60). The $k-\varepsilon$ realizable turbulence model with enhanced wall treatment (near-wall modelling) was chosen for numerical investigations (54, 60). In addition, the influence on the results of the $k-\omega$ SST as well as $k-\varepsilon$ standard turbulence models was tested.

2.6. Multiphase modelling

A large number of flows in nature and technology are a mixture of phases. The physical phases of matter are gas, liquid, and solid. Multiphase flows can be grouped in these categories: gas-liquid or liquid-liquid; gas-solid; liquid-solid; three-phase flows. The first step in solving the multiphase problem is to determine which category (flow regime) best represents the analysed problem. According to the literature review and the descriptions of the experimental facilities, in this thesis, the analysed problem belongs to the gas-liquid category, where the flow regime is stratified/free-surface flow (flow of immiscible fluids separated by a clearly-defined interface) (54).

There are two approaches for numerical investigation of multiphase flow at this moment: the Euler-Lagrange and the Euler-Euler approaches. In the Euler-Lagrange approach, the fluid phase is treated as a continuum by solving the Navier-Stokes equations, while the dispersed phase is solved by tracking a large number of particles, bubbles, or droplets through the calculated flow field. The dispersed phase can exchange momentum, mass, and energy with the fluid phase. This Euler-Lagrange approach is used for discrete phase modelling. In the Euler-Euler approach, the different phases are treated mathematically as interpenetrating continua. Since the volume of a phase cannot be occupied by the other phases, the concept of phasic volume fraction is introduced. These volume fractions are assumed to be continuous functions of space and time and their sum is equal to one. Conservation equations for each phase are derived to obtain a set of equations, which have a similar structure for all phases. These equations are closed by providing constitutive relations that are obtained from empirical information, or, in the case of granular flows, by application of kinetic theory. This Euler-Euler approach is used for typical multiphase problems and has three different multiphase models: VOF, Mixture, and Eulerian (54). The VOF model is necessary in order to simulate the two-phase natural convection and thermal stratification phenomena in the experimental facilities (8, 51, 52) as the flow regime is free-surface flow.

2.6.1. The VOF model

The VOF model is designed for two or more immiscible fluids where the interface between the fluids is a place of interest. In this model, a single set of governing equations is shared by the phases and the volume fraction of each fluid in each mesh cell is tracked throughout each of the CFD models. The VOF model formulation assumes that two or more fluids (or phases) are not interpenetrating. For each additional phase, the volume fraction of the phase in the mesh cell is introduced. The sum of the volume fractions of all phases is equal to 1 in each mesh cell. The fields for all variables and properties are shared by the phases and represent averaged values as well as the volume fraction of each of the phases is known at each location of the computational domain. The variables and properties of one of the phases, or a mixture of the phases, in all mesh cells are shown according to the volume fraction values (Fig. 2.5). For example, the two-phase system consists of air (q^{1st}) and water-liquid (q^{2nd}) phases. The volume fraction of q^{1st} in the mesh cell is denoted as α_{1st}, and q^{2nd} is denoted as α_{2nd}, respectively. Then three conditions are possible:

1. If mesh cells contain pure air, when $\alpha_{1st} = 1$ and $\alpha_{2nd} = 0$;
2. If mesh cells contain pure water-liquid, when $\alpha_{1st} = 0$ and $\alpha_{2nd} = 1$;
3. If mesh cells contain $0 < \alpha_{1st} < 1$ and $0 < \alpha_{2nd} < 1$, when the interface between the q^{1st} and q^{2nd} phases are visible.

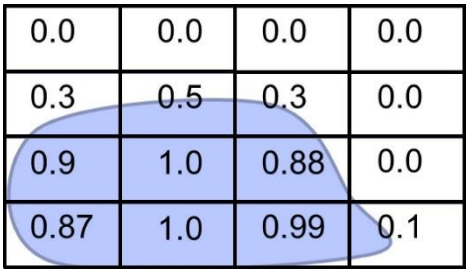

Fig. 2.5. Theoretical distribution of the qth in mesh cells calculated by the VOF model (54)

The VOF model is applied for modelling of stratified/free-surface flows, tank filling, waves in open channels, the motion of bubbles in a liquid, etc. Generally, the VOF model is used to perform transient calculations and must be used with the pressure-based solver. All mesh cells must be filled by a single fluid phase or combination of phases. Only one phase can be specified as a compressible ideal gas (recommended to set "first-phase" as an ideal gas). The only first-order implicit scheme can be used for transient formulation (54).

2.6.2. Evaporation and condensation modelling

Evaporation and condensation phenomena, within the VOF model, can be simulated using the Lee model or UDFs created by the CFD user. In this thesis, Lee model was chosen. In the Lee model, the mass transfer (evaporation and condensation) is governed by the vapor transport equation (54):

$$\frac{\partial}{\partial t}(\alpha_v \rho_v) + \nabla \cdot \left(\alpha_v \rho_v \overrightarrow{V_v}\right) = \dot{m}_{lv} - \dot{m}_{vl} \tag{6}$$

As shown in Equation 3, the ANSYS Fluent defines positive mass transfer from the liquid to the vapor. The mass transfer can be described as follows, if $T_l > T_{sat}$ (evaporation):

$$\dot{m}_{lv} = coef\ f\ \cdot \alpha_l \rho_l \frac{(T_l - T_{sat})}{T_{sat}} \tag{7}$$

and, if $T_v < T_{sat}$ (condensation):

$$\dot{m}_{vl} = coef\ f\ \cdot \alpha_v \rho_v \frac{(T_{sat} - T_v)}{T_{sat}} \tag{8}$$

2.6.3. Governing equations

Tracking of the interface(s) between the phases is accomplished by the solution of the continuity equation for the volume fraction of one (or more) of phases. The equation of qth phase has the following form (54):

$$\frac{\partial}{\partial t}\left(\alpha_q \rho_q\right) + \nabla \cdot \left(\alpha_q \rho_q \vec{v}_q\right) = S_{a_q} + \sum_{p=1}^{n}\left(\dot{m}_{pq} - \dot{m}_{qp}\right) \tag{9}$$

The volume fraction equation solved through explicit time formulation and discretised in the following form:

$$\frac{\alpha_q^{n+1}\rho_q^{n+1}-\alpha_q^n\rho_q^n}{\Delta t}V+\sum_f\left(\rho_q U_f^n \alpha_{q,f}^n\right)=\left[\sum_{p=1}^n\left(\dot{m}_{pq}-\dot{m}_{qp}\right)+S_{a_q}\right]V \quad (10)$$

A single momentum equation has the following form:

$$\frac{\partial}{\partial t}(\rho\vec{v})+\nabla\cdot(\rho\vec{v}\vec{v})=-\nabla p+\nabla\cdot[\mu(\nabla\vec{v}+\nabla\vec{v}^T)]+\rho\vec{g}+\vec{F} \quad (11)$$

The energy equation, as well as the momentum equation, is shared among phases:

$$\frac{\partial}{\partial t}(\rho E)+\nabla\cdot\left(\vec{v}(\rho E+p)\right)=\nabla\cdot\left(k_{eff}\nabla T\right)+S_h \quad (12)$$

The VOF model treats total energy (E) and temperature (T) as mass-averaged variables:

$$E=\frac{\sum_{q=1}^n \alpha_q\rho_q E_q}{\sum_{q=1}^n \alpha_q\rho_q} \quad (13)$$

In Equation 10, the total energy for q phase (E_q) has the following form:

$$E_q=h-\frac{p}{\rho}+\frac{v^2}{2}; \quad (14)$$

where enthalpy (h) is defined for ideal gases (air phase) as:

$$h=\sum_s M_s h_s \quad (15)$$

and for incompressible flows (water phase) as:

$$h=\sum_s M_s h_s+\frac{p}{\rho} \quad (16)$$

In Equations 12 and 13, enthalpy of species s (h_s) has the following form:

$$h_s=\int_{T_{ref}}^T c_{p,s}dT \quad (17)$$

The transport equations for the $k-\varepsilon$ realizable model:

$$\frac{\partial}{\partial t}(\rho k)+\frac{\partial}{\partial x_j}\left(\rho k u_j\right)=\frac{\partial}{\partial x_j}\left[\left(\mu+\frac{\mu_t}{\sigma_k}\right)\frac{\partial k}{\partial x_j}\right]+G_k+G_b-\rho\varepsilon-Y_M+S_k \quad (18)$$

and

$$\frac{\partial}{\partial t}(\rho\varepsilon)+\frac{\partial}{\partial x_j}\left(\rho\varepsilon u_j\right)=\frac{\partial}{\partial x_j}\left[\left(\mu+\frac{\mu_t}{\sigma_\varepsilon}\right)\frac{\partial\varepsilon}{\partial x_j}\right]+\rho C_1 S_{rst}\varepsilon-\rho C_2\frac{\varepsilon^2}{k+\sqrt{\nu\varepsilon}}+C_{1\varepsilon}\frac{\varepsilon}{k}C_{3\varepsilon}G_b+S_\varepsilon \quad (19)$$

The transport equations for the $k-\omega$ SST model:

$$\frac{\partial}{\partial t}(\rho k)+\frac{\partial}{\partial x_i}(\rho k u_i)=\frac{\partial}{\partial x_j}\left(\Gamma_k\frac{\partial k}{\partial x_j}\right)+G_k-Y_k+S_k \quad (20)$$

and

$$\frac{\partial}{\partial t}(\rho\omega)+\frac{\partial}{\partial x_j}\left(\rho\omega u_j\right)=\frac{\partial}{\partial x_j}\left(\Gamma_\omega\frac{\partial\omega}{\partial x_j}\right)+G_\omega-Y_\omega+D_\omega+S_\omega \quad (21)$$

2.7. Convergence

Solving a complex mathematical system is difficult and the CFD user may encounter stability and converge problems. All conservation equations in all control volumes (cells) have to satisfy specified convergence (tolerance) criteria. Convergence criteria are equal to 10^{-6} for energy and 10^{-4} (to obtain more reliable solution 10^{-5}) for continuity, k, omega, X, Y, and Z velocities in standard ANSYS Fluent settings. The residuals measure these imbalances and the residuals curves must decrease below these convergence criteria. In other words, the overall mass, energy, momentum, and scalar balances must be achieved. The solver must perform enough iteration in order to achieve a converged solution. Convergence can be judged by residuals curves and monitors (e.g. temperature, velocity, turbulence, pressure, etc., monitoring point or monitoring surface). When the residuals curves decrease below the convergence criteria (Fig. 2.6) and the chosen target quantities (the monitors) such as mass flow rate, heat flux, etc., become constant (Fig. 2.7), the CFD user can assume that solution is fully converged.

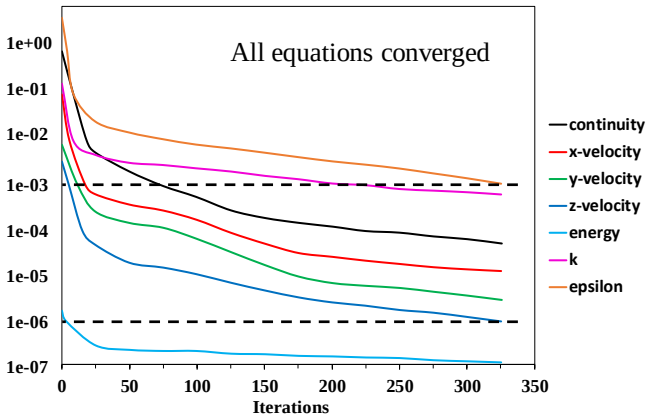

Fig. 2.6. Convergence according to residuals curves (62)

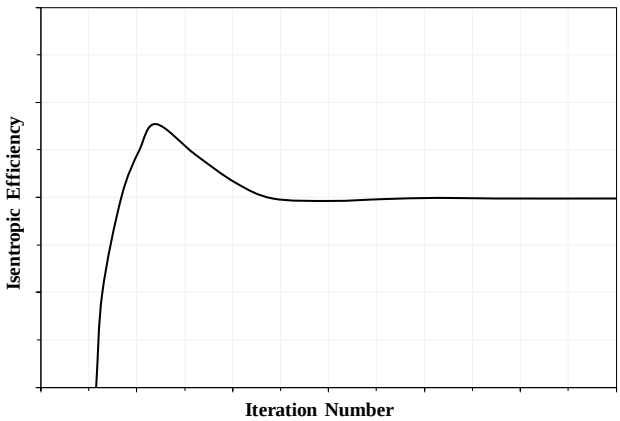

Fig. 2.7. Convergence according to the chosen target quantity (62)

Stability problems could arise with wrong initial conditions, poor quality mesh, or inappropriate solver settings. The increase (or "stuck") in residuals indicates diverging, stability problems, and imbalance in governing equations. These solution results are misleading. Such stability problems can be solved by ensuring that the initial conditions are well-posted, decreasing under relaxation factors for equations that have convergence problems, remesh or refine cells that have poor quality cells.

2.8. Transient calculation

All flows in nature are unsteady and many problems (e.g. aerodynamics, multiphase flows, unsteady heat transfer, etc.) require performing unsteady calculation. CFD calculation can be performed under steady-state (the influence of time not evaluated) or transient condition (the influence of time is evaluated). Usually, most thermal-hydraulic experiments have been analysing changes of processes in time, therefore, the transient calculation is necessary. In order to perform successful transient calculation and achieve a converged solution, many requirements for transient calculation must be satisfied, more inputs are required, and deep knowledge of transient calculation is necessary. The transient calculation is solved by computing a solution for many discrete points in time. At each point in time, the solver must perform as many iterations as needed to achieve a converged solution (Fig. 2.1).

The time step size is a very important parameter in transient calculations. The time step size must be small enough to resolve time-dependent problems. A too large time step can cause stability and convergence problems, however, a large time step size generates less solution (or so-called "data") files and calculation takes less CPU time. Meanwhile, a smaller time step size can ensure better stability and convergence of calculation, nevertheless, larger solution files are generated and the calculation takes more CPU time. The CFL number can be used to estimate a time step size. The CFL number gives the number of mesh elements the fluid passes through in one time step. Usually, in order to resolve mean flow physical time scales under transient condition, the CFL number should be not higher than 1 and have the following form:

$$CFL = \frac{U\Delta t}{\Delta x} \tag{22}$$

Residuals plot for transient calculation not always indicate a converged solution. The time step size must be chosen that the residuals decrease by 2–3 orders of magnitude within one time step (Fig. 2.8). For smaller time steps, residuals may decrease by 1–2 orders of magnitude. It is better to use the smaller time step size than more iterations in one time step. The time step size should be such that the residuals satisfy the convergence criteria with around 5–10 maximum iterations per time step. According to these recommendations (63), it is a good idea to go "on testing way", for example, to set 50 iterations per time step and "to play" with time step size until the time step size will be proper. There is another way to set the time step size using a variable time stepping method, which automatically calculates the CFL number and the time step size, nevertheless, this method requires additional knowledge. Command lines with specified time steps sizes are the best way to manage transient calculation based on calculation stability and convergence.

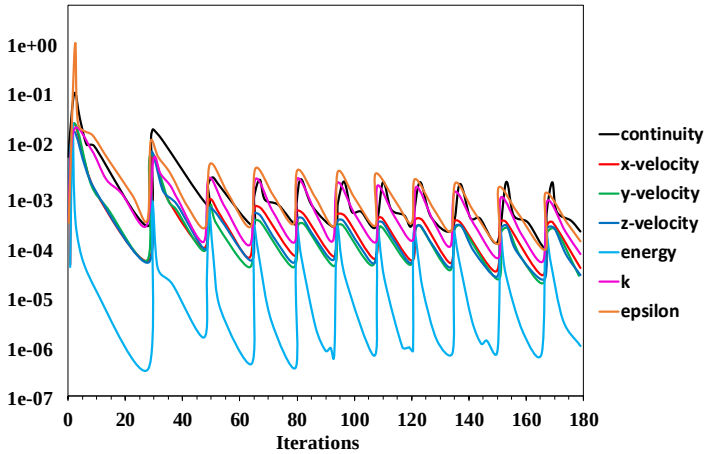

Fig. 2.8. Example of residuals of transient calculation (~15 iterations per time step) (63)

2.9. UDF for heating

A UDF is a function(s) constructed in the C programing language, which can be loaded directly to the ANSYS Fluent solver in order to enhance modelling capabilities. UDFs can be used to specify mass, momentum, and energy sources, as well as variable boundary conditions such as variable heat flux through the wall, variable mass flow through the inlet, etc. Specific models such as chemical reactions, mass transfer, heat transfer correlations, etc., can be created in UDFs, nonetheless, it requires deep knowledge of phenomena and creation of UDFs (64). In other words, almost all numerical investigations of thermal-hydraulic phenomena in experimental facilities under transient condition require specially created UDF(s) for each kind of experimental facility.

3. DESCRIPTION OF EXPERIMENTAL FACILITIES AND CFD MODELS

First, the design of the different experimental facilities and the description of the experiments are presented within this chapter. Then, a lack of information needed for successful numerical investigations and numerical models of the experimental facilities is described. Variable/constant thermal-physical properties of the water-liquid, water-vapor, and air are presented. Finally, the UDF, which describes the thermal power rate of the heater rod(s) and has been developed during the PhD studies and incorporated in the CFD models is presented.

3.1. Introduction to KAERI experimental facility

After the Fukushima accident on 11 March 2011, the importance of a passive safety system for the reactor, containment and spent fuel pool heat removal was highlighted. Many advanced NPPs are designed incorporating a passive safety system now. In order to incorporate a passive safety system, the evaluation of heat removal capacity is required for system design and safety analysis. Large pools of water near atmospheric pressure provide a heat sink to remove heat from the reactor, containment and spent fuel pool by natural convection (65, 66). In these water pools, due to the heat transfer process, a three-dimensional convection flow develops. Thermal stratification is increasingly encountered in large pools of water that is being used as heat sinks in the new generation NPPs.

Fig. 3.1 shows a schematic view of the PAFS, which is an example of a passive safety system and was adopted in the advanced power reactor plus (APR+). The PCCT and PCHXs are few parts of many parts that constitute full PAFS. Due to heat transfer from the PCHXs, which are placed in a horizontal position in the bottom part of the PCCT, water temperature increases up to saturation temperature and forms natural convection flow inside the PCCT. When the heat transfer process from the PCHXs starts, the temperature of the water near the PCHXs starts to increase. During this process, the density of water decreases and water moves upward due to the buoyancy force. After reaching the free surface, the warmer water moves toward the other sidewall of the PCCT, along the free surface. During the moving along the free surface, warmer water cools down and while mixing with colder water moves downward along the wall at the other side of the PCCT. Natural convection forms above the PCHXs, meanwhile there is no flow below the PCHXs and thermal stratification occurs. Thermal stratification disappears and water becomes well mixed when the water temperature reaches saturation temperature (8, 51).

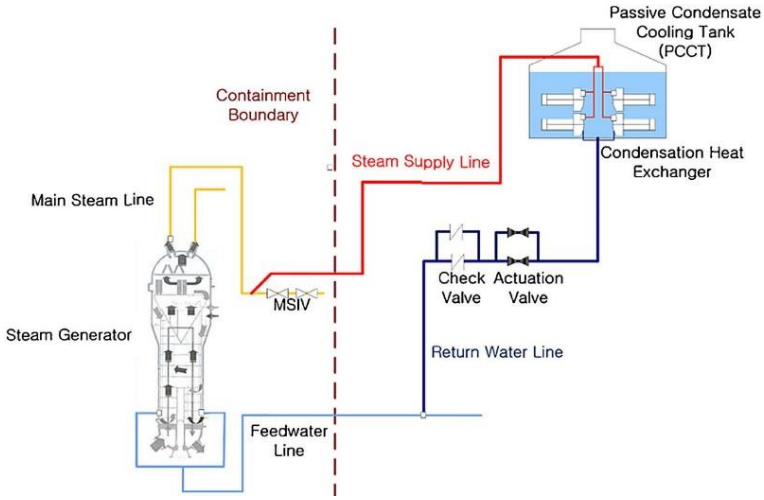

Fig. 3.1. A schematic view of the PAFS (8)

In order to investigate natural convection and thermal stratification phenomena as well as multi-dimensional local flow velocity, turbulence intensity, and energy, the KAERI created an experimental facility, which represents the PCCT within PCHXs. It is the rectangular enclosure within heater rod placed in the horizontal position at the bottom part of the rectangular enclosure (8, 51).

3.1.1. Description of the KAERI experimental facility

The rectangular enclosure consists of the single heater rod, solid walls, and 2D PIV measurement technique. The horizontal cylindrical heater rod inside the rectangular enclosure was designed to produce natural convection and thermal stratification phenomena. The working fluid in this facility is the de-ionised water (for the PIV measurements). The length of the rectangular enclosure is 300 mm, width – 60 mm, and height – 650 mm. The heater rod, which is 19.05 mm diameter, is placed in a horizontal position, 85 mm above the bottom. The total length of the heater rod is 160 mm: 150 mm is heating part and 10 mm at the end of the rod is a non-heating part. The back wall is made from 15 mm thick polycarbonate, the front and right walls are made from 3 mm thick pyrex glass, and for the bottom and left walls the 20 mm thick stainless steel “304” is used. A 3D view of rectangular enclosure construction is shown in Fig. 3.2. Five thermocouples (TF-01÷TF-05) in the rectangular enclosure and 25 thermocouples (TW-01÷TW-25) on the rectangular enclosure walls were installed to monitor and record thermal changes during the experiments. The TF-01÷TF-05 thermocouples were placed in the centre of the rectangular enclosure, except the TF-02 thermocouple, which was placed 2 mm away from the heater rod surface. A schematic drawing of the rectangular enclosure and the positions of TF-01÷TF-05 thermocouples are shown in Fig. 3.3.

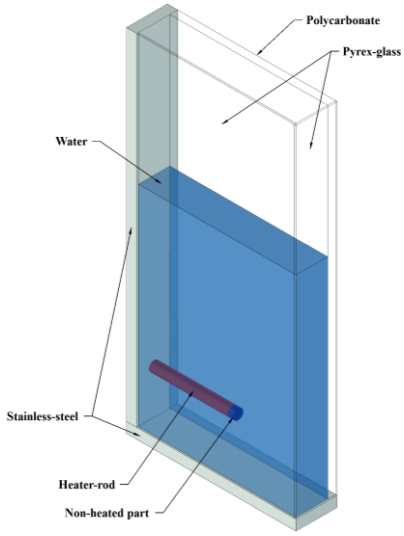

Fig. 3.2. A 3D view of the rectangular enclosure

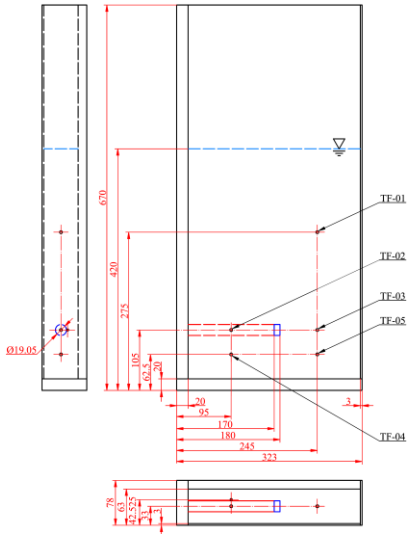

Fig. 3.3. Drawing of the rectangular enclosure (dimensions in mm)

3.1.2. Initial and boundary conditions of the KAERI experiment

The experiment takes five hours. The initial de-ionised water, rectangular enclosure walls, and the ambient temperature is approximately 15 °C. The rectangular enclosure is filled with water up to a 400 mm level. Thermal power of the heater rod is 600 W. The insulation could not be used on the walls due to the employment of the PIV measurement technique, heat losses through the walls had to be evaluated. These losses were evaluated by comparing the amount of heat supplied to the water (given electrical power) and the real increase of the water enthalpy and the time spent to reach the saturation temperature. The estimated average heat loss during the time

interval, when the water temperature increased from 20 ℃ to 90 ℃, was approximately 310 W (51).

3.1.3. Lack of information

In References (8, 51), there is no information about the construction of the experimental facility walls. It is difficult to understand how the walls are connected to each other. Neither the thermal-physical properties of the walls nor the picture of the experimental facility is provided. Furthermore, a detailed investigation of heat losses during the experiment was not performed.

3.2. Introduction to the Osaka University experimental facility

In an accident of station blackout (which occurred in the Fukushima NPP) or loss of the heat removal system in the mid-loop operation during the shutdown of the pressurised water reactor, reactor core cooling has to occur by natural convection. Usually, heat flux has axial distribution in the nuclear fuel assembly, e.g. the top part of the fuel rod has a larger heat flux, while the upper part has a smaller heat flux. Under this assumption, the natural convection is limited to the upper part of the reactor vessel and thermal stratification is considered to occur. Therefore, detailed knowledge of natural convection and thermal stratification phenomena in vessels with axially distributed heat flux is indispensable (52).

In order to investigate natural convection and thermal stratification phenomena under these assumptions, the Osaka University researchers created the experimental facility, which represents the pressurised water reactor with a hot leg during the station blackout or loss of the heat removal system in the mid-loop operation during the shutdown. During these accidents, the pressure in the reactor vessel is almost equal to atmospheric pressure, the temperature is around 50 ℃ and the heating rate is at decay heat magnitude.

3.2.1. Description of the Osaka University experimental facility

The experimental facility (Fig. 3.4), which is a rectangular enclosure with an attached pipe, represents the pressure vessel and the hot leg of the reactor vessel. The walls of the rectangular enclosure and pipe are made from Lucite material and can be operated until 130 ℃. The width and length of the rectangular enclosure are 120 mm, the height is 550 mm. The pipe is a cylinder with an inner diameter of 30 mm and a length of 250 mm (Fig. 3.5). The pipe is attached 45 mm from the top of the rectangular enclosure and the end of the pipe is closed. The 25 heater rods were installed inside the rectangular enclosure. The nine heater rods were installed in the center part of the rectangular enclosure and are called centre rods, the 16 heater rods were installed in the peripheral part and are called peripheral rods, respectively. Each heater rod has a 10 mm diameter and a 100 mm heated section, located between altitudes of 0÷100 mm, while the rest length of the heater rods is unheated part (52).

Fig. 3.4. The experimental facility (52)

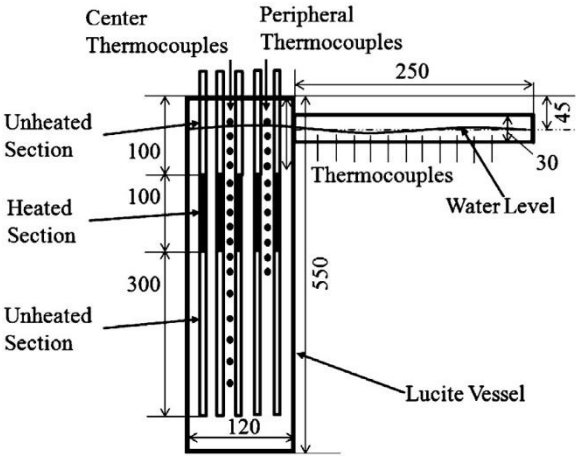

Fig. 3.5. A schematic view of the experimental facility (52)

The heater rods were placed in a square lattice with a pitch of 20 mm (Fig. 3.6). Heat flux was regulated by changing electricity input voltage to each heater rod. The centre and peripheral rods were regulated separately. 16 CA thermocouples were located in the centre sub-channel, 11 CA thermocouples in the peripheral sub-channel, 11 CA thermocouples in the pipe, respectively (Fig. 3.7).

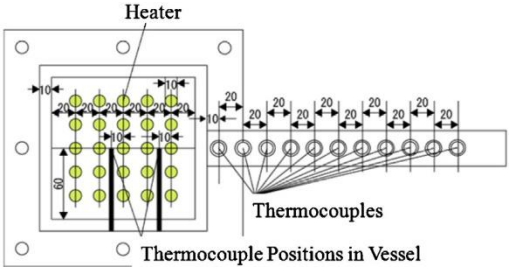

Fig. 3.6. Top view of the experimental facility (52)

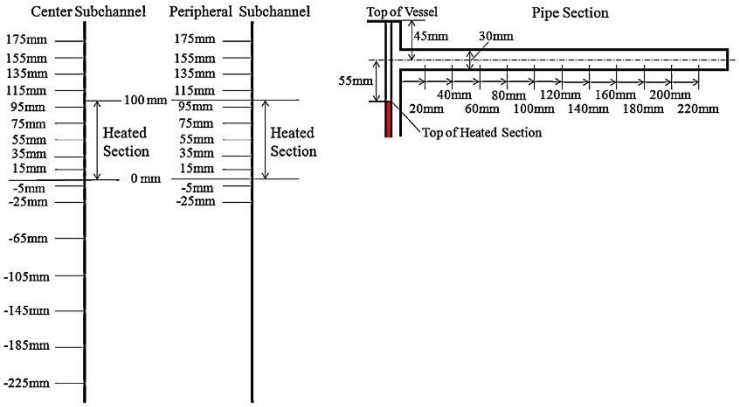

Fig. 3.7. Positions of the thermocouples (52)

3.2.2. Osaka University experiment initial and boundary conditions

The experiments were performed at atmospheric pressure under single-phase and two-phase natural convection conditions. The experiment takes 1357 seconds. The vessel was filled up with de-ionised water until 155 mm altitude, which corresponds half pipe of its diameter. The initial water temperature was around 9 ℃, the initial experimental facility and environment temperature was around 12 ℃, respectively. The thermal power of the heater rods was 4.4÷71.0 kW/m^2.

3.2.3. Lack of information

In Reference (52), there is no information about the thickness of the pipe walls and how the pipe walls are connected to the vessel walls. The thermal-physical properties of the walls are not provided in the KAERI experiment. Furthermore, a detailed investigation of heat losses during the experiment was not performed either.

3.3. A numerical model for KAERI experiment modelling

A full-scale geometry of the CFD model of the experimental facility was created using the ICEM CFD software. All solid walls were considered in this model and were meshed instead of using the Shell Conduction model, which treats walls as virtual walls. There are no symmetry planes. The main simplification is that the solid structure of the heater rod is not modelled. It means that the thermal inertia of the

heater rod was not considered in the CFD model, as it is not expected that thermal inertia of the heater rod can have an influence on results.

3.3.1. Mesh generation

The mesh, as well as geometry, was created using ICEM CFD software. In order to perform the mesh independence study, four different meshes (Fig. 3.8, Fig. 3.9) were created according to the mesh quality requirements and recommendations mentioned in Section 2.3. The most important locations in terms of meshing are the boundary layer near all surfaces and smooth cell size in overall geometry. A comparison of four different mesh parameters is presented in Table 2.

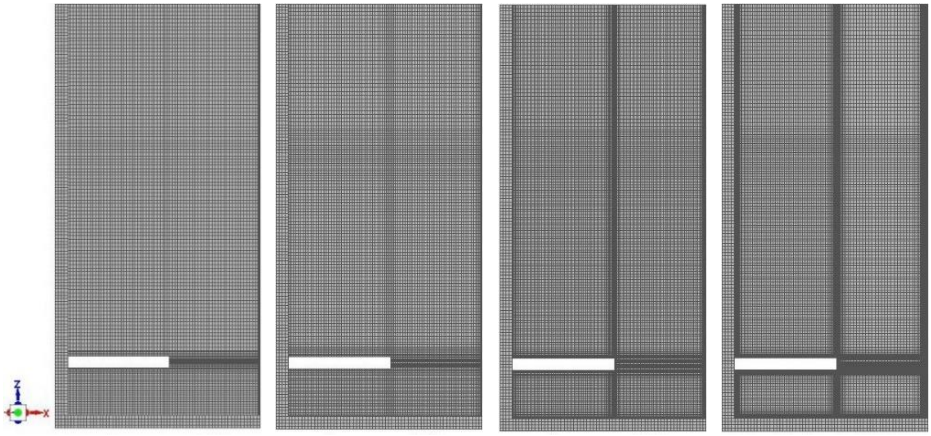

(a) (b) (c) (d)

Fig. 3.8. The contours of the mesh cells on the plane ZX: (a) 218313; (b) 313964; (c) 570610 and (d) 922736

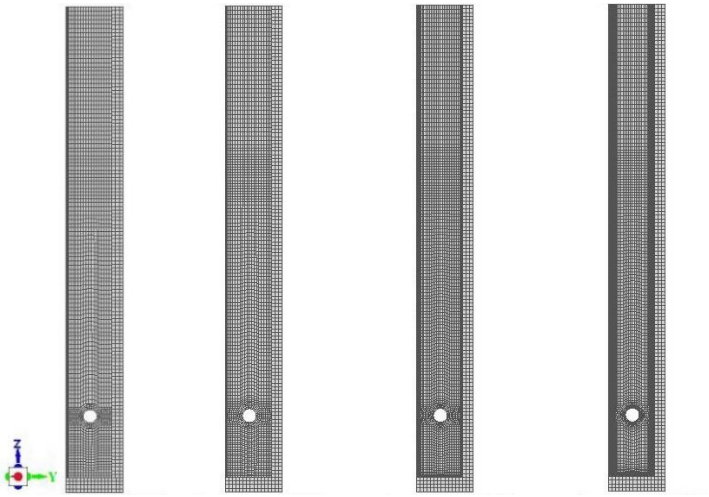

(a) (b) (c) (d)

Fig. 3.9. The contours of the mesh cells on the plane ZY: (a) 218313; (b) 313964; (c) 570610 and (d) 922736

Table 2. Mesh parameters of the computational model

Parameter	The acceptable value	218313	313964	570610	922736
The smallest cell size	–	1.96 mm	1.89 mm	1.41 mm	0.28 mm
The biggest cell size	–	9.87 mm	8.55 mm	7.15 mm	8.31 mm
Mesh quality	> 0.3	> 0.47	> 0.49	> 0.50	> 0.55
Minimum angle of a cell	> 20.0	> 50.10		> 49.52	
Aspect ratio	< 100.0	< 4.46	< 4.16	< 6.77	< 40.28
Skewness	< 0.8	< 0.23		< 0.24	
Orthogonal quality	> 0.2	> 0.77		> 0.76	
Expansion rate	< 20.0%	20.0%			
Cells type	–	Hexahedral			

3.3.2. Boundary and initial conditions of the CFD model for the KAERI experiment

The initial temperature of ambient air, water, and walls of the rectangular enclosure was set to 15 ℃. The water level in the enclosure is 400 mm. The thermal power of the heater rod was set to 600 W and regulated according to the UDF. Unfortunately, the exact range of heat transfer coefficients from the walls of the rectangular enclosure to the environment air during the experiment is unknown. Therefore, the heat transfer coefficient 18.95 W/m^2·K was applied for all the walls of the computational domain and was calculated according to heat losses during the experiment (51). Heat loss to ambient air was treated as the convection thermal condition (67). The calculations were performed until water started to boil in full volume, not only around heater rod, as in this case the time step size needed to properly simulate water boiling should be very small (~0.001÷0.005 sec). Generation of water vapor bubbles around the heater rod, evaporation and condensation processes were taken into account using the Lee evaporation-condensation model. The material properties of the rectangular enclosure walls are presented in Table 3.

Table 3. Material properties of the rectangular enclosure walls assumed in numerical simulation (68–70)

Properties	Polycarbonate	Pyrex-glass	Stainless steel “304”
Density, kg/m^3	1200	2230	8030
Specific heat, J/kg·K	1200	753	500
Thermal conductivity, W/m·K	0.19	1.1	16.2

3.4. A numerical model for the Osaka University experiment modelling

The creation strategy of the CFD model of the experimental facility was similar as described in Section 3.3. The CFD model of the experimental facility was split according to the symmetry plane using the ICEM CFD software. The first calculations will be made without the solid walls due to the mesh size, however, the solid walls will be considered in the last calculations. It was assumed that the solid structures of the heater rods are not modelled.

3.4.1. Mesh generation

The mesh was created using the ICEM CFD software. In order to perform the mesh independence study, the five different meshes (Fig. 3.10–Fig. 3.14) were created according to the mesh quality requirements and recommendations mentioned in Section 2.3. The size of the mesh cells was modified by a factor 1.5 from the initial mesh (463176 cells). Also, in order to ensure the same CFL number during the mesh independence study, the time step size was modified by a factor 1.5. The first four meshes are created without solid walls and the last mesh includes the solid walls. The most important locations in terms of meshing are the pipe region, the upper unheated region, the heated region, the small region under the heated region, where thermal stratification expected, and the boundary layer of the mentioned region is as well very important. A comparison of five different mesh parameters is presented in Table 4.

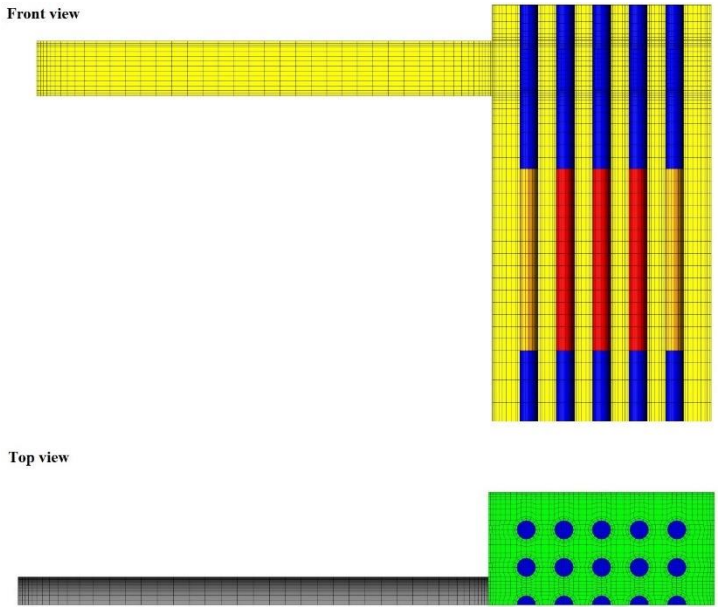

Fig. 3.10. The contours of the mesh cells (98550 cells)

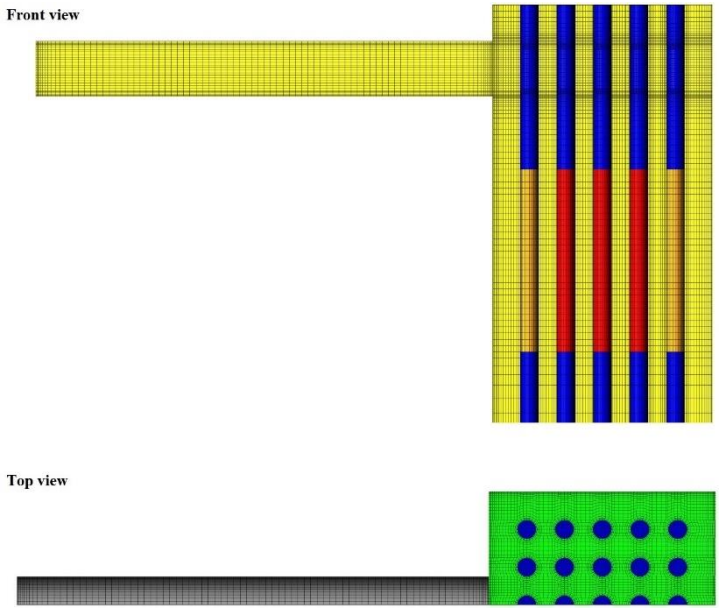

Fig. 3.11. The contours of the mesh cells (463176 cells)

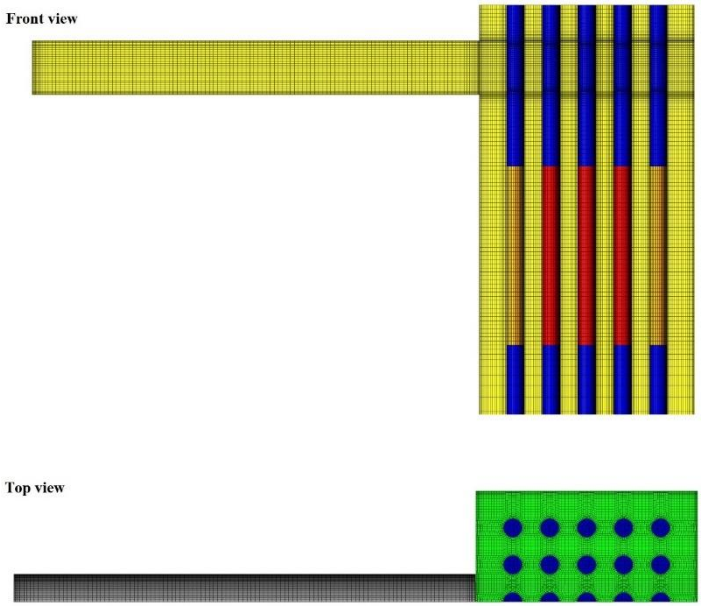

Fig. 3.12. The contours of the mesh cells (1125338 cells)

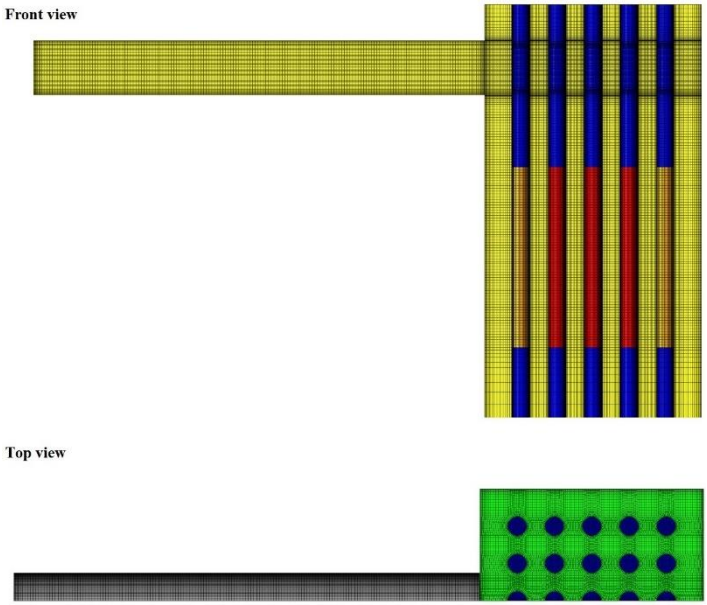

Fig. 3.13. The contours of the mesh cells (2763037 cells)

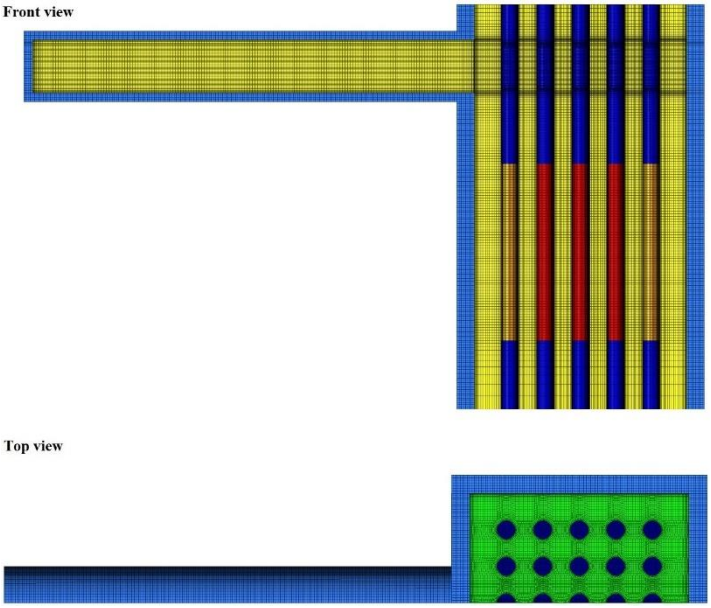

Fig. 3.14. The contours of the mesh cells (3478277 cells)

Table 4. Mesh parameters of the computational model

Parameter	The acceptable value	98550	463176	1125338	2763037	3478277
The smallest cell size	–	1.19 mm	0.60 mm	0.40 mm	0.27 mm	
The biggest cell size	–	31.83 mm	13.51 mm	13.97 mm	16.40 mm	
Mesh quality	> 0.30	> 0.47	> 0.52	> 0.56	> 0.54	
Minimum angle of a cell	> 20.00	> 41.49	> 37.60	> 35.15	> 33.62	
Aspect ratio	< 100.00	< 35.71	< 29.75	< 47.22	< 84.17	
Skewness	< 0.80	< 0.34	< 0.39	< 0.42	< 0.45	
Orthogonal quality	> 0.20	> 0.66	> 0.61	> 0.58	> 0.55	
Expansion rate	< 20.00 %	20.0 %				
Cells type	–	Hexahedral				

3.4.2. Boundary and initial conditions of the CFD model for Osaka University experiment

The initial water temperature is 9 ℃, ambient air is 12 ℃, respectively. The thermal power of the heater rods was set to 4.4 kW/m^2 and regulated using created UDF. The exact range of heat transfer coefficients from the walls of the rectangular enclosure to the ambient air during the experiment is unknown as well as during the KAERI experiment. The correct heat losses to environment air were searched by performing calculations using adiabatic conditions (HTC=0 W/m^2·K) and increasing HTC (the convection thermal condition) from 0 until 100 W/m^2·K. The generation of water vapor bubbles around the heater rods and evaporation and condensation processes were taken into account using the Lee evaporation-condensation model, however, it was not expected to capture these phenomena due to short time and low heat flux during the experiment. The material properties of the rectangular enclosure walls are presented in Table 5.

Table 5. Material properties of the rectangular enclosure walls assumed in numerical simulation (71)

Properties	Lucite
Density, kg/m^3	1180
Specific heat, J/kg·K	1810
Thermal conductivity, W/m·K	0.198

3.5. Numerical set-up

The VOF multiphase model for two-phase flow simulations and time-depended explicit formulation for volume fraction discretisation was chosen. The flow regime

in natural convection could be selected evaluating the Ra number. The Ra=$3.92 \cdot 10^{11}$ for the KAERI experiment and Ra=$6.17 \cdot 10^{9}$ for the Osaka University experiment were calculated according to Eq. 1. It was considered that natural convection is turbulent in both experiments.

The convergence criteria 10^{-6} for energy and 10^{-5} for continuity, k, omega, X, Y, Z velocities were applied. For calculations of the KAERI experiment, the variable time-stepping algorithm was used. The maximum CFL number was set to 1. The initial time step sized was 10^{-5} second with a 5 % increase until the CFL=1 was reached. For calculations of the Osaka University experiment, the fixed time-stepping algorithm was used. Special "calculation" file with text command lines was used to set the number of iterations, the time step size, and other commands related to stable and converged calculation.

The spatial discretisation settings used for numerical investigations are presented in Table 6. The discretisation equations were solved using Pressure-Implicit with Splitting of Operators (PISO) segregated algorithm.

Table 6. Spatial discretisation settings

Discretisation	Scheme
Gradient	Least Squares Cell-Based
Pressure	PRESTO
Density	Second-Order Upwind
Momentum	
Turbulent Kinetic Energy	
Specific Dissipation Rate	
Energy	
Volume Fraction	Geo-Reconstruct

3.6. UDF for heating

The UDFs were created and used for numerical investigations of the two-phase natural convection and thermal stratification phenomena in the KAERI and Osaka University experimental facilities in order to describe and regulate the thermal power rate of the heater rod(s). The mathematical form of thermal power rate of the heater rod(s) is presented below:

$$P = Q \cdot t; \tag{23}$$

where: P – total heat flux, W/m^2; Q – heat flux ratio per second until full thermal power will be reached, W/m^2; t – time, s.

This mathematical form was converted to the UDF and implemented to the CFD models of the KAERI and Osaka University experimental facilities:

```
/*==========================================================
 *
 * HEATING MODEL FOR VARIABLE SURFACE HEAT FLUX
 *
 * Created: 17 July 2018, A. Grazevicius, NRG, Petten, The Netherlands
 * Modified: 18 August 2018, A. Grazevicius, NRG, Petten, The Netherlands
```

```
 *
*==========================================================*/

#include "udf.h"

/* profile for variable wall heat flux */

DEFINE_PROFILE(heater_rods,t,i)
{
 face_t f;
 real flow_time = CURRENT_TIME;

 begin_f_loop(f,t)
  {
 /* heat flux linear increasing from beginning until A sec (heat flux B W/m2 / A sec
(C W / A sec)) */
   if (flow_time > A.) flow_time = A.;
     F_PROFILE(f,t,i) = D * flow_time;
  }
 end_f_loop(f,t)
}

/*----------------------------------------------------------*/
```

where: *A* – total time needed to reach full thermal power, sec; *B* – total heat flux, W/m^2; *C* – total integral heat flux, W; *D* – heat flux ratio per second until full thermal power will be reached, W/m^2; flow_time – time, s.

3.7. Thermal-physical properties of the fluids

For both numerical investigations of the KAERI and the Osaka University experiments, the real variable/constant thermal-physical properties of fluids (air, water-liquid and water-vapor) were chosen and these properties are presented in Table 7.

Table 7. Variable/constant thermal-physical properties of the fluids used in the numerical simulation (72–76)

Data point	Temperature, K	Density, kg/m^3	Specific heat, J/kg·K	Thermal conductivity, W/m·K	Dynamic viscosity, kg/m·s	Molecular weight, kg/kg·mol
Variable air thermal-physical characteristics						
1	273.15	Ideal-gas	1005	0.02364	$1.729 \cdot 10^{-5}$	28.97
2	333.15			0.02808	$2.008 \cdot 10^{-5}$	
3	393.15			0.03095	$2.181 \cdot 10^{-5}$	
Variable water-liquid thermal-physical characteristics						
1	273.15	999.8	4217	0.6	0.001792	18.02
2	293.15	998.0	4182		0.001002	
3	313.15	992.1	4179		0.000653	
4	333.15	983.3	4185		0.000467	
5	353.15	971.8	4196		0.000355	
6	373.15	957.9	4217		0.000282	
Constant water-vapor thermal-physical characteristics						
1	-	0.59	2026.7	0.0261	$1.2 \cdot 10^{-5}$	18.02

4. RESULTS AND DISCUSSION

In this chapter, the calculations of the KAERI and Osaka University experiments are presented and their results are discussed. Almost all calculations were treated as intermediate calculations, because different settings such as mesh sizes, turbulence models, heating rates, etc., were tested. Brief discussions on the results of intermediate calculations are presented. All the best settings of intermediate calculations were chosen according to the results and used for the final calculations. Finally, detailed analyses of the results of the final calculations are presented and discussed in detail in the last sections.

4.1. Numerical investigation of the KAERI experiment

The calculation journal was created and the conditions of each calculation were planned (APPENDIX A) before the numerical investigation of the KAERI experiment started. This calculation journal was updated during the overall numerical investigation. Calculations were planned and performed in this order according to the calculation journal:

1. 01 to perform the reference calculation;
2. 02–03 to test the viscous models;
3. 04 to test smaller time step size;
4. 05–07 to perform the mesh independence study;
5. 08–12 to test different conditions of the heating ratio and to perform the final calculation.

Results of the monitoring points that represent the thermocouples TF-01…TF-05, of each calculation, were compared in the charts. The comparison of the turbulence models, mesh size, time step size, and different conditions of the heating ratio were analysed for the first part (until 5300 sec.) of the experiment due to large CPU time requirements for one calculation. Meanwhile, as the boiling process was not simulated the final calculation was performed for time period 0–10558 seconds. Brief discussions are presented in Sections 4.1.1–4.1.3 (intermediate calculations) and detailed discussion in Section 4.1.4 (the final calculation).

4.1.1. Influence of the turbulence models

The first step in the numerical investigation was to analyse the influence of the $k - e$ realizable with enhanced wall treatment and $k - \omega$ SST turbulence models as the most advanced RANS group models to address heat transfer and turbulence problems (67). The Laminar viscous model was tested as well.

The comparison of the results of the 01–03 calculations showed that the TF-01…TF-03 temperatures are in quite good agreement with the experimental data, meanwhile, the TF-04 and TF-05 temperatures show differences (Fig. 4.1–Fig. 4.5). According to the results, the $k - e$ realizable turbulence model works better than $k - \omega$ SST at the thermal stratification region (below the heater rod). The TF-04 and TF-05 temperatures increase immediately during the calculation, meanwhile, during the

experiment, these temperatures show delay. The $k - e$ realizable turbulence model was chosen for further calculations.

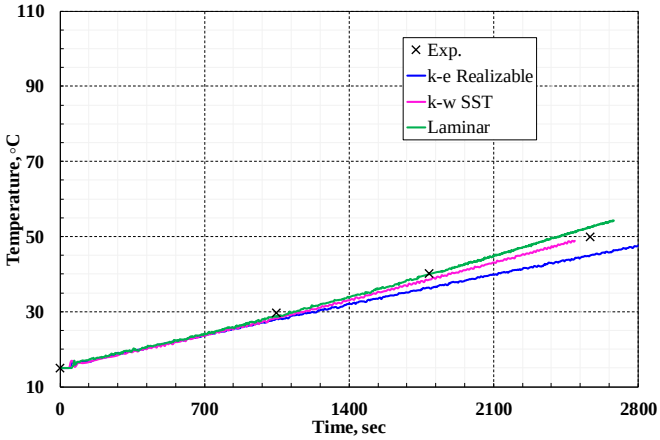

Fig. 4.1. Comparison of measured and calculated TF-01 temperatures

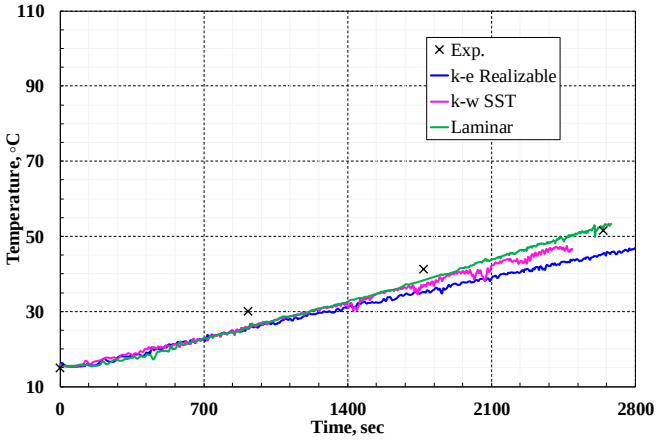

Fig. 4.2. Comparison of measured and calculated TF-02 temperatures

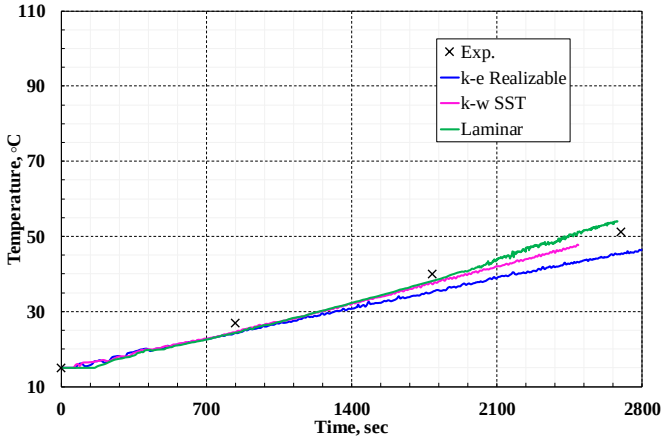

Fig. 4.3. Comparison of measured and calculated TF-03 temperatures

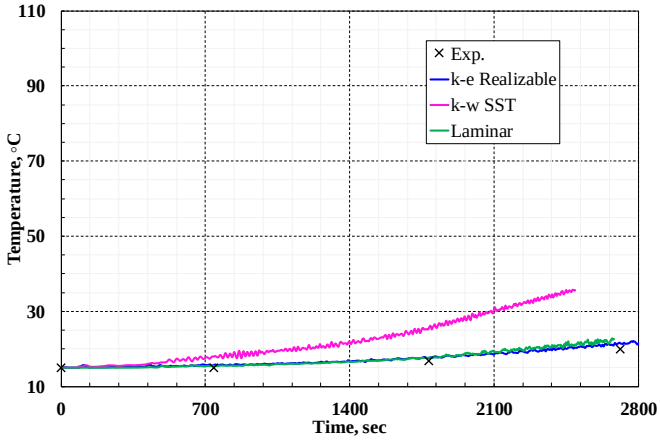

Fig. 4.4. Comparison of measured and calculated TF-04 temperatures

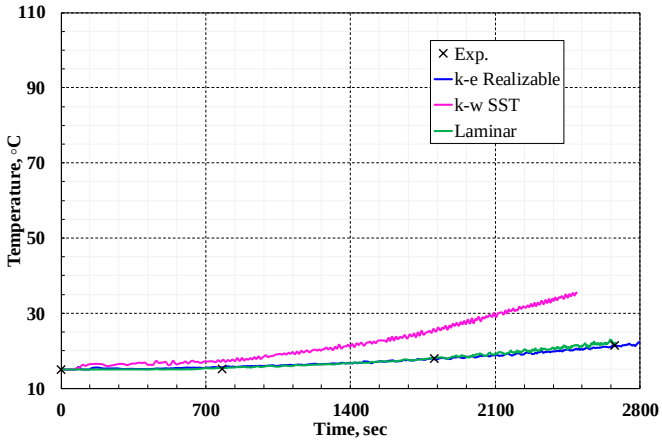

Fig. 4.5. Comparison of measured and calculated TF-05 temperatures

4.1.2. Mesh independence study

In order to investigate the influence of mesh size for results (01, 05–07 calculations), four different meshes were created (Section 3.3.1). The TF-02 monitoring point is only two millimeters away from the heater rod surface, therefore, this monitoring point shows the best results of the influence of mesh size. During the comparison, other monitoring points TF-01, TF-03…TF-05 show similar results.

The mesh, which consists of 313964 hexahedral cells was chosen for further simulations because the temperature value of the monitoring point TF-02 was the same magnitude for the rest 570610 and 922736 meshes (Fig. 4.6). The mesh quality parameters of the mesh, which consist of 313964 hexahedral cells are presented in Table 2.

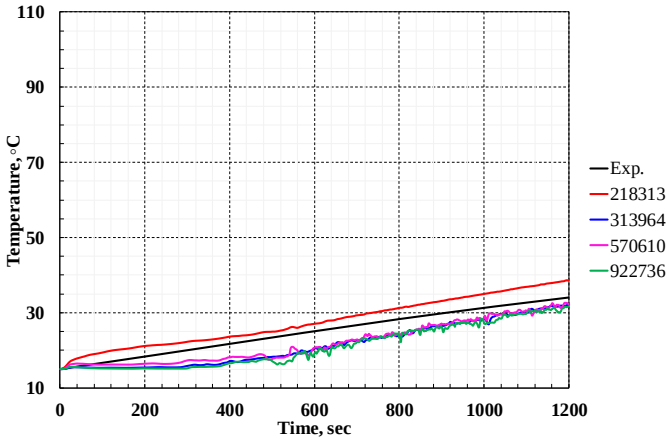

Fig. 4.6. Comparison of measured and calculated TF-02 temperatures

4.1.3. Influence of the heating rate

During the turbulence models testing (Section 4.1.1) and mesh independence study (Section 4.1.2), quite good agreement between the experimental and calculated temperatures of the TF-01…TF-03 was found. Meanwhile, differences between TF-04 and TF-05 temperatures were observed. The results showed that the calculated temperatures increase much faster than the experimental temperatures. The main hypothesis was that the heat flux (600 W) released by the heater rod is too large. In order to confirm this hypothesis and to find a reason why these differences arise, additional calculations (08–12 calculations) related to different heating boundary conditions were performed.

During the 08 calculation, following the assumption that the experimental facility is placed on a very thermal conductive surface such as stainless steel, the bottom wall was cooled using the heat flux thermal condition (-252 W). Slow heating 600 W per 300 seconds was set during the 09 calculation in order to investigate the influence of heating ratio. In all calculations were assumed, that heat flux is released through the all surface of the heater rod, except the 10 calculation, where 480 W / 60 sec were released through the upper surface and 120 W / 60 sec through the lower

surface of the heater rod. The 11 and 12 calculations were performed to investigate the smaller heat flux (480 W / 60 sec and 450 W / 60 sec). The results of these calculations are shown in Fig. 4.7 and Fig. 4.8. The different heating boundary conditions give similar results for the TF-04 and TF-05 temperatures as well as the mesh independence study, the different turbulence models, and smaller time step size. The TF-04 and TF-05 calculated temperatures increase much faster than experimental temperatures.

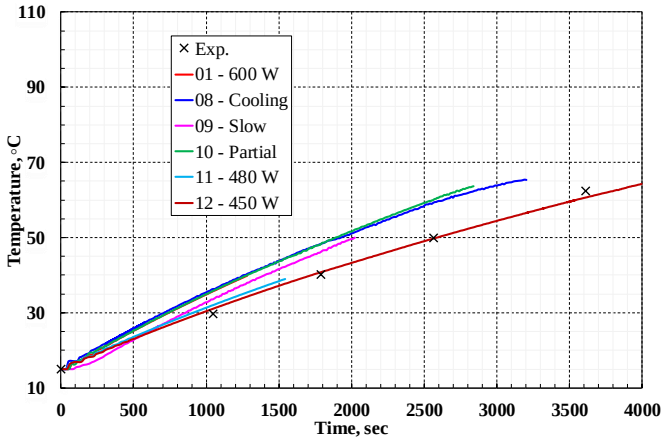

Fig. 4.7. Comparison of measured and calculated TF-01 temperatures

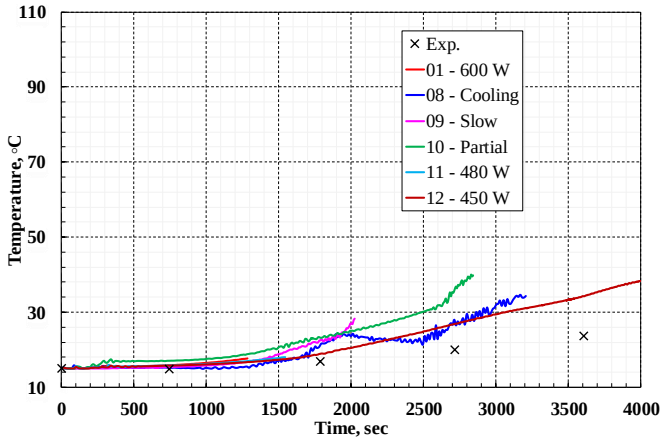

Fig. 4.8. Comparison of measured and calculated TF-04 temperatures

According to the results of 01–12 calculations, the 05 calculation was selected as the final calculation and the two-phase natural convection and thermal stratification phenomena were analysed in more detail in Section 4.1.4.

4.1.4. Final calculation

As it was mentioned earlier, the rectangular enclosure (Fig. 3.2) with the heater rod placed in a horizontal position was modelled using the ANSYS software. The

results of numerical simulations are presented in two vertical cross-sections, as shown in Fig. 4.9. The cross-sections ZX and ZY were chosen according to the positions of TF-01…TF-05 thermocouples in the experimental facility and geometry specifics. In the developed model, the average water temperature is calculated in the positions of TF-01…TF-03 thermocouples.

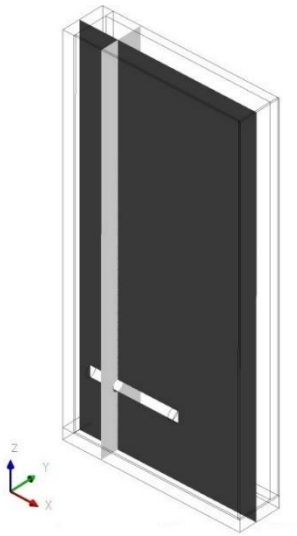

Fig. 4.9. Positions of ZX and ZY planes in the computational domain

During the experiment, 600 W of thermal power was supplied to the heater rod. Due to the heat transferred from the heater rod, the water heats up around the heater. This leads to the local water density decrease. As a result of this density difference, thermally induced buoyancy forces initiate natural convection of the water. As it is seen from Fig. 4.10, the water upward flow arises near the left wall. In the top part of water, just below water level (near a free surface), the water flows in a horizontal direction to the right wall and after mixing with colder water, it starts to flow downward along the right wall. The water circulation is formed above the heater rod, meanwhile, there is no flow below the heater rod and thermal stratification occurs in the lower part of the rectangular enclosure. Fig. 4.10 shows a velocity field at water temperature 72 ℃. The experimentally measured water circulation above the heater rod and the results of numerical simulations are very similar at water temperature (72 ℃). Meanwhile, smaller velocity is observed near the right wall and region near the “non-heated” part of the heater rod. Due to the warming of the water, heat transfer through the free surface is increasing, therefore, natural convection of the air begins above the water. As it is visible in Fig. 4.10, the air above the water region, moves downward near the right wall and moves against water flow direction near the free surface. The heated air rises upward to the top and flows out from the computational domain near the left wall. Similar results are captured in Fig. 4.11 at water temperature equal to 91.3 ℃. Fig. 4.12 and Fig. 4.13 show that thermal stratification disappears and when the water temperature reaches a saturation temperature (water temperatures in the bottom part are equal to 98.1℃) the water becomes well mixed. This shows that

the overall phenomena were predicted by the CFD software in quite good agreement with experimental data. As we can see from Fig. 4.10–Fig. 4.13, there is a sufficiently good agreement between the experimental and numerical velocity fields of the water. The temperature gradients during numerical simulations are presented in Fig. 4.14. Up to 91.3 ℃, in the region below the heater rod, the heat to the water is transferred only due to conduction. As experimental data was not given in References (8, 51), there is no opportunity to show the temperature fields of the experiment. Special measurement technique, for example, Laser-Induced Fluorescence (LIF) measurement technique and fluorescent dyes, must be used during the experiment in order to obtain temperature fields in water.

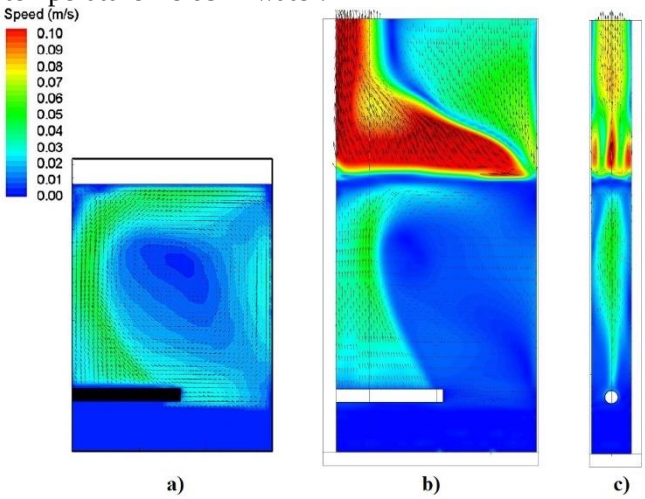

Fig. 4.10. Velocity field at water temperature 72 ℃: a) experiment (51); b) CFD (ZX plane); c) CFD (ZY plane)

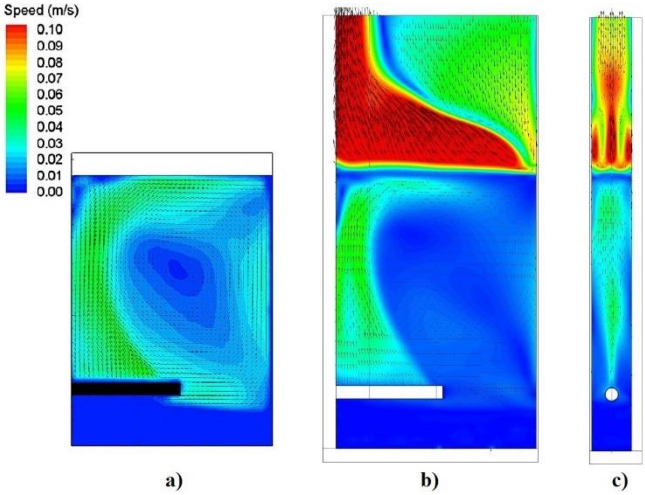

Fig. 4.11. Velocity field at water temperature 91.3 ℃: a) experiment (51); b) CFD (ZX plane); c) CFD (ZY plane)

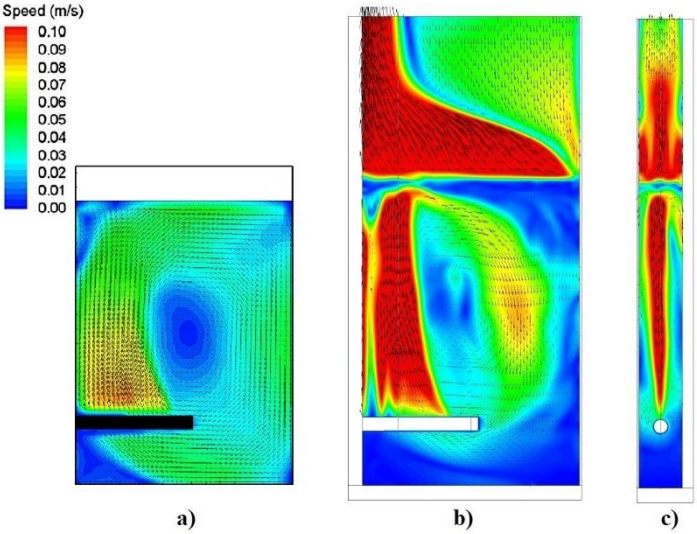

Fig. 4.12. Velocity field at water temperature 98.1 ℃: a) experiment (51); b) CFD (ZX plane); c) CFD (ZY plane)

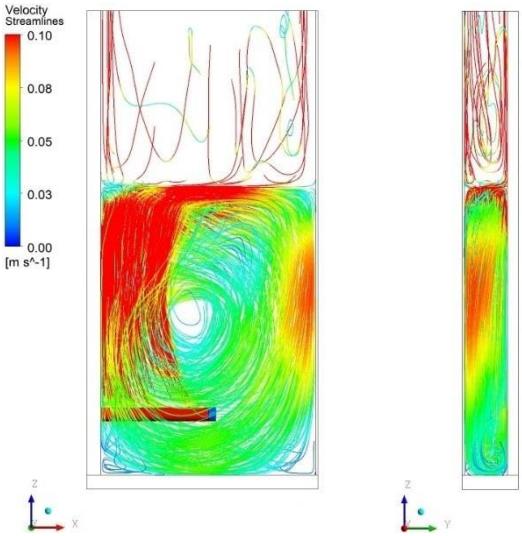

Fig. 4.13. Velocity streamlines at water temperature 98.1 ℃

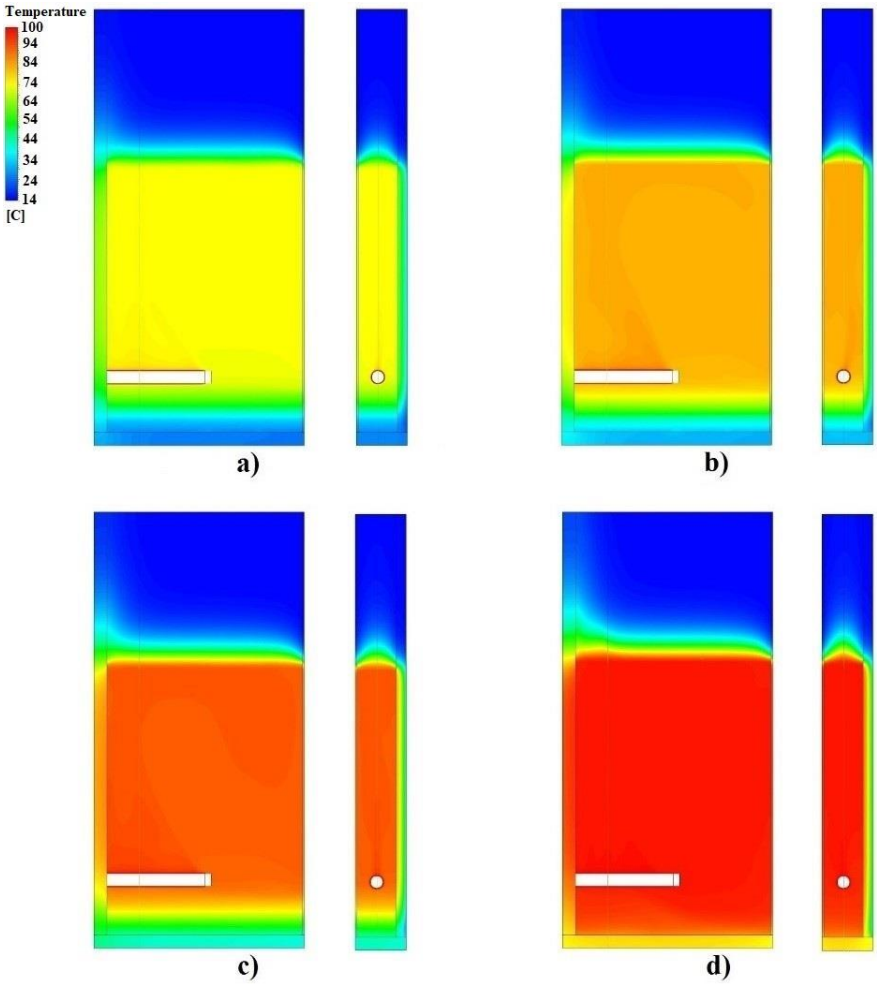

Fig. 4.14. Temperature fields, calculated by CFD, at different water temperatures: a) 72 ℃; b) 81.5 ℃; c) 91.3 ℃; d) 98.1 ℃

The comparison of TF-01…TF-03 temperature changes (Fig. 4.15–Fig. 4.17) shows a good agreement with the experimental data. The thermocouples TF-01…TF-03 present the behaviour of water temperature in the part of the experimental facility above the heater rod. This part consists of ~80 % of the total water volume in the experimental facility. The agreement between the measured and calculated TF-01…TF-03 water temperatures proves that heat losses (heat transfer coefficient from the outside surface area of walls to the ambient air) are predicted well.

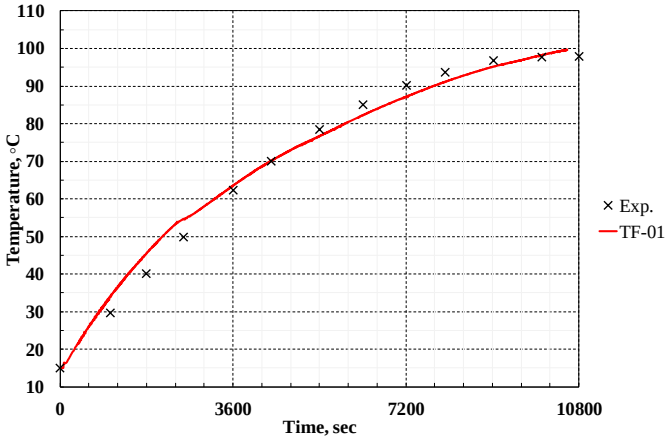

Fig. 4.15. Comparison of measured and calculated TF-01 water temperature

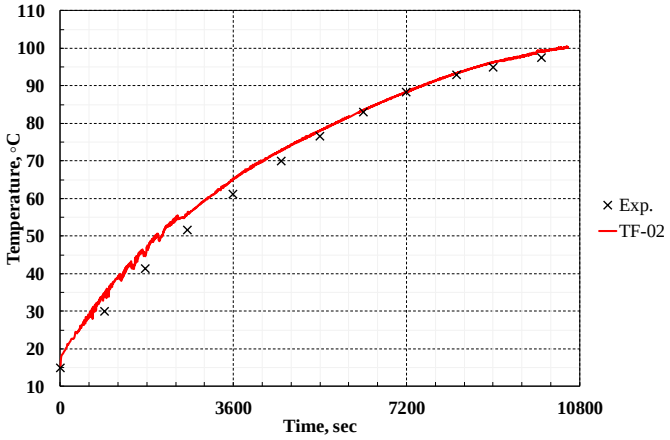

Fig. 4.16. Comparison of measured and calculated TF-02 water temperature

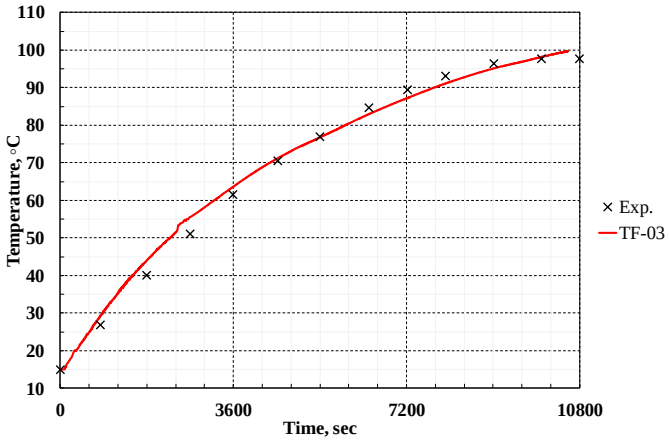

Fig. 4.17. Comparison of measured and calculated TF-03 water temperature

During the experiment measured temperatures of TF-04…TF-05 shows a significant delay in water heat-up, while in numerical simulations, the TF-04…TF-05 temperatures start to increase with a very short delay after the beginning of heat-up (Fig. 4.18, Fig. 4.19). The first observation is that the differences between the experimental and numerical behaviour of TF-04…TF-05 temperatures could arise due to the unknown accurate heat losses during the experiment. In Reference (51), when the water temperature was increased from 20 ℃ to 90 ℃, it was just written that the average heat loss during the experiment was approximately 310 W. A detailed investigation of heat losses during the experiment was not performed. Numerical simulations showed greater heat losses – from 80 W (at the beginning of heating) up to 531 W (at the beginning of water boiling). Based on the good agreement of calculated and measured water TF-01…TF-03 temperatures, we can conclude that we set a correct heat transfer coefficient and numerical heat losses are very similar to the experimental heat losses. The second observation is that the heat losses are very large compared to the thermal power of the heater rod and the walls of the rectangular enclosure must play a significant role as heat sinks. The front and right walls are made from Pyrex-glass, which is a very conductive material with low specific heat, also, the thickness of the front and right walls is only three millimeters, therefore, these walls are not significant heat sinks. Meanwhile, the bottom, left, and back walls have larger thickness (from 15 to 20 mm) and are made from polycarbonate and stainless steel. According to Table 3, these walls can be treated as significant heat sinks. Taking into account this observation and the results of the ANSYS Fluent, we can conclude that the main amount of heat losses goes to the environment through the front and right walls, while the rest small amount of heat losses goes through the bottom, left, and back walls. In addition, there is no information in Reference (51) regarding the accurate thermal-physical properties of the walls, which were used in the construction process of the experimental facility, therefore, deviations of the TF-04 and TF-05 numerical results are expected. The third observation is that the processes during the experiment are very slow, therefore, unknown accurate heat losses during the experiment and unknown accurate thermal-physical properties of the walls must have a significant influence on the TF-04 and TF-05 numerical results. Despite all observations, in order to understand TF-04 and TF-05 differences, was tested a lot of different assumptions: no heat losses, different heat transfer coefficients, cooling of the bottom wall, different mesh size, different turbulence models, different heat-up rate, etc., and all these tests gave very similar results. The assumption that the measurements of TF-04 and TF-05 temperatures could be affected by some systematic error could not be rejected either.

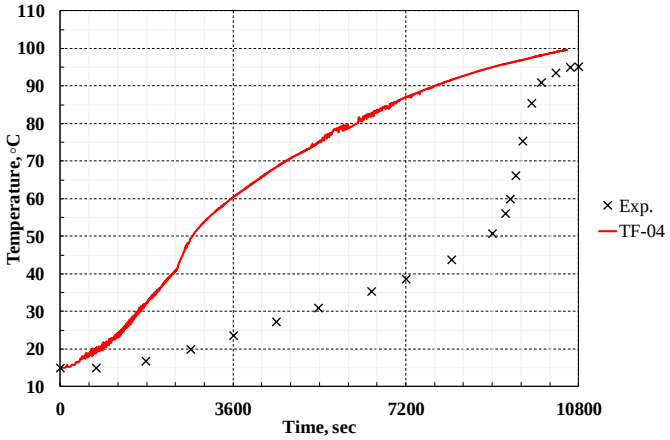

Fig. 4.18. Comparison of measured and calculated TF-04 water temperature

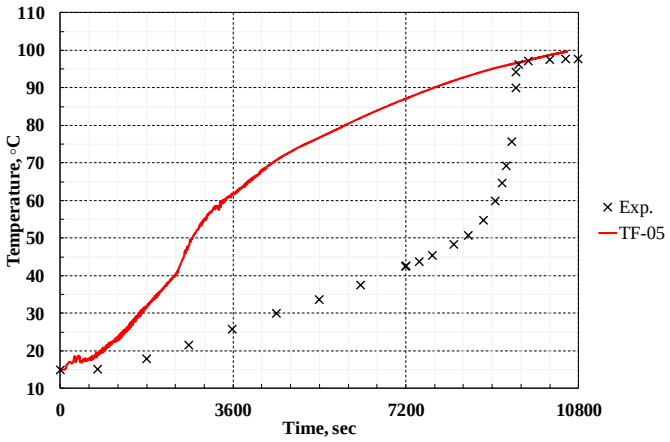

Fig. 4.19. Comparison of measured and calculated TF-05 water temperature

Heat losses through the walls of the computational domain until the water temperature reaches the saturation temperature are presented in Fig. 4.20. The minus sign means the movement of the heat flux from the computational domain to the ambient.

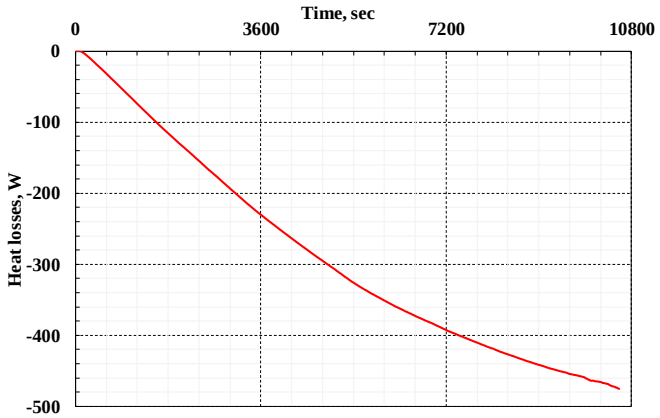

Fig. 4.20. Total heat losses through the walls of the computational domain

Fig. 4.21 and Fig. 4.22 show water mass and volume changes during the final calculation. During the time period of 0–3600 seconds, water mass is stable and water volume increases due to the density changes. When the evaporation phenomenon is becoming more and more intense, water mass starts to decrease significantly since 4200 seconds until the end of the final calculation. The biggest water volume is about 7000 seconds and starts to decrease due to the evaporation phenomenon. These charts demonstrate that not only the natural convection and thermal stratification phenomenon were simulated but also the generation of water-vapor bubbles around the heater rod and evaporation phenomena were considered in the numerical investigation.

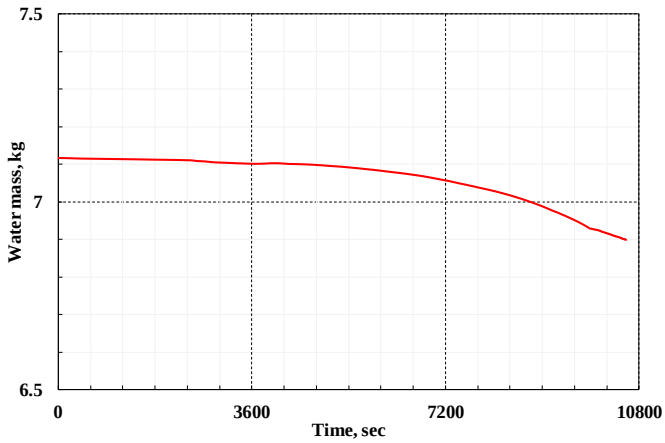

Fig. 4.21. Water mass conservation in the computational domain

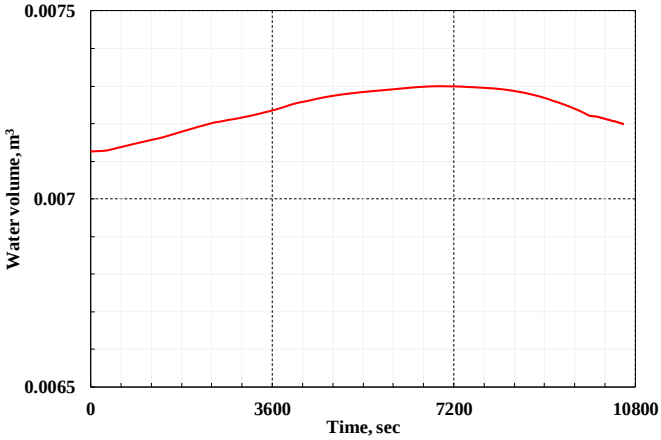

Fig. 4.22. Water volume conservation in the computational domain

The numerical investigation demonstrates similar results of two-phase natural convection above the heater rod and thermal stratification below the heater rod as in the experimental facility. Furthermore, it was found a good agreement with the experimental data, except for the deviation of TF-04 and TF-05 temperatures. In order to perform the double check of the created methodology and demonstrate that the created methodology is reliable for numerical investigations of the two-phase natural convection and thermal stratification phenomena, the additional experiment (Section 3.2) was chosen and investigated using the same CFD software and the same methodology.

4.2. Numerical investigation of the Osaka University experiment

The calculation journal (APPENDIX B) was created as well as for investigations of the KAERI experiment. The 26 calculations were planed and performed in this order:

1. 01 to perform the reference calculation;
2. 02 to test fewer iterations per time step;
3. 03–04 to test smaller time step size;
4. 05–11 to find the proper heat transfer coefficient;
5. 12–14 to investigate the influence of the heating ratio;
6. 15–19 to find the heating power;
7. 20–21 to test the turbulence models;
8. 22–14 to perform the mesh independence study;
9. 26 to supplement the CFD model with solid walls and to perform the final calculation.

The monitoring points, which represent the thermocouples in the centre sub-channel, the peripheral sub-channel, and the pipe were created to compare numerical and experimental results. As opposed to the KAERI experiment, almost all calculations were performed and compared for the full-time period of the experiment (0–1357 sec). In order to have a balance between the quality of results and CPU speed, all calculations before the mesh independence study and the final calculation were

performed using the medium quality mesh (463176). As well as a discussion of the KAERI results, brief discussions are presented for Sections 4.2.1–4.2.7 (intermediate calculations) and a detailed discussion for the final calculation (Section 4.2.8). The result of each monitoring point was compared to the experimental data in the charts. However, due to a large amount of the charts, the results of the “CS 135”, “CS 75”, “CS -5” and “120” locations are presented only for a brief discussion of the intermediate calculations. Meanwhile much more results presented for a detailed discussion of the final calculation. The locations “CS 135”, “CS 75”, “CS -5” and “120” are in four different regions of the experimental facility. These locations are presented in Fig. 4.23.

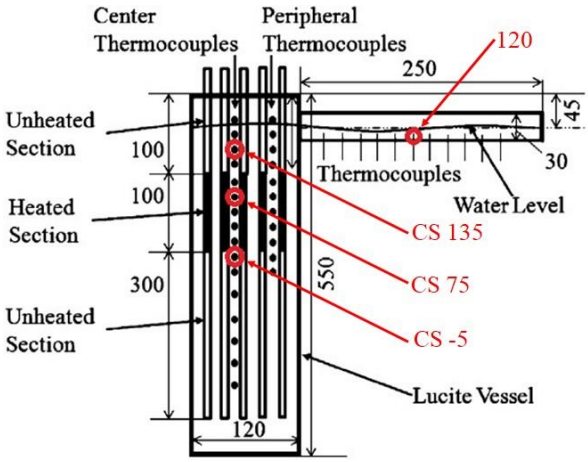

Fig. 4.23. Locations of the “CS 135”, “CS 75”, “CS -5” and “120” thermocouples and monitoring points

4.2.1. Influence of the number of iterations

To analyse the influence of the results using four and 50 iterations, the number of iterations per time step was investigated. As to test different boundary conditions (01–24 calculations) using 50 iterations per time step will require a few years of the CPU time, four iterations were chosen to perform calculations with small-time consumptions. Therefore, 50 iterations per time step were chosen only for the initial and final calculations. Using 50 iterations per time step and depending on the CFL number, convergence criteria were satisfied after 6–15 iterations. It demonstrates, that a converged solution was reached in each time step.

As heat losses during the experiment are unknown, the 01–02 calculations were performed without the heat transfer coefficient (no heat losses). Therefore, Fig. 4.24-Fig. 4.27 shows that the calculated temperatures are higher than the experimental temperatures and the differences between calculations using four and 50 iterations per time step are negligible, except the pipe region where minor differences were captured.

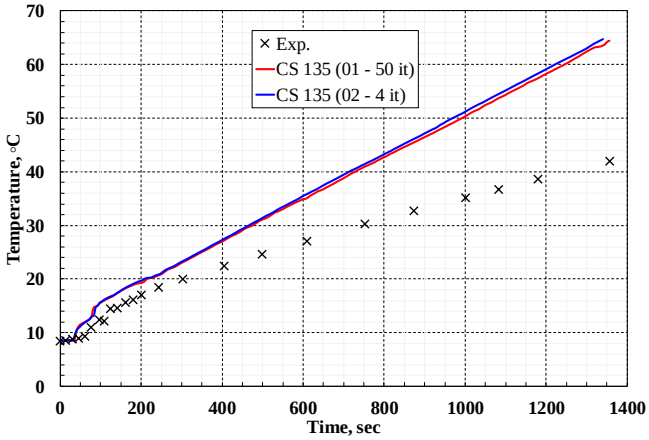

Fig. 4.24. Comparison of measured and calculated CS 135 temperature

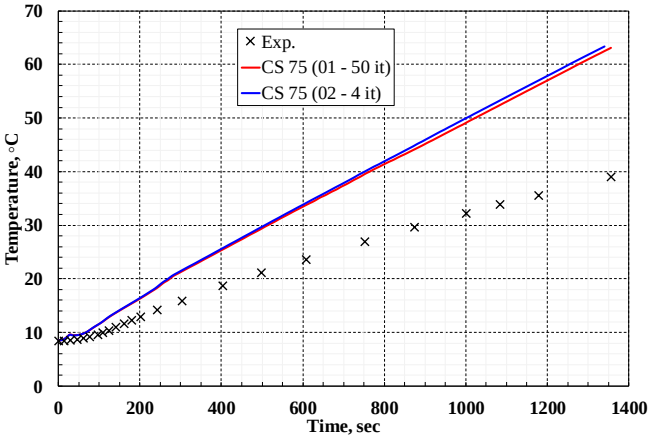

Fig. 4.25. Comparison of measured and calculated CS 75 temperature

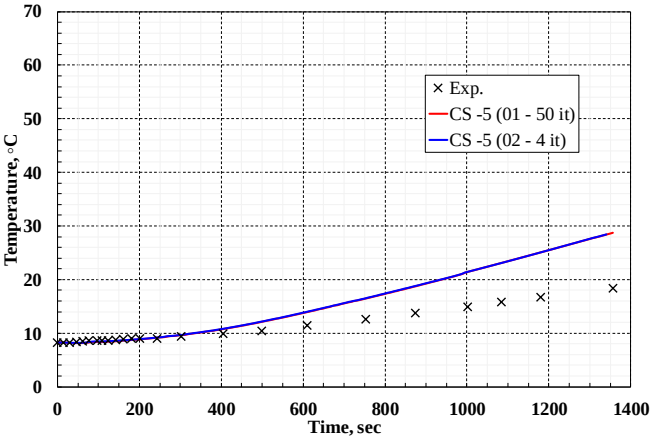

Fig. 4.26. Comparison of measured and calculated CS -5 temperature

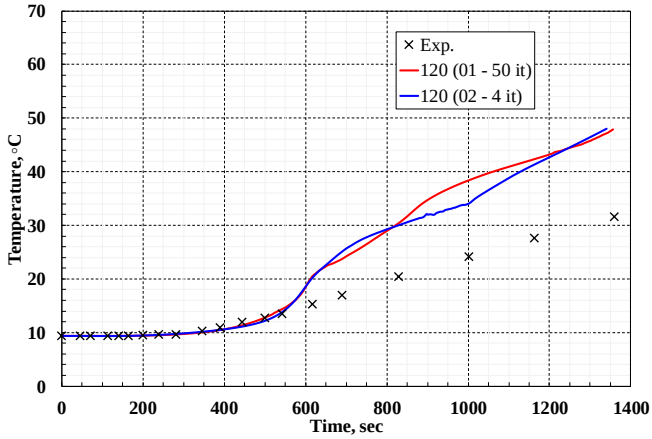

Fig. 4.27. Comparison of measured and calculated 120 temperature

4.2.2. Influence of time step size

The influence of the different time step sizes was investigated. The initial calculation was performed using 0.015 second for each time step. The 0.01 second was used for the 03 calculation and 0.005 second for the 04 calculation. All different sizes of time step demonstrate a stable solution and residuals were always decreasing. CPU time consumptions using 0.015 second for time step was approximately two days, therefore, it was decided to continue the calculation until the end. Meanwhile, due to a large CPU time consumption, the 03 calculation was stopped at 1150 second and the 04 calculation at 625 second.

Fig. 4.28–Fig. 4.31 show that the chosen time step sizes has no influence for the results, except in the pipe region where minor differences were captured.

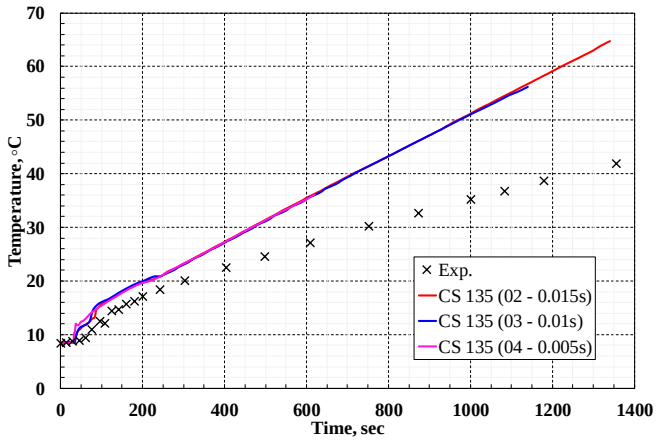

Fig. 4.28. Comparison of measured and calculated CS 135 temperature

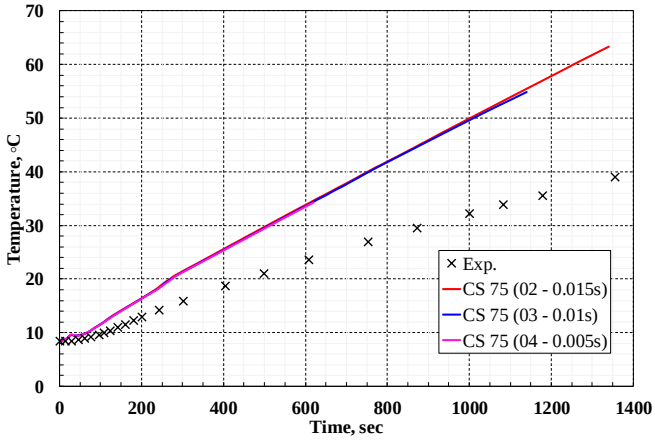

Fig. 4.29. Comparison of measured and calculated CS 75 temperature

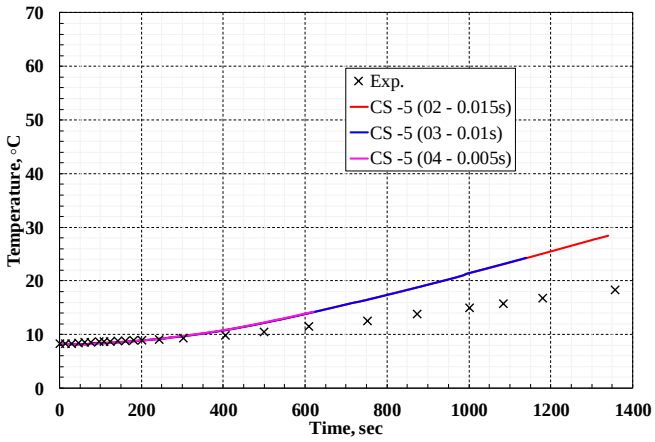

Fig. 4.30. Comparison of measured and calculated CS -5 temperature

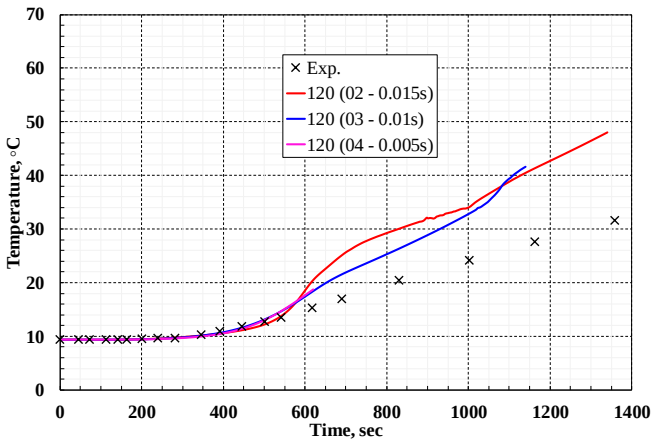

Fig. 4.31. Comparison of measured and calculated 120 temperature

4.2.3. Influence of the heat transfer coefficient

After previous investigations, the following aim was to find a proper heat transfer coefficient and heat losses. The heat transfer coefficient and heat losses were not investigated during the experiment and not specified in the Reference (52), therefore, they are unknown. According to Reference (77), experimentally and numerically it was found that the heat transfer coefficient on a vertical flat plate in air is between 5 and 10 W/m^2·K. In order to find proper heat transfer coefficient and heat losses, and to perform sensitivity study, the different heat transfer coefficients were tested: 5, 30, 50, 70 and 100 W/m^2·K (05–11 calculations). Fig. 4.32–Fig. 4.35 show the temperatures changes depending on the heat transfer coefficient. Notwithstanding that the trend of the 50 W/m^2·K curve (09 calculation) represents the trend of the experimental points the best, during the experiment the heating power seems too high compared to the calculations. Fig. 4.35 shows that the pipe region is very sensitive to the size of the heat transfer coefficient. The size of the heat transfer coefficient has no influence on results when the fluid and environment air temperatures are similar at the beginning of the calculations. Meanwhile, the size of the heat transfer coefficient has a major influence on the temperatures due to large temperature differences at the end of the calculations.

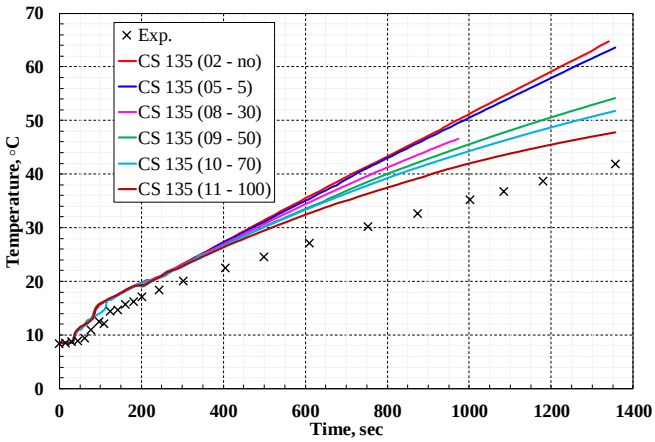

Fig. 4.32. Comparison of measured and calculated CS 135 temperature

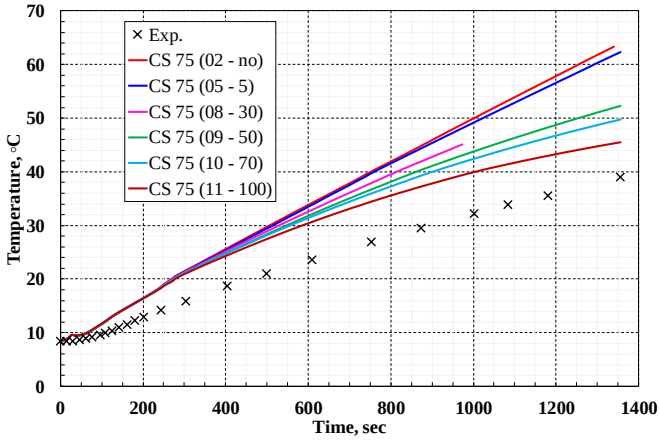

Fig. 4.33. Comparison of measured and calculated CS 75 temperature

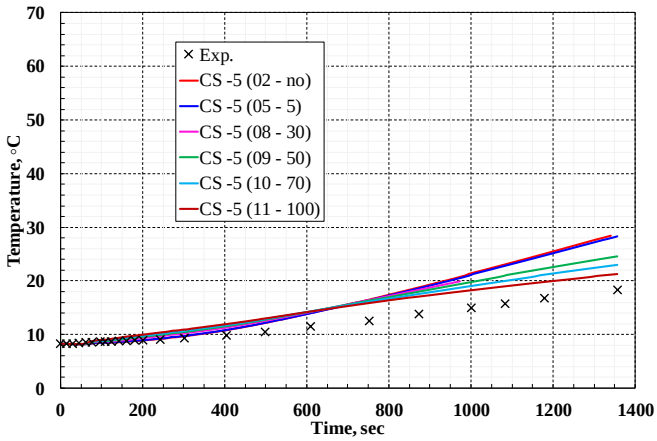

Fig. 4.34. Comparison of measured and calculated CS -5 temperature

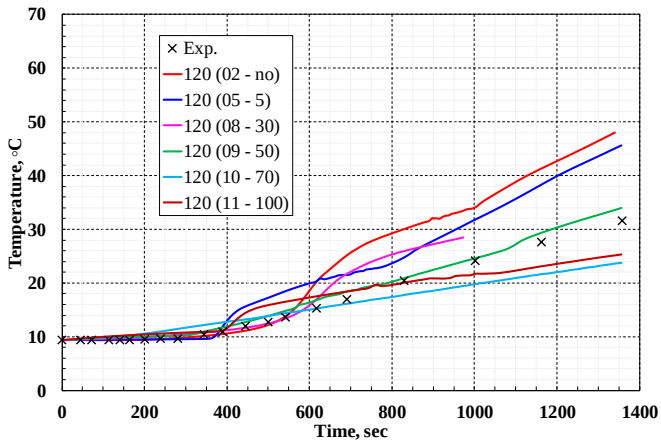

Fig. 4.35. Comparison of measured and calculated 120 temperature

At all sizes of the heat transfer coefficient, the calculated temperatures are too high compared to the experimental results. After 400 seconds, the temperatures begin to vary and the biggest differences are captured at the end of the calculations. The trend of the 100 W/m^2·K curve shows that the calculated heat losses will be larger than the experimental heat losses, provided that the duration of the experiment and calculation will be longer than 1357 seconds. All these observations cause the hypothesis that the heating power (4400 W/m^2) specified by the authors of the experiment can be too large compared to the real heating power during the experiment. In order to verify this hypothesis, heat balances of the different experiment cases (4400, 8800, 17800, and 35500 W/m^2) were calculated according to the heat balance equation. A systematic error was found after the calculation of heat balances for the different experimental cases. A comparison of the heating power specified by the authors of the experiment and calculated according to the heat balance equation are presented in Table 8. Deviations between the specified and calculated heat fluxes for all experiment cases vary from ~56 % until ~62 %. Therefore, it was decided to verify this hypothesis and additional 12–19 calculations were performed.

Table 8. Comparison of specified and calculated heat fluxes

Case No	Heat flux, W/m^2		Heat flux, W		Difference, %
	Experiment	Experiment	Calculated	Calculated	~56
1	4400	~2470	345	~194	~57
2	8800	~5042	691	~396	~65
3	17800	~11319	1398	~889	~63
4	35500	~22014	2788	~1729	~62

4.2.4. Influence of the heating rate

In order to verify the hypothesis, four different heating rates were investigated. The first calculation (09 calculation) indicates an assumption that the heat flux is released immediately when the calculation starts (344.53 W / 0 sec). For the rest calculations these heating rates were chosen: 344.53 W / 30 sec, 344.53 W / 60 sec and 344.53 W / 120 sec.

Fig. 4.36-Fig. 4.39 show the influence of the heating rates. There are significant temperature differences in the heated and upper unheated regions at the beginning of the calculations, meanwhile, there are no significant temperature differences at the end of the calculations. Heating rates have no influence on the thermal stratification region. Results show that the heating rate is not the reason why the calculated temperatures are higher than the experimental temperatures.

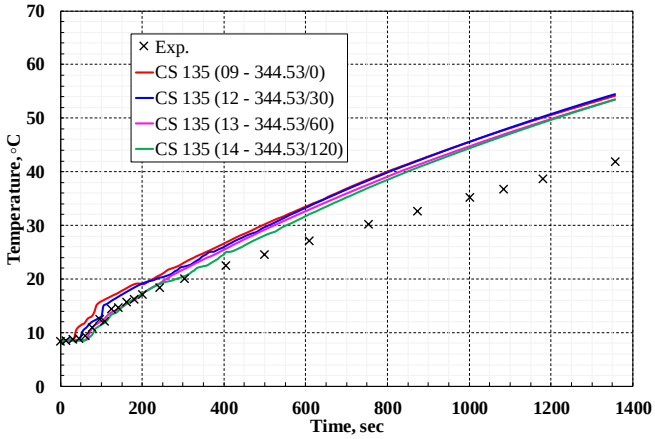

Fig. 4.36. Comparison of measured and calculated CS 135 temperature

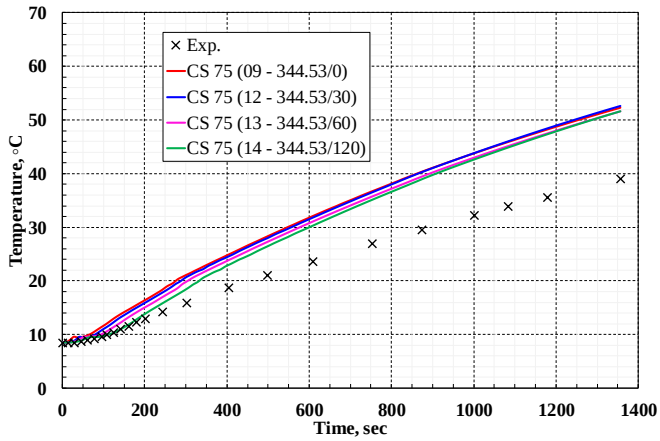

Fig. 4.37. Comparison of measured and calculated CS 75 temperature

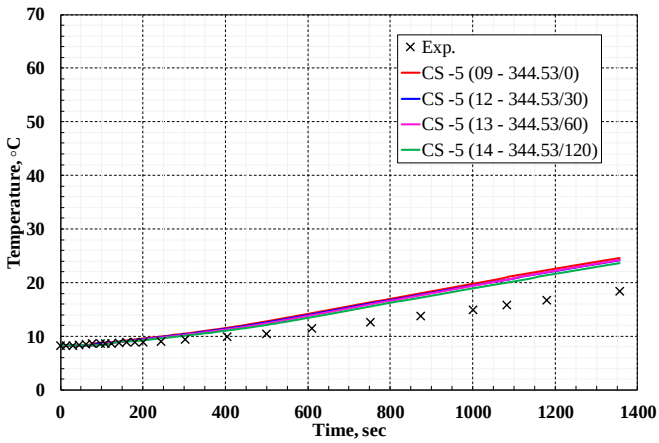

Fig. 4.38. Comparison of measured and calculated CS -5 temperature

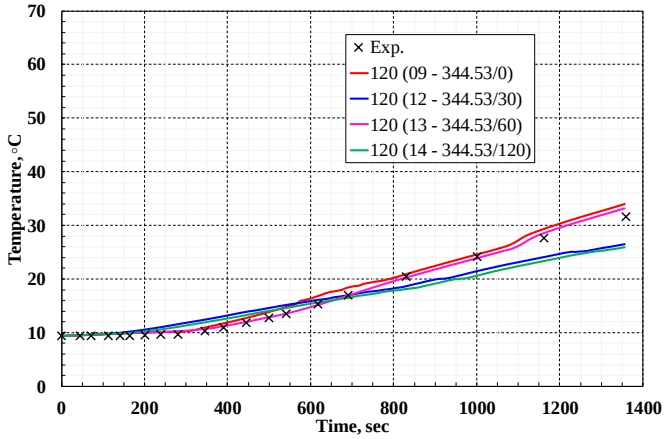

Fig. 4.39. Comparison of measured and calculated 120 temperature

4.2.5. Influence of the heating power

The incorrect heating power might be the reason why the calculated temperatures are higher than the experimental temperatures. Additional calculations (15–19 calculations) of different heating power were performed. It was assumed, that full heating power will be reached after 30 seconds since the calculation starts and the heat transfer coefficient 5 W/m^2·K was applied. Different heat flux sizes were tested: 3500, 2700, 2600, and 2500 W/m^2. The most probable real heat flux is 2500 W/m^2 according to Table 8.

Fig. 4.40–Fig. 4.42 show that the heat flux of 2600 W/m^2 is in a good agreement with the experimental data in the upper unheated, the heated, and the thermal stratification regions. Meanwhile, the calculated temperature is lower than the experimental temperature in the pipe region (Fig. 4.43). These results demonstrate the hypothesis that heating power (4400 W/m^2) specified by the authors of the experiment is too large compared to the real heating power during the experiment. Real heating power should be around 2600 W/m^2.

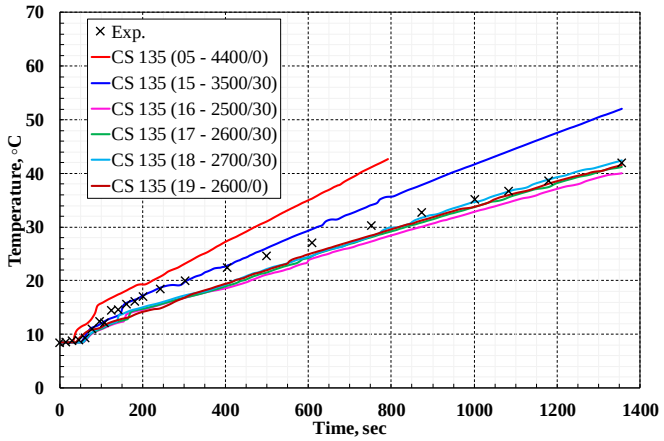

Fig. 4.40. Comparison of measured and calculated CS 135 temperature

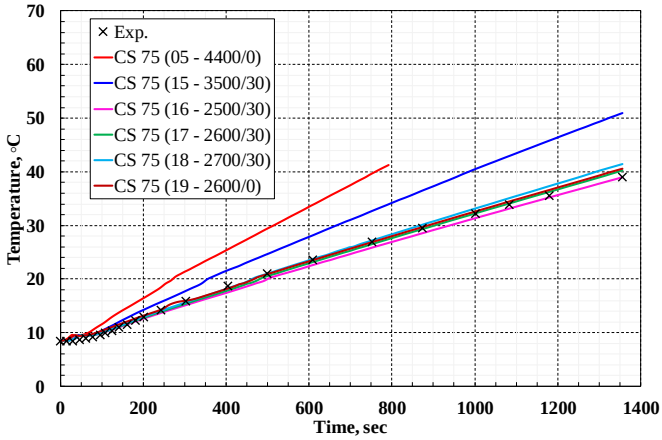

Fig. 4.41. Comparison of measured and calculated CS 75 temperature

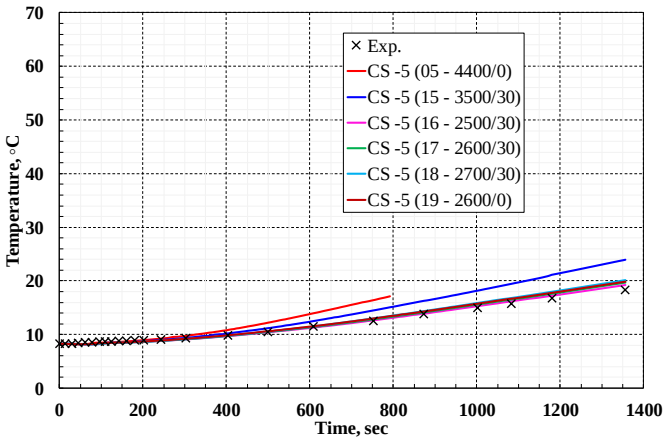

Fig. 4.42. Comparison of measured and calculated CS -5 temperature

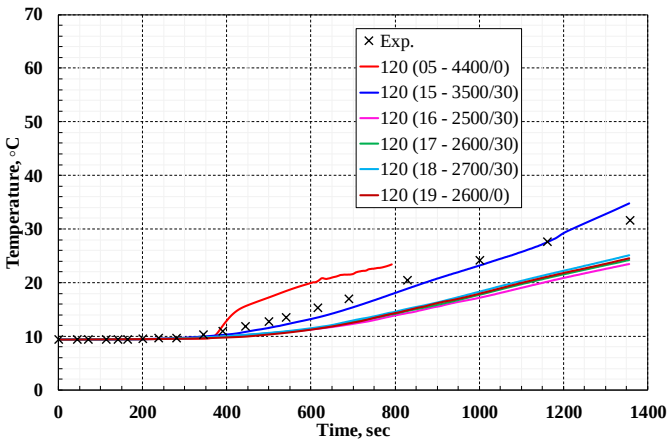

Fig. 4.43. Comparison of measured and calculated 120 temperature

4.2.6. Influence of the turbulence models

Having found the correct heating power, the following step was to analyse the influence of the $k - e$ realizable and standard turbulence models with enhanced wall treatment and the $k - \omega$ SST turbulence model (17, 20–21 calculations).

Fig. 4.44–Fig. 4.46 show small differences in temperatures in the upper unheated region for the time period of 100–550 seconds. Meanwhile, there are no differences in the heated and the thermal stratification regions. Fig. 4.47 shows that the temperature starts to increase dramatically from 550 until 850 seconds using the $k - \omega$ SST turbulence model, and the temperature remains much higher than the temperatures using the $k - e$ realizable and standard turbulence models. The trend of the curves of the $k - e$ realizable and standard turbulence models best represents the trend of the experimental points.

These differences can be explained by the production/dissipation of turbulence by buoyancy. In a non-zero gravity field, buoyancy forces can suppress or promote turbulence in the presence of density gradients. Buoyancy tends to suppress turbulence at a stable stratification and the buoyancy promotes turbulence at an unstable stratification. The $k - e$ realizable turbulence model with enhanced wall treatment was chosen for further calculations.

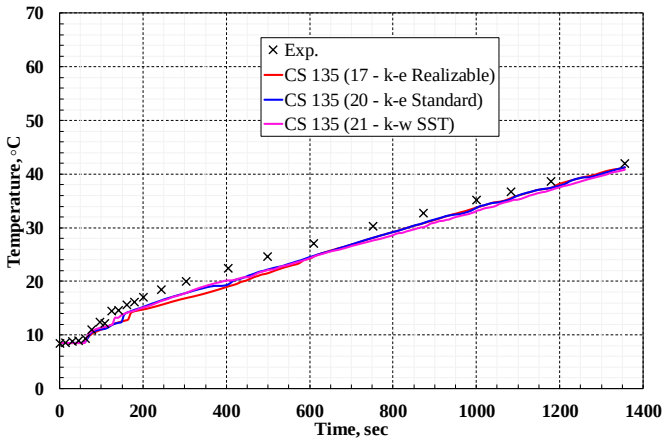

Fig. 4.44. Comparison of measured and calculated CS 135 temperature

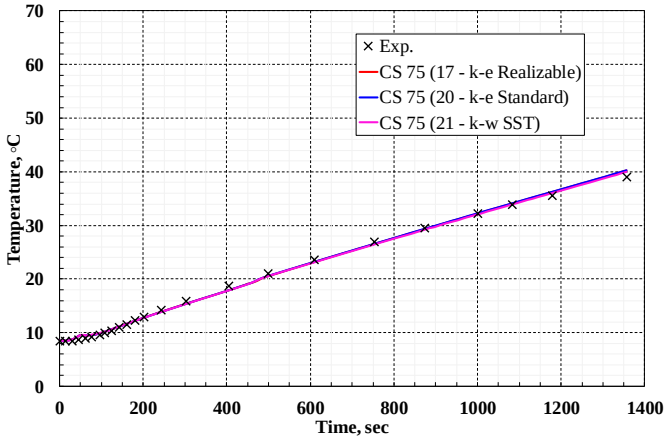

Fig. 4.45. Comparison of measured and calculated CS 75 temperature

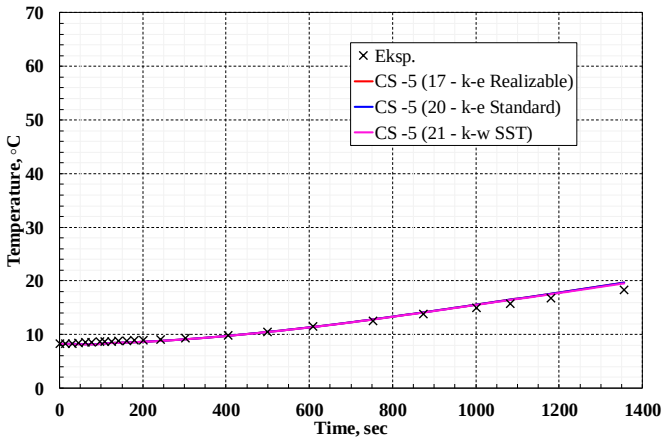

Fig. 4.46. Comparison of measured and calculated CS -5 temperature

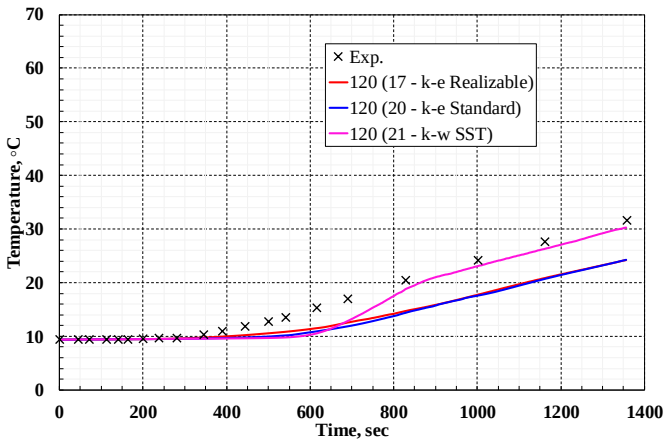

Fig. 4.47. Comparison of measured and calculated 120 temperature

4.2.7. Mesh independence study

The main part of calculations was performed using the mesh, which consists of 463176 hexahedral cells, and each time step size was 0.015 second. This mesh was a reference mesh.

The four different meshes were tested in the mesh independence study. The mesh cells size and time step size were changed by a factor 1.5. The time step size was changed in order to ensure the same CFL number. For example, the time step size is 0.0225 second for the mesh, which consists of 98550 cells (22 calculation). Time step size is 0.0075 second for 1125338 mesh cells (23 calculation), and 0.00375 for 2763037 mesh cells (23 calculation), respectively. The mesh, which consists of 7285416 cells was included in the calculations journal, however, due to large CPU time requirements, it was impossible to perform the calculation using this mesh.

Fig. 4.48–Fig. 4.51 show that the number of mesh cells has no influence on the upper unheated and the heated regions. Small temperatures differences are captured in the thermal stratification region, meanwhile, there are significant temperatures differences in the pipe region.

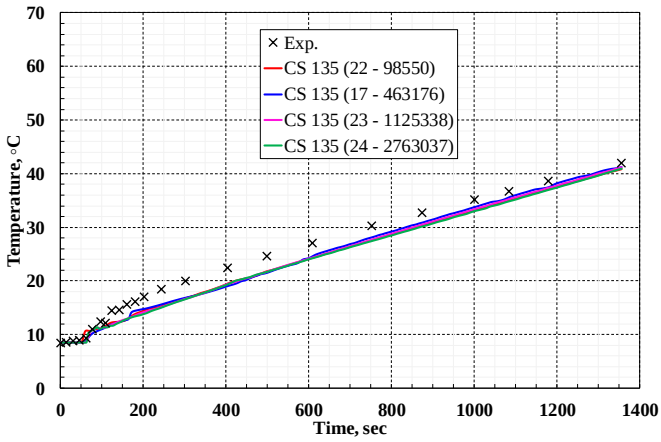

Fig. 4.48. Comparison of measured and calculated CS 135 temperature

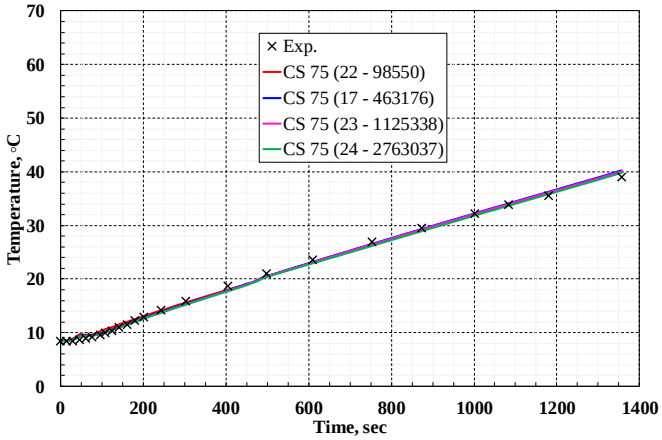

Fig. 4.49. Comparison of measured and calculated CS 75 temperature

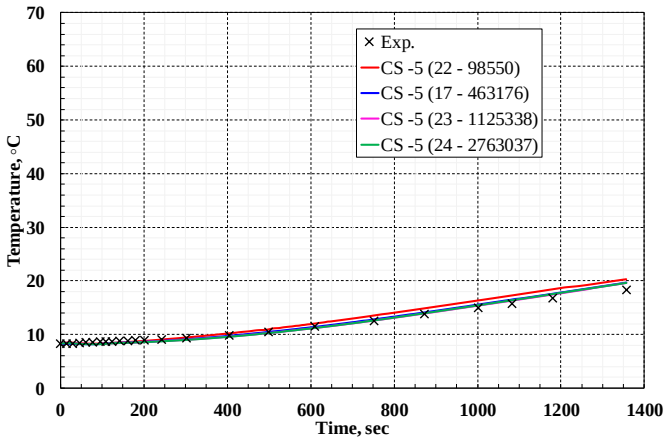

Fig. 4.50. Comparison of measured and calculated CS -5 temperature

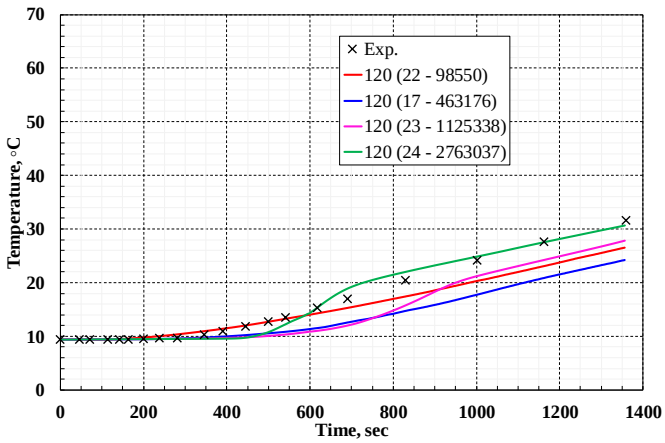

Fig. 4.51. Comparison of measured and calculated 120 temperature

The mesh, which consists of 2763037 hexahedral cells and the time step size 0.00375 second was chosen for the final calculation. The non-dimensional distance from the wall (Y^+) of the 24 calculation was $Y^+<0.5$. It demonstrates that mesh cells located at the near-wall regions are of high quality and are able to capture various gradients. In order to include thermal inertia of the solid structures in the CFD model, the CFD model was supplemented by the solid walls. The mesh of the solid walls consists of 715240 hexahedral cells. The total number of mesh cells is 3478277. The model of solid walls was created according to the symmetry plane. Due to the lack of information regarding the solid walls used in the experimental facility, it was assumed that the thickness of solid walls is 10 millimeters, except the pipe region, where five-millimeters thickness was chosen. The updated mesh is presented in Fig. 3.14. The mesh quality parameters of the mesh used for the final calculation is presented in Table 4. The thermal properties of the solid walls are presented in Table 5.

4.2.8. Final calculation

The results of the final calculation are presented on the symmetry plane, the horizontal cross-section located at 50 mm altitude, and the outer walls, as shown in Fig. 4.52.

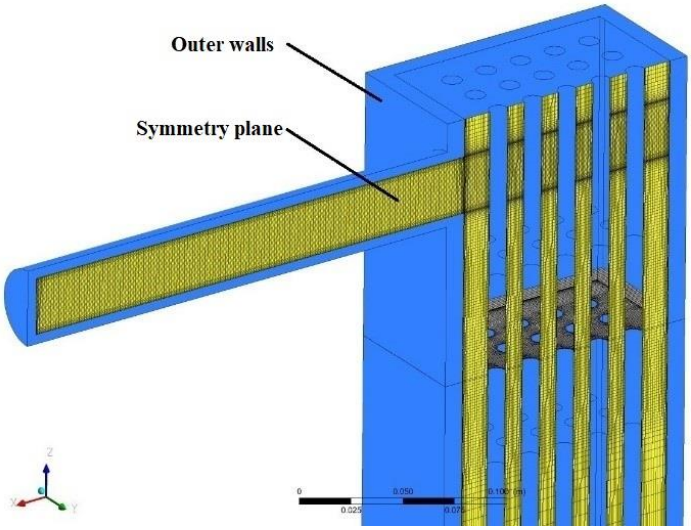

Fig. 4.52. Locations of symmetry plane, outer walls and cross-section

The final calculation includes all the best settings used in the intermediate calculations: 50 iterations per time step, time step size 0.00375 second, fluid region consist of 2763037 hexahedral cells, the solid region consists of 715240 hexahedral cells, the heating power is 2600 W/m^2 (204 W), full heating power reached per 30 seconds, the heat transfer coefficient is 5 W/m^2·K, the $k-e$ realizable turbulence model with enhanced wall treatment.

Fig. 4.53 and Fig. 4.54 shows that the calculated temperatures are a little bit lower in the upper unheated region and the heated regions, compared to the

experimental data. These differences arise due to the solid walls, which were added to the CFD model. Slightly higher heating power than 2600 W/m^2 was needed to compensate for the thermal inertia of the solid walls. The maximum deviation in the upper unheated region is 9 % and in the heated region 5 %, when heating power is 2600 W/m^2. If the thermal inertia will be compensated by additional heating power, the maximum deviations would be smaller.

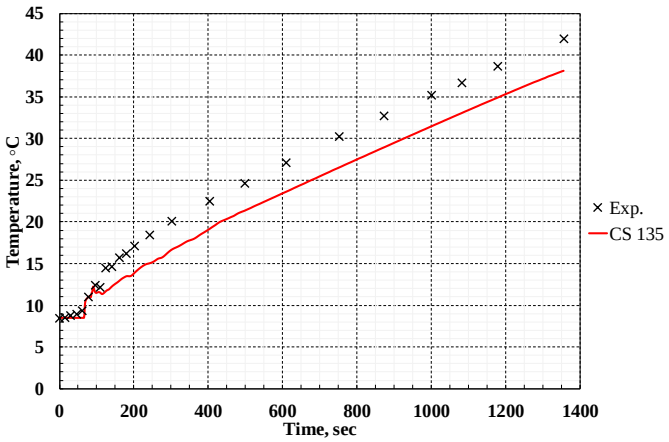

Fig. 4.53. Comparison of measured and calculated CS 135 temperature

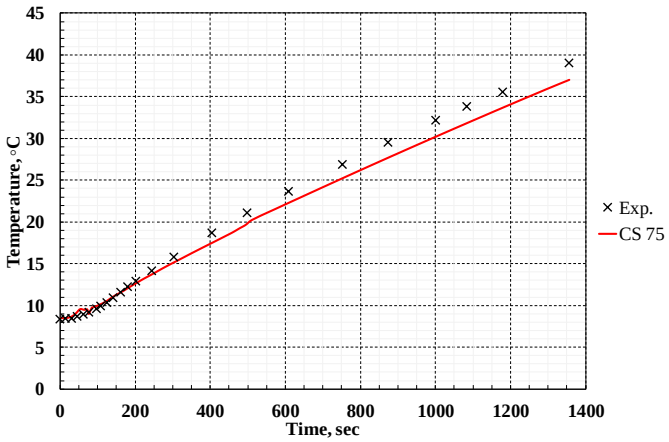

Fig. 4.54. Comparison of measured and calculated CS 75 temperature

Fig. 4.55 shows the temperature variation in the thermal stratification region immediately under the heater rods. The temperature is in very good agreement with the experimental data. The maximum deviation in the thermal stratification region is 2.6 %, which demonstrates that the created methodology can capture the thermal stratification phenomenon. Fig. 4.56 shows quite a good temperature agreement with the experimental data in the pipe region. The maximum deviation in the pipe region is 14 %. As mentioned in the comments of the intermediate calculations, the pipe region is very sensitive in changes in various settings. As well as in the upper unheated

and the heated regions, if the thermal inertia will be compensated by additional heating power, the maximum deviations in the pipe regions would be smaller.

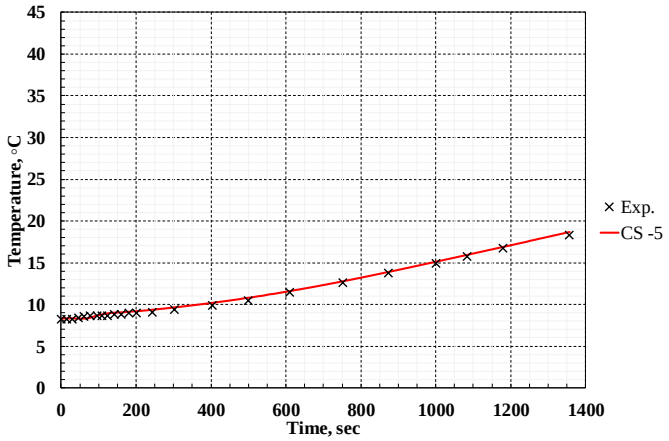

Fig. 4.55. Comparison of measured and calculated CS -5 temperature

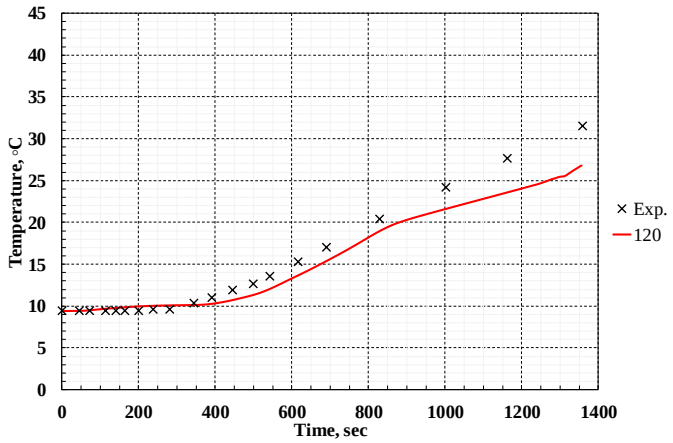

Fig. 4.56. Comparison of measured and calculated 120 temperature

Fig. 4.57 shows the total heat losses during the final calculation. Provided that there is no experimental data on heat losses during the experiment, only calculated heat losses are presented. Initial water temperature is lower (9 ℃) than the initial environment temperature (12 ℃) at the beginning of the final calculation. The heat flux spreads from the environment to the computational domain until 800 seconds due to a larger environment temperature. Due to the heat flux emitted by the heater rods, water temperature increases and heat flux starts to spread in the opposite direction from the computational domain to the environment. Heat losses are very small (only ~4 W) at the end of the final calculation.

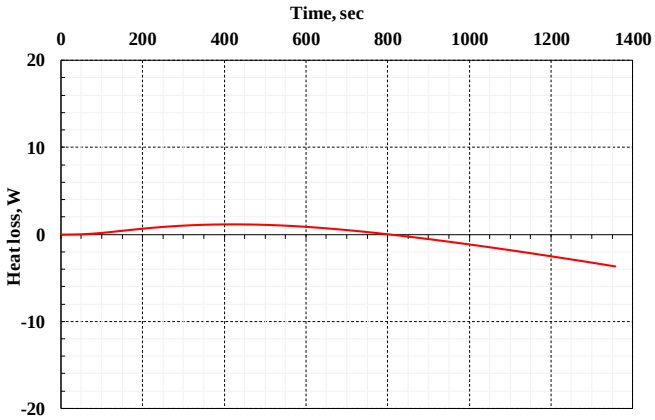

Fig. 4.57. Total heat losses to the environment

Fig. 4.58 and Fig. 4.59 show water temperature and density changes on the symmetry plane at 1110 second. The heater rods reach full thermal power (2600 W/m^2) per 30 seconds. Due to the heat flux emitted by the heater rods, the water heats up and density decreases around the heater rods. As the results of water temperature and density changes, the natural convection flow occurs. The hotter water upward flow arises around the heater rods and the colder water downward flow arises along the solid walls. The water temperature in horizontal directions increases rapidly, meanwhile, temperature increases more slowly in the vertical direction. The thermal stratification region is clearly visible in the heated and the upper unheated regions, and in the small region below the heater rods.

The hotter water flows in horizontal directions near a free surface in the upper unheated and the pipe regions. The hotter water in the upper unheated region has a smaller density than the colder water in the pipe region. The hotter water flows near a free surface to the pipe region, meanwhile the colder water in the bottom part of the pipe region flows to the upper unheated region. The hotter water is mixing with the colder water in the pipe region. The colder water from the pipe region flows downward along the left wall and is mixing with the hotter water in the upper unheated and heated regions. Hotter and hotter water flows near a free surface deeper and deeper to the pipe region until reach the end of the pipe.

Heat transferred from the water to the air leads to the air density changes and natural convection occurs in the air region. The hotter air flows from the computational domain to the environment, meanwhile, 12 ℃ air flows from the environment to the computational domain through the top wall of the fluid region. The water is cooled by colder air, but heat losses in this way are negligible.

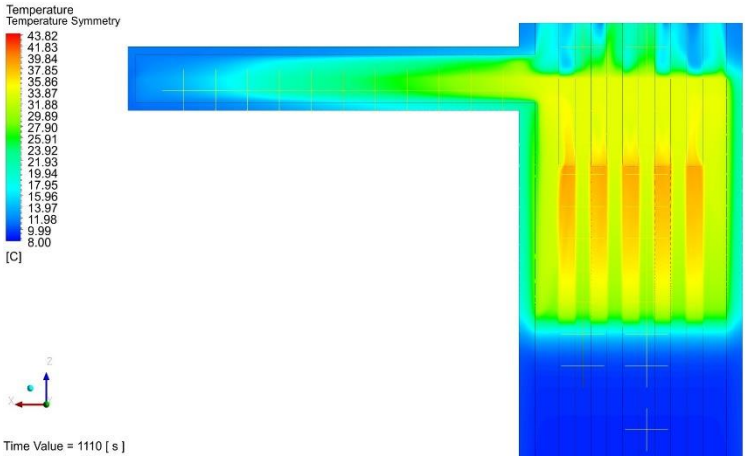

Fig. 4.58. Water temperature on the symmetry plane

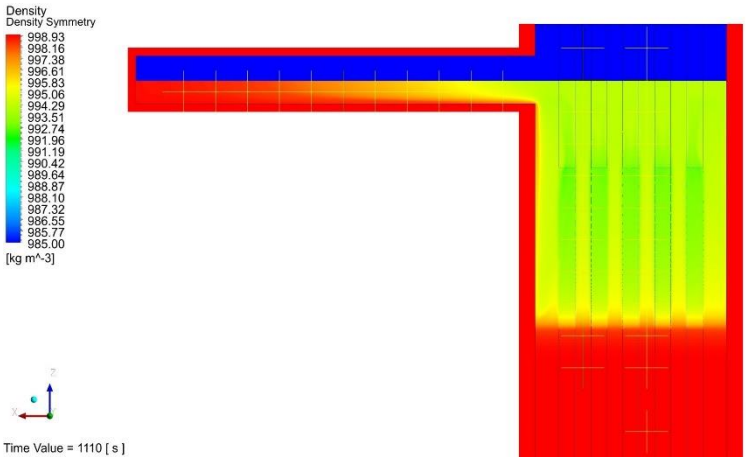

Fig. 4.59. Water density on the symmetry plane

Fig. 4.60 shows the temperature distribution of the outside surfaces of the solid walls. The heat flux emitted by the heater rods heats-up water in the heated, upper unheated and pipe regions and the top part of the lower unheated region. The total water mass in the computational domain is 6.32 kg, but only ~2.02 kg are heated. These 2.02 kg of water transfers the heat flux by convection and conduction to the solid walls. The heat losses on the outside surfaces of the solid walls are presented in Fig. 4.61. In this figure, the minus sign in the legend and green and yellow colours indicate the heat flux from the computational domain to the environment, meanwhile the red colour shows heat flux from the environment to the computational domain. From Fig. 4.60 and Fig. 4.61 it is clearly visible that the hotter water flows deeper and deeper near a free surface in the pipe region, meanwhile, the colder water flows along the bottom surface of the pipe region to the upper unheated region.

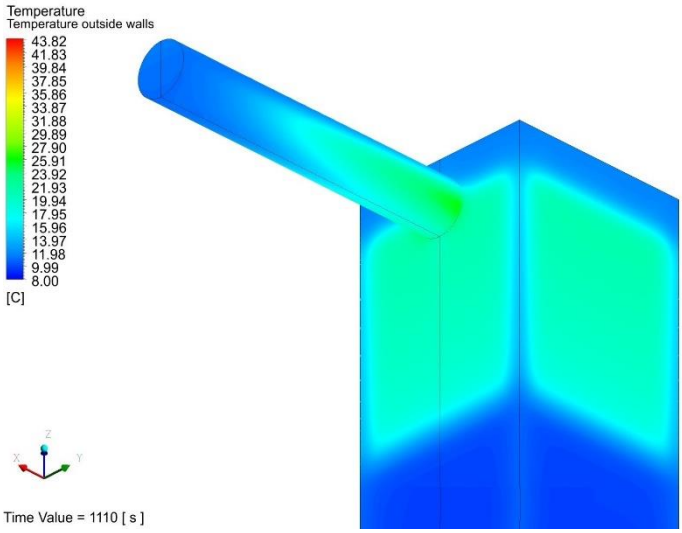

Fig. 4.60. Temperature of the outside surfaces of the solid walls

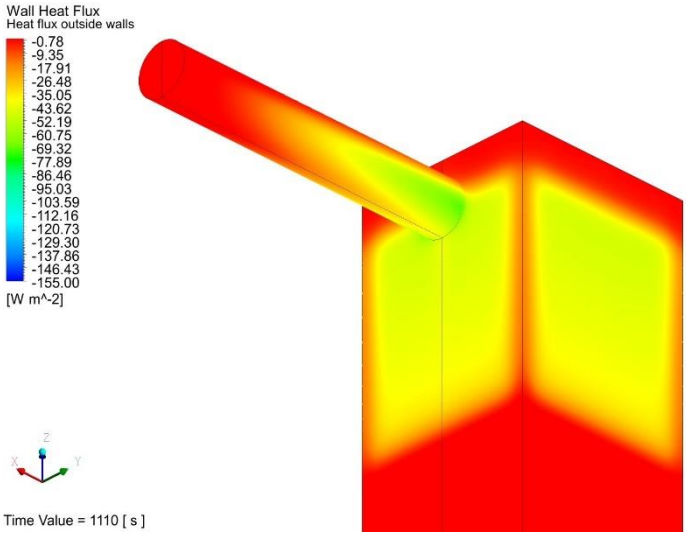

Fig. 4.61. Heat flux through the outside surfaces of the solid walls

CONCLUSIONS

Numerical investigation of two-component two-phase natural convection and thermal stratification phenomena in the cooling pool of the passive system was performed. The appropriateness of the developed CFD modelling methodology was proved based on this numerical investigation. The two experiments, which represent the cooling pool of the passive system and the nuclear reactor cooling during the shutdown, were chosen in order to prove the appropriateness of developed methodology. After the modelling of two-component two-phase natural convection and thermal stratification phenomena, which were investigated in these two experiments, can be concluded:

1. In modelling the thermal stratification phenomenon:
   1.1. When the heating surface is placed in the horizontal position:
      a) the maximum temperature deviation is 5 % using the $k-\varepsilon$ realizable turbulence model with enhanced wall treatment;
      b) the maximum temperature deviation is 89 % using the $k-\omega$ SST turbulence model.
   1.2. The maximum temperature deviation is 6.5 %, when the heating surfaces are placed in the vertical position, using the $k-\varepsilon$ realizable turbulence model with enhanced wall treatment and the $k-\omega$ SST turbulence model.
2. Heat transfer between fluid and solid structures has a significant influence on modelling results in case of the buoyant flow. The maximum temperature deviation when the heating surfaces are placed in the vertical position and the solid structures are not included or included in the numerical model (at the same thermal power) is 9 %. The description of the solid structures in the numerical model significantly influences the fluid mixing and heat transfer in the boundary layer and the whole volume.
3. In order to define the dynamics of the heat release on heating surfaces, a special UDF was created and described in the programming language and implemented in a numerical model. In this way, the modelling capabilities are expanded using this UDF.
4. Good agreement between numerical and experimental results proves the appropriateness of the developed methodology:
   4.1. The maximum temperature deviation (when the heating surface is placed in horizontal position), above the heating surface, is 12.5 %.
   4.2. The maximum temperature deviation (when the heating surfaces are placed in vertical position) in the upper unheated region is 9 %, in the heated region – 5 %, in the thermal stratification region – 2.6 %, and in the pipe region – 14 %.

REFERENCES

1. BEJAN, A. *Convection Heat Transfer*. Hoboken, New Jersey: John Wiley & Sons, Inc., 2013.
2. ELGHNAM, R.I. Experimental and numerical investigation of heat transfer from a heated horizontal cylinder rotating in still air around its axis. *Ain Shams Engineering Journal*. 2014, 5, 177-185.
3. SHAH, N. A., et al. Scrutinization of the effects of Grashof number on the flow of different fluids driven by convection over various surfaces. *Journal of Molecular Liquids*. 2018, 249, 980-990.
4. ANSYS. *Module 08: Heat Transfer, Introduction to ANSYS Fluent, 17.0 Release*. 12 April 2016. [viewed 1 March 2020]. Accessed via ANSYS Customer Portal.
5. GANDHI, M. S., et al. Reduction in thermal stratification in two phase natural convection in rectangular tanks: CFD simulations and PIV measurements. *Chemical Engineering Science*. 2013, 100, 300-325.
6. VASILIEV, A., et al. High Rayleigh number convection in a cubic cell with adiabatic sidewalls. *International Journal of Heat and Mass Transfer*. 2016, 102, 201-212.
7. MONFARED, A.E.F., et al. Thermal flux simulations by lattice Boltzmann method; investigation of high Richardson number cross flows over tandem square cylinders. *International Journal of Heat and Mass Transfer*. 2015, 86, 563-580.
8. KIM, S., et al. Experimental investigation on the natural convection flow in pool boiling. *Nuclear Engineering and Design*. 2014, 280, 349-361.
9. MAWIRE, A., and S.H. TAOLE. A comparison of experimental thermal stratification parameters for an oil/pebble-bed thermal energy storage (TES) system during charging. *Applied Energy*. 2011, 88, 4766-4778.
10. HAN, Y.M., et al. Thermal stratification within the water tank. *Renewable and Sustainable Energy Reviews*. 2009, 13, 1014-1026.
11. HALLER, M.Y., et al. Methods to determine stratification efficiency of thermal energy storage processes – Review and theoretical comparison. *Solar Energy*. 2009, 83, 1847-1860.
12. CONSUL, R., et al. Virtual prototyping of storage tanks by means of three-dimensional CFD and heat transfer numerical simulations. *Solar Energy*. 2004, 77, 179-191.
13. BAHNFLETH, W.P., and A. MUSSER. Thermal performance of a full-scale stratified chilled-water thermal storage tank. *ASHRAE Transactions*. 1998, 104(2), 377-388.
14. ADAMS, D.E. and J.H. DAVIDSON. Tank stratification with a flexible manifold. In *The 1993 American Solar Energy Society Annual Conference, April 22-28 1993, Washington, DC*. Proceedings of solar ’93, pp. 277-281.
15. CASTELL, A., et al. Dimensionless numbers used to characterize stratification in water tanks for discharging at low flow rates. *Renewable Energy*. 2010, 35, 2192-2199.
16. FERNANDEZ-SEARA, J., et al. Experimental analysis of a domestic electric hot water storage tank. Part II: dynamic mode of operation. *Applied Thermal Engineering*. 2007, 27, 137-144.
17. SHAH, L.J., and S. FURBO. Entrance effects in solar storage tanks. *Solar Energy*. 2003, 75, 337-348.

18. MAWIRE, A., et al. Thermal performance of a small oil-in-glass tube thermal energy storage system during charging. *Energy*. 2009, 34, 838-849.
19. YEE, C.K., and F.C. LAI. Effects of a porous manifold on thermal stratification in a liquid storage tank. *Solar Energy*. 2001, 71(4), 241-254.
20. ANSYS. *ANSYS CFX Introduction, 17.2 Release*. August 2016. [viewed 1 March 2020]. Accessed via ANSYS Customer Portal.
21. KESHMIRI, A., ANDREWS, K. *Vascular flow modelling using computational fluid dynamics.* Handbook of Vascular Biology Techniques. Springer, 2015, 343-361.
22. ANSYS. *ANSYS Fluent*. [viewed 1 March 2020]. Accessed via internet: https://www.ansys.com/Products/Fluids/ANSYS-Fluent
23. ANSYS. *HLRS and Cray set new supercomputing record*. [viewed 1 March 2020]. Accessed via Internet: https://www.ansys.com/about-ansys/news-center/11-15-16-ansys-hlrs-cray-set-new-supercomputing-record
24. ANSYS. *ANSYS CFX*. [viewed 1 March 2020]. Accessed via Internet: https://www.ansys.com/products/fluids/ansys-cfx
25. ANSYS. *ANSYS capabilities 2019*. [viewed 1 March 2020]. Accessed via Internet: https://edrmedeso.com/simulation/software/ansys/?gclid=Cj0KCQiAv8PyBRDMARIsAFo4wK043eTYWU6CMlFFWRJoqRClVfYMrDyO0r17WYZvlKREu0pn9ON1tOMaAsF1EALw_wcB
26. OpenFOAM. *About OpenFOAM*. [viewed 1 March 2020]. Accessed via Internet: https://www.openfoam.com/
27. Maya HTT. *STAR-CD*. [viewed 1 March 2020]. Accessed via Internet: https://www.mayahtt.com/products/star-cd
28. Maya HTT. *STAR-CCM+*. [viewed 1 March 2020]. Accessed via Internet: https://www.mayahtt.com/products/star-ccm
29. Flow Science. *FLOW-3D*. [viewed 1 March 2020]. Accessed via Internet: https://www.flow3d.com/products/flow-3d/
30. Safe Solutions. *PHOENICS*. [viewed 1 March 2020]. Accessed via Internet: https://www.safesolutions.com.br/en/software-4/phoenics-en
31. Safe Solutions. *PHOENICS Publications*. [viewed 1 March 2020]. Accessed via Internet: http://www.cham.co.uk/phoenics/d_polis/d_info/publish.htm
32. COMSOL, Inc. *COMSOL Multiphysics*. [viewed 1 March 2020]. Accessed via Internet: https://www.comsol.com/release/5.5
33. EDF. *Code Saturne*. [viewed 1 March 2020]. Accessed via Internet: https://www.code-saturne.org/cms/
34. KESHMIRI, A., et al. Benchmarking of three different CFD codes in simulating natural, forced, and mixed convection flows. *Numerical Heat Transfer*. 2015, 67, 1324-1351.
35. OZTOP, H.F., et al. Fluid flow due to combined convection in lid-driven enclosure having a circular body. *International Journal of Heat and Fluid Flow*. 2009, 30, 886-901.
36. PARK, Y.G., et al. Study on natural convection in a cold square enclosure with a pair of hot horizontal cylinders positioned at different vertical locations. *International Journal of Heat and Mass Transfer*. 2013, 65, 696-712.
37. PARK, Y.G., et al. Natural convection in a square enclosure with two inner circular cylinders positioned at different vertical locations. *International Journal of Heat and Mass Transfer*. 2014, 77, 501-518.

38. PARK, Y.G., et al. Natural convection in a square enclosure with four circular cylinders positioned at different rectangular locations. *International Journal of Heat and Mass Transfer*. 2015, 81, 490-511.
39. KANG, D.H., et al. Bifurcation to unsteady natural convection in square enclosure with a circular cylinder at Rayleigh number of 10^7. *International Journal of Heat and Mass Transfer*. 2013, 64, 926-944.
40. MUN, G.S., et al. Thermo-dynamic irreversibility induced by natural convection in square enclosure with inner cylinder. Part-I: Effect of tilted angle of enclosure. *International Journal of Heat and Mass Transfer*. 2016, 97, 1102-1119.
41. LEE, H.J., et al. Effects of thermal boundary conditions on natural convection in a square enclosure with an inner circular cylinder locally heated from the bottom wall. *International Journal of Heat and Mass Transfer*. 2013, 65, 435-450.
42. CHOI, C., et al. Effect of a circular cylinder's location on natural convection in a rhombus enclosure. *International Journal of Heat and Mass Transfer*. 2014, 77, 60-73.
43. SEO, Y.M., et al. Three-dimensional flow instability of natural convection induced by variation in radius of inner circular cylinder inside cubic enclosure. *International Journal of Heat and Mass Transfer*. 2016, 95, 566-578.
44. LEE, S.H., et al. Three-dimensional natural convection around an inner circular cylinder located in a cubic enclosure with sinusoidal thermal boundary condition. *International Journal of Heat and Mass Transfer*. 2016, 101, 807-823.
45. SOUAYEH, B., et al. Numerical simulation of three-dimensional natural convection in a cubic enclosure induced by an isothermally-heated circular cylinder at different inclinations. *International Journal of Thermal Sciences*. 2016, 110, 325-339.
46. KUMAR, A., et al. 3D CFD simulation of air cooled condenser-I: Natural convection over a circular cylinder. *International Journal of Heat and Mass Transfer*. 2014, 78, 1265-1283.
47. GANDHI, M.S. et al. Two phase natural convection: CFD simulations and PIV measurement. *Chemical Engineering Science*. 2011, 66, 3152-3171.
48. GANDHI, M.S., et al. Study of two phase thermal stratification in cylindrical vessels: CFD simulations and PIV measurements. *Chemical Engineering Science*. 2013, 98, 125-151.
49. KELM, S., et al. A comparative assessment of different experiments on buoyancy driven mixing processes by means of CFD. *Annals of Nuclear Energy*. 2016, 93, 50-57.
50. PAPUKCHIEV, A., and S. BUCHHOLZ. Validation of ANSYS CFX for gas and liquid metal flows with conjugate heat transfer within the European project THINS. *Nuclear Engineering and Design*. 2017, 312, 338-350.
51. KIM, S., et al. Experimental study on the thermal stratification in a pool boiling with a horizontal heat source. *Annals of Nuclear Energy*. 2017, 106, 235-246.
52. KODAMA, S., et al. Thermal stratification and mixing under single- and two-phase flow in rod bundle with axially distributed heat flux in vessel without forced convection. *Nuclear Engineering and Design*. 2014, 268, 164-172.
53. ANSYS. *ANSYS Fluent User's Guide, 17.2 Release*. August 2016. [viewed 1 March 2020]. Accessed via ANSYS Customer Portal.
54. ANSYS. *ANSYS Fluent Theory Guide, 17.2 Release*. August 2016, [viewed 1 March 2020]. Accessed via ANSYS Customer Portal.
55. MAHAFFY, J., et al. *Best Practice Guidelines for the use of CFD in Nuclear Reactor Safety Applications*. 2007. [viewed 1 March 2020]. Accessed via Internet:

https://inis.iaea.org/collection/NCLCollectionStore/_Public/44/037/44037877.pdf?r=1&r=1
56. MAHAFFY, J., et al. *Best Practice Guidelines for the use of CFD in Nuclear Reactor Safety Applications – Revision*. 2014. [viewed 1 March 2020]. Accessed via Internet: https://www.oecd-nea.org/nsd/docs/2014/csni-r2014-12.pdf
57. MENTER, F., et al. *CFD Best Practice Guidelines for CFD Code Validation for Reactor - Safety Applications*. 2002. [viewed 1 March 2020]. Accessed via Internet: https://epdf.pub/cfd-best-practice-guidelines-for-cfd-code-validation-for-reactor-safety-applicat.html
58. CASEY, M., T. WINTERGERSTE, European Research Community on Flow, Turbulence and Combustion. *ERCOFTAC Special Interest Group on Quality and Trust in Industrial CFD: Best practice guidelines*. London: ERCOFTAC, 2000.
59. ANSYS. *Module 09: Best Practice Guidelines, Introduction to ANSYS Fluent, 17.0 Release*. 12 April 2016. [viewed 1 March 2020]. Accessed via ANSYS Customer Portal.
60. ANSYS. *Module 07: Turbulence, Introduction to ANSYS Fluent, 17.0 Release*. 12 April 2016. [viewed 1 March 2020]. Accessed via ANSYS Customer Portal.
61. VERSTEEG, H.K., W. MALALASEKERA. *An Introduction to Computational Fluid Dynamics*. Glasgow: Pearson Education Limited, 2007.
62. ANSYS. *Module 05: Solving, Introduction to ANSYS Fluent, 17.0 Release*. 12 April 2016. [viewed 1 March 2020]. Accessed via ANSYS Customer Portal.
63. ANSYS. *Module 10: Transient Flow Modeling, Introduction to ANSYS Fluent, 17.0 Release*. 12 April 2016. [viewed 1 March 2020]. Accessed via ANSYS Customer Portal.
64. ANSYS. *ANSYS Fluent Customization Manual, 17.2 Release*. August 2016. [viewed 1 March 2020]. Accessed via ANSYS Customer Portal.
65. BAE, B.U., et al. Design of condensation heat exchanger for the PAFS (Passive Auxiliary Feedwater System) of APR+ (Advanced Power Reactor Plus). *Annals of Nuclear Energy*. 2012, 46, 134-143.
66. Kim, S., et al. An experimental study on the validation of cooling capability for the Passive Auxiliary Feedwater System (PAFS) condensation heat exchanger. *Nuclear Engineering and Design*. 2013, 260, 54-63.
67. ANSYS. *Module 08: Heat Transfer, Introduction to ANSYS Fluent, 17.0 Release*. 12 April 2016. [viewed 1 March 2020]. Accessed via ANSYS Customer Portal.
68. BLUMM, J., and A. LINDEMANN. Characterization of the thermophysical properties of molten polymers and liquids using the flash technique. *High Temperatures – High Pressures*. 2003/2007, 35/36, 627-632.
69. Corning Glass Works. *Pyrex – Glass Code 7740*. [viewed 1 March 2020]. Accessed via Internet: http://glassfab.com/wp-content/uploads/2015/08/Corning-Pyrex.pdf
70. AK Steel Corporation. *304/304L Stainless Steel*. [viewed 1 March 2020]. Accessed via Internet: http://www.aksteel.com/sites/default/files/2018-01/304304L201706_1.pdf
71. MatWeb. *Overview of materials for Acrylic, Cast*. [viewed 1 March 2020]. Accessed via Internet: http://www.matweb.com/search/datasheet.aspx?bassnum=O1303
72. TOULOUKIAN, Y.S., P.E. LILEY, S.C. SAXENA, P. HESTERMANS. *Thermophysical Properties of Matter*. New York: Plenum Publishing Corp., 1970.
73. KEENAN, J.H., J. CHAO, J. KAYE. *Gas Tables*. New York: Joh Wiley & Sons, 1980.

74. SENGERS J.V., and J.T.R. WATSON. Improved International Formulations for the Viscosity and Thermal Conductivity of Water Substance. *Journal of Physical and Chemical Reference Data*. 1986, 15(4), 1291-1312.
75. RATHAKRISHNAN, E. *Gas Tables*. Hyderabad: Universities Press (India) Private Limited, 1993.
76. HILSENRATH, J., C.W. BECKETT, W.S. BENEDICT, L. FANO, H. MASI, R.L. NUTTALL, Y.S. TOULOUKIAN, H.W. WOOLLEY. *Tables of Thermal Properties of Gases*. Publisher: National Bureau of Standards, 1955.
77. MARANZANA, G., et al. Experimental estimation of the transient free convection heat transfer coefficient on a vertical flat plate in air. *International Journal of Heat and Mass Transfer*. 2002, 45, 3413-3427.

LIST OF SCIENTIFIC ARTICLES RELATED TO DISSERTATION

Articles in the "Web of Science Core Collection" references of the "Clarivate Analytics" database

1. GRAŽEVIČIUS, A., and A. KALIATKA. Modelling of the spent fuel heat-up in the spent fuel pools using one-dimensional system codes and CFD codes. *Kerntechnik*. 2017, 82(3), 316-333.
2. GRAŽEVIČIUS, A., et al. Numerical investigation of two-phase natural convection and temperature stratification phenomena in a rectangular enclosure with conjugate heat transfer. *Nuclear Engineering and Technology*. 2020, 52, 27-36.

Articles in the proceedings of international conferences

1. GRAŽEVIČIUS, A. CFD Simulating the Heat Removal from Fuel Assembly Located in the Spent Fuel Pool. In *Proceedings of the Conference of Young Scientists on Energy Issues 2016*. 2016. pp. 341-348. ISSN 1822-7554.
2. KALIATKA, A., et al. Modeling of heat transfer processes in the spent fuel pool using one and three dimensional computer codes. In *Proceedings of the NUTHOS-11: 11th International Topical Meeting on Nuclear Reactor Thermal-Hydraulics, Operation and Safety*. Paper N11P0442. 2016. pp. 1-12.
3. GRAŽEVIČIUS, A. Modelling of pool heat-up experiment using ANSYS Fluent. In *Proceedings of the Conference of Young Scientists on Energy Issues 2017*. 2017. pp. 216-224. ISSN 1822-7554.
4. GRAŽEVIČIUS, A. Numerical investigation of the thermal hydraulic phenomena in a rectangular enclosure. In *Proceedings of the Conference of Young Scientists on Energy Issues 2018*. 2018. pp. 269-276. ISSN 1822-7554.
5. GRAŽEVIČIUS, A. and A. KALIATKA. Numerical investigation of two-phase natural convection and thermal stratification phenomena in rod bundle. In *Proceedings of the Conference of Young Scientists on Energy Issues 2019*. 2019. pp. 259-266. ISSN 1822-7554.

Presentations in the international conferences

1. GRAŽEVIČIUS, A. CFD Simulating the Heat Removal from Fuel Assembly Located in the Spent Fuel Pool. In *Proceedings of the Conference of Young Scientists on Energy Issues 2016*. 2016. pp. 341-348. ISSN 1822-7554.
2. KALIATKA, A., et al. Modeling of heat transfer processes in the spent fuel pool using one and three dimensional computer codes. In *Proceedings of the NUTHOS-11: 11th International Topical Meeting on Nuclear Reactor Thermal-Hydraulics, Operation and Safety*. Paper N11P0442. 2016. pp. 1-12.
3. GRAŽEVIČIUS, A. Modelling of pool heat-up experiment using ANSYS Fluent. In *Proceedings of the Conference of Young Scientists on Energy Issues 2017*. 2017. pp. 216-224. ISSN 1822-7554.

4. GRAŽEVIČIUS, A. Numerical investigation of the thermal hydraulic phenomena in a rectangular enclosure. In *Proceedings of the Conference of Young Scientists on Energy Issues 2018*. 2018. pp. 269-276. ISSN 1822-7554.
5. GRAŽEVIČIUS, A. and A. KALIATKA. Numerical investigation of two-phase natural convection and thermal stratification phenomena in rod bundle. In *Proceedings of the Conference of Young Scientists on Energy Issues 2019*. 2019. pp. 259-266. ISSN 1822-7554.

APPENDIXES

APPENDIX A: Calculation journal of the KAERI experiment

Case	Core(s) No	Mesh size	What was changed?
01	108	218313	FLUENT 17.2. Pressure-based. Transient. Gravity enabled. VOF. Lee Evaporation-Condensation model. k-e Realizable EWT. UDF (heating model) for heater rod – heat flux 600 W / 120 sec. HTC = 20 W/(m^2·K). Solution Methods: PISO; SC=1; NC=1; Gradient: Least Squares Cell Based; Pressure: PRESTO!; Density: 2; Momentum: 2; Volume Fraction: Geo-Reconstruct; Turbulent Kinetic Energy: 1; Turbulent Dissipation Rate: 1; Energy: 2; Transient Formulation: First Order Implicit. Solution Controls: Pressure: 0.3; Density: 1; Body Forces: 1; Momentum: 0.7; Vaporization Mass: 1; Turbulent Kinetic Energy: 0.8; Turbulent Dissipation Rate: 0.8; Turbulent Viscosity: 1; Energy: 1. Convergence criteria: 10^{-6} for energy and 10^{-5} for continuity, k, omega, X, Y, Z velocities. Solution Initialization: Standard Initialization; Gauge Pressure: 0; X Velocity: 0; Y Velocity: 0; Z Velocity: 0; Turbulent Kinetic Energy: 0.001; Turbulent Dissipation Rate: 0.001; Initial temperatures of water, air & ambient: 288.15 °C; water-liquid Volume Fraction: 0; water-vapor Volume Fraction: 0. Time step size: 0.015 sec. Time steps number: 960'000. Max iterations per t/s 6. Ending time / Flow time / Solution time: 144'000 sec.
02			Similar to 01 but now: k-w SST turbulence model.
03			Similar to 01 but now: Laminar flow model.
04			Similar to 01 but now: Time step: 0.01 sec.
05		313964	Similar to 01 but now: Better mesh.
06		570610	Similar to 05 but now: Better mesh.
07		922736	Similar to 06 but now: Better mesh.
08		313964	Similar to 05 but now: Cooling of the bottom wall.
09			Similar to 05 but now: UDF for slow heating: 600 W / 300 sec.
10			Similar to 05 but now: UDF for partial heating: top surface of the heater rod 480 W / 60 sec.; bottom surface of the heater rod 120 W / 60 sec.

11			Similar to 05 but now: UDF for smaller heat flux: 480 W / 60 sec.
12			Similar to 05 but now: UDF for smaller heat flux: 450 W / 60 sec.

APPENDIX B: Calculation journal of the Osaka University experiment

Case	Core(s) No	Mesh size	What was changed?	Date
01	156	463176	FLUENT 17.2. Pressure-based. Transient. Gravity enabled. VOF. Lee Evaporation-Condensation model. k-e Realizable EWT. UDF (heating model) for heater rods – heat flux 4400 W/m^2 / 0 sec (345.58 W / 0 sec). No heat losses. Solution Methods: PISO; SC=1; NC=1; Gradient: Least Squares Cell Based; Pressure: PRESTO!; Density: 2; Momentum: 2; Volume Fraction: Geo-Reconstruct; Turbulent Kinetic Energy: 1; Turbulent Dissipation Rate: 1; Energy: 2; Transient Formulation: First Order Implicit. Solution Controls: Pressure: 0.3; Density: 1; Body Forces: 1; Momentum: 0.7; Vaporization Mass: 1; Turbulent Kinetic Energy: 0.8; Turbulent Dissipation Rate: 0.8; Turbulent Viscosity: 1; Energy: 1. Convergence criteria: 10^{-6} for energy and 10^{-5} for continuity, k, omega, X, Y, Z velocities. Solution Initialization: Standard Initialization; Gauge Pressure: 0; X Velocity: 0; Y Velocity: 0; Z Velocity: 0; Turbulent Kinetic Energy: 0.001; Turbulent Dissipation Rate: 0.001; Initial temperatures: water 8.15÷9.37 °C, air & ambient 11.73 °C; water-liquid Volume Fraction: 0; water-vapor Volume Fraction: 0. Time step size: 0.015 sec. Time steps number: 90467. Max iterations per t/s 50. Ending time / Flow time / Solution time: 1357.005 sec.	19/03/2019
02	168		Similar to 01 but now: Max iterations per t/s 4.	21/03/2019
03			Similar to 02 but now: Time step size: 0.01 sec. Time steps number: 135700. Ending time / Flow time / Solution time: 1357.000 sec.	22/03/2019
04			Similar to 02 but now: Time step size: 0.005 sec. Time steps number: 271400. Ending time / Flow time / Solution time: 1357.000 sec.	23/03/2019
05	180		Similar to 02 but now: Heat losses are included → HTC = 5 W/(m^2·K).	24/03/2019
06	156		Similar to 02 but now: Heat losses are included → HTC = 10 W/(m^2·K).	25/03/2019
07	96		Similar to 02 but now: Heat losses are included → HTC = 20 W/(m^2·K).	
08	84		Similar to 02 but now: Heat losses are included → HTC = 30 W/(m^2·K).	
09	96		Similar to 02 but now: Heat losses are included → HTC = 50 W/(m^2·K).	26/03/2019

10	84		Similar to 02 but now: Heat losses are included → HTC = 70 W/(m^2·K).	
11	96		Similar to 02 but now: Heat losses are included → HTC = 100 W/(m^2·K).	27/03/2019
12	84		Similar to 09 but now: UDF (heating model) for heater rods – heat flux 4400 W/m^2 / 30 sec (345.58 W / 30 sec).	
13	96		Similar to 09 but now: UDF (heating model) for heater rods – heat flux 4400 W/m^2 / 60 sec (345.58 W / 60 sec).	28/03/2019
14	84		Similar to 09 but now: UDF (heating model) for heater rods – heat flux 4400 W/m^2 / 120 sec (345.58 W / 120 sec).	
15	96		Similar to 05 but now: UDF (heating model) for heater rods – heat flux 3500 W/m^2 / 30 sec (274.89 W / 30 sec).	01/04/2019
16	96	463176	Similar to 05 but now: UDF (heating model) for heater rods – heat flux 2500 W/m^2 / 30 sec (196.35 W / 30 sec).	01/04/2019
17			Similar to 05 but now: UDF (heating model) for heater rods – heat flux 2600 W/m^2 / 30 sec (204.20 W / 30 sec).	02/04/2019
18			Similar to 05 but now: UDF (heating model) for heater rods – heat flux 2700 W/m^2 / 30 sec (212.06 W / 30 sec).	
19			Similar to 17 but now: UDF (heating model) for heater rods – heat flux 2600 W/m^2 / 0 sec (204.20 W / 0 sec).	03/04/2019
20			Similar to 17 but now: $k-\varepsilon$ Standard EWT turbulence model.	
21			Similar to 17 but now: $k-\omega$ SST turbulence model.	05/04/2019
22	96	98550	Similar to 17 but now: Mesh cells volume increased by a factor 0.5. Time step size increased by a factor 1.5. Time step size: 0.0225 sec. Time steps number: 60311. Ending time / Flow time / Solution time: 1356.9975 sec.	
23	180	1125338	Similar to 17 but now: Mesh cells volume reduced by a factor 1.5. Time step size reduced by a factor 0.5. Time step size: 0.0075 sec. Time steps number: 180933. Ending time / Flow time / Solution time: 1356.9975 sec.	06/04/2019
24		2763037	Similar to 17 but now: Mesh cells volume reduced by a factor 1.5 twice. Time step size reduced by a factor 0.5 twice.	10/04/2019

			Time step size: 0.00375 sec. Time steps number: 361866. Ending time / Flow time / Solution time: 1356.9975 sec.	
~~25~~		~~7285416~~	~~Similar to 17 but now:~~ ~~Mesh cells volume reduced by a factor 1.5 three times. Time step size reduced by a factor 0.5 three times. Time step size: 0.001875 sec. Time steps number: 723733. Ending time / Flow time / Solution time: 1356.999375 sec.~~	-
26		2763037 + 715240 = 3478277	Similar to 24 but now: Solid walls were added (Lucite material). Density 1180 kg/m^3. Specific heat (cp) 1810 J/kg·K. Thermal conductivity 0.198 W/m·K. Max iterations per t/s 50.	29/04/2019

SL344. 2020-07-15, 12,25 leidyb. apsk. 1. Tiražas 12 egz.
Išleido Kauno technologijos universitetas, K. Donelaičio g. 73, 44249 Kaunas
Spausdino leidyklos „Technologija“ spaustuvė, Studentų g. 54, 51424 Kaunas